

University of Louisville

ThinkIR: The University of Louisville's Institutional Repository

Electronic Theses and Dissertations

5-2013

Impedance analysis of endothelial cells undergoing orbital shear stress.

Mark Jacob Gruenthal
University of Louisville

Follow this and additional works at: <https://ir.library.louisville.edu/etd>

Recommended Citation

Gruenthal, Mark Jacob, "Impedance analysis of endothelial cells undergoing orbital shear stress." (2013). *Electronic Theses and Dissertations*. Paper 542.
<https://doi.org/10.18297/etd/542>

This Master's Thesis is brought to you for free and open access by ThinkIR: The University of Louisville's Institutional Repository. It has been accepted for inclusion in Electronic Theses and Dissertations by an authorized administrator of ThinkIR: The University of Louisville's Institutional Repository. This title appears here courtesy of the author, who has retained all other copyrights. For more information, please contact thinkir@louisville.edu.

IMPEDANCE ANALYSIS OF ENDOTHELIAL CELLS UNDERGOING ORBITAL
SHEAR STRESS

By

Mark Jacob Gruenthal
B.S., Washington University in St Louis, 2007

A Thesis
Submitted to the Faculty of the
J. B. Speed School of Engineering of the University of Louisville
in Partial Requirement
for the Degree of

Master of Science

Department of Mechanical Engineering
University of Louisville
Louisville, Kentucky

May 2013

IMPEDANCE ANALYSIS OF ENDOTHELIAL CELLS UNDERGOING ORBITAL
SHEAR STRESS

By

Mark Jacob Gruenthal
B.S., Washington University in St Louis, 2007

A Thesis Approved on

April 23, 2013

by the following Thesis Committee:

Dr. Stuart J. Williams, Thesis Director

Dr. M. Keith Sharp

Dr. Robert Eric Berson

ACKNOWLEDGEMENTS

I would like to thank my thesis director, Dr. Stuart Williams, for his guidance in completing this project. I would also like to thank Dr. Robert Keynton for supplying the environmental chamber and impedance analyzer. In addition, I must acknowledge Vanessa Velasco for performing device fabrication, and Jonathan Michael D. Thomas for providing computational fluid dynamics modeling results.

ABSTRACT

IMPEDANCE ANALYSIS OF ENDOTHELIAL CELLS UNDERGOING ORBITAL SHEAR STRESS

Mark Jacob Gruenthal

April 23, 2013

Understanding the endothelium at the cellular level could further knowledge of the cardiovascular system as a whole and could therefore lead to advances in the prevention and treatment of cardiovascular disease. Electric cell-substrate impedance sensing is an *in vitro* technique that can be used for observing the behavior of endothelial cells in real-time using a fluid flow environment to simulate the circulatory system. This study examined the effect of fluid shear stress on human umbilical vein endothelial cells using electrochemical impedance spectroscopy (impedance sensing). Circuit models were fit to empirical data to measure cell layer resistance and capacitance changes, and to determine if data trends follow those of previously published findings. Information derived from transendothelial electrical resistance measurements, about changes in cell layer permeability when subjected to varying shear stress conditions within an orbiting circular well, was used to draw conclusions aided by microscopic images of the cells.

TABLE OF CONTENTS

	PAGE
APPROVAL PAGE.....	ii
ACKNOWLEDGMENTS.....	iii
ABSTRACT.....	iv
LIST OF TABLES.....	vi
LIST OF FIGURES.....	vii
I. INTRODUCTION.....	1
II. REVIEW OF RELATED LITERATURE.....	6
A. THE ENDOTHELIUM.....	6
B. MEASUREMENT SYSTEMS.....	19
C. IMPEDANCE SENSING.....	32
D. ORBITAL FLOW.....	50
III. SYSTEM DESIGN.....	54
A. SPECIFICATIONS.....	54
B. BENEFITS.....	56
IV. MATERIALS AND METHODS.....	58
A. CELL CULTURE DEVICE.....	58
B. ATTACHMENT AND SPREADING.....	61
C. SHEAR STRESS RESPONSE.....	62
D. IMPEDANCE DATA.....	64
V. RESULTS.....	70
A. ATTACHMENT AND SPREADING.....	70
B. SHEAR STRESS CALCULATIONS.....	81
C. SHEAR STRESS RESPONSE.....	84
VI. DISCUSSION.....	101
A. ATTACHMENT AND SPREADING.....	101
B. SHEAR STRESS RESPONSE.....	102
VII. CONCLUSION.....	110
REFERENCES.....	116
APPENDIX.....	124
CURRICULUM VITAE.....	128

LIST OF TABLES

TABLE	PAGE
1. Circuit Parameters for a Recording Electrode of Row A-5.0mm from the Center with Counter Electrodes A and 1.....	72
2. Circuit Parameters for a Recording Electrode of Row A-7.5mm from the Center with Counter Electrodes A and 1.....	73
3. Circuit Parameters for a Recording Electrode of Row A-10.0mm from the Center with Counter Electrodes A and 1.....	74
4. Circuit Parameters for a Recording Electrode of Row B-2.5mm from the Center with Counter Electrodes B and 2.....	75
5. Circuit Parameters for a Recording Electrode of Row B-7.5mm from the Center with Counter Electrodes B and 2.....	76
6. TER Values Normalized to RE Area to Produce Specific Cell Layer Resistance.....	77
7. Constant Phase Element Parameters at Different Averaged Culture Time-Points.....	78

LIST OF FIGURES

FIGURE	PAGE
1. A schematic representation of the circuit model that Giaever and Keese (1991) used to represent the electrochemical system.....	40
2. A schematic representation of the circuit model that Goda <i>et al.</i> (2005) used to represent the cell layer.....	43
3. A schematic representation of the circuit model that best fit data from conductance scanning of unilayered epithelia (Gitter <i>et al.</i> , 1997).....	44
4. A schematic representation of the circuit models that Wegener <i>et al.</i> (1999) used....	45
5. A schematic representation of the device.....	56
6. A photograph of the device with the PDMS well on its surface.....	60
7. The PCB used to select electrode connections.....	64
8. The device used for impedance sensing inside the environmental chamber.....	65
9. A schematic of the electric circuits fit to impedance data.....	67
10. Impedance Bode plot from the RE of row A at a 5.0 mm radius and CE A.....	79
11. Impedance phase plot from the RE of row A at a 5.0 mm radius and CE A.....	80
12. Nyquist plot of data from the RE of row A at a 5.0 mm radius and CE A.....	81
13. A contour plot of wall shear stress magnitude and the radii examined.....	83

14. TER normalized to its baseline value and plotted over two hours of shear stress exposure for the RE of Row B at a radius of 15.0 mm.....	85
15. TER normalized to its baseline value and plotted over two hours of shear stress exposure for the RE of Row A at a radius of 15.0 mm.....	86
16. TER normalized to its baseline value and plotted over two hours of shear stress exposure for the RE of Row A at a radius of 12.5 mm.....	87
17. TER normalized to its baseline value and plotted over two hours of shear stress exposure for the RE of Row A at a radius of 10.0 mm.....	88
18. TER normalized to its baseline value and plotted over two hours of shear stress exposure for the RE of Row A at a radius of 7.5 mm.....	89
19. TER normalized to its baseline value and plotted over two hours of shear stress exposure for the RE of Row A at a radius of 5.0 mm.....	90
20. Cell layer capacitance normalized to its baseline value and plotted over two hours of shear stress exposure for the RE of Row B at a radius of 15.0 mm.....	91
21. Cell layer capacitance normalized to its baseline value and plotted over two hours of shear stress exposure for the RE of Row A at a radius of 15.0 mm.....	92
22. Cell layer capacitance normalized to its baseline value and plotted over two hours of shear stress exposure for the RE of Row A at a radius of 12.5 mm.....	93
23. Cell layer capacitance normalized to its baseline value and plotted over two hours of shear stress exposure for the RE of Row A at a radius of 10.0 mm.....	94
24. Cell layer capacitance normalized to its baseline value and plotted over two hours of shear stress exposure for the RE of Row A at a radius of 7.5 mm.....	95

25. Cell layer capacitance normalized to its baseline value and plotted over two hours of shear stress exposure for the RE of Row A at a radius of 5.0 mm.....	96
26. A Bode plot of the impedance of the electrochemical system over the full spectrum of recording frequencies.....	97
27. An image of the device surface in the vicinity of the electrode of Row A at a radius of 12.5 mm after two hours of shear stress exposure.....	99
28. An image of the device surface in the vicinity of the electrode of Row A at a radius of 12.5 mm after two hours of shear stress exposure.....	100

I. INTRODUCTION

Cardiovascular disease is a major cause of health problems and death throughout the world. In the year 2009, heart disease was listed as the number one cause of death in the United States according to the *National Vital Statistics Reports* (Kochanek *et al.*, 2011). Of the 780,624 fatalities attributed to major cardiovascular diseases that year, 57,043 had atherosclerotic cardiovascular disease listed as the cause of death. The health of the circulatory system is essential to the proper functioning of the human body. The endothelium, which makes up the innermost lining of all blood vessels, is one cell width in thickness (Chiu and Chien, 2011). It is critical to the homeostasis of the vasculature for proper functioning and in its role in vascular disease when it is dysfunctional.

The endothelium serves as a barrier between the circulating blood and the surrounding tissues. Its compromised integrity has been detected in many pathological conditions such as ischemia, atherosclerosis, inflammation, and tumor progression (Wegener *et al.*, 1999). Due to the importance of the endothelium to many physiological and pathological processes, this biological monolayer is an area of great interest to many clinicians and laboratory researchers. Investigators have paid special attention to the fact that endothelial cells (ECs) experience many mechanical forces mainly as a result of their anatomic location in direct contact with the circulating blood (Davies, 1995). For this reason, over the last thirty years the world has seen the rise of many cell culture flow (CCF) systems to study the behavior of typically confluent EC monolayers under fluid

flow as a means of simulating the hemodynamic shear stress found in the *in vivo* cellular microenvironment (Young and Simmons, 2010).

Some of the drawbacks of current conventional CCF systems are that they are usually custom designed and they cannot be easily modified to adapt to varying experimental goals, they typically require auxiliary equipment that demands large amounts of dedicated lab space, and they often involve large EC cultures that necessitate the consumption of large volumes of reagents (Young and Simmons, 2010). Over the last ten to fifteen years, these drawbacks of macro-scale CCF systems have led to the adoption of some microfluidic approaches to studying the effects of mechanical forces on ECs. On the micro-scale, low Reynolds numbers allow consistently laminar flows to be introduced to the cellular environment, resulting in the generation of easily predictable shear stress values on EC monolayers. Additionally, micro-fabrication techniques such as soft lithography (Xia and Whitesides, 1998) as well as replica molding of elastomeric materials have enabled the affordable production of these devices with easy disposability allowing for rapid prototyping and proof of principle experiments.

Despite the advantages, these microfluidic systems are not without their own concerns. For example, Gray *et al.* (2002) demonstrated that bovine aortic endothelial cells (BAECs) align themselves in the direction of fluid flow in a 200-micron wide micro-channel after sixteen hours of shear stress exposure at 20 dynes/cm², as would be expected. However, the group also showed that BAECs align themselves in the direction of channel length for channels less than 200-microns in width even when no fluid flow is occurring. This experimental outcome shows that channel width has an effect on cell morphology and that this design parameter may confound experimental results. One of

the downsides of microfluidic experiments involving ECs is that the biological validity of outcomes is still questionable, and further research is necessary in order to confirm that EC behavior is scalable from the macro- to the micro-scale (Young and Simmons, 2010). Because most of the current literature on ECs was established with macro-scale CCF systems, the continuation of the use of these types of traditional methods has been desirable so that results can be compared objectively.

Macro-scale CCF systems have the advantage of having the capacity to culture large populations of ECs, allowing for the yield of enough biological material for endpoint measurements such as gene and protein expression levels, while smoothing out heterogeneities within the sample being studied (Young and Simmons, 2010). On the other hand, microfluidic cell culture systems involve small cellular populations, reducing the amount of detectable analyte. However, these concerns revolve around the question of what specific endpoint measurements to select for a given CCF study.

While many studies rely on immunostaining of intracellular proteins that are associated with cytoskeletal remodeling at the termination of shear stress-based flow experiments (Noria *et al.*, 1999; Girard and Nerem, 1995), these types of studies limit themselves to analyzing cellular behavior and morphology at the end of some defined time period of shear stress exposure. Because the time frame of endothelial responses to shear stress typically varies from seconds to hours (DePaola *et al.*, 2001), many researchers have become interested in the real-time evaluation of cell structure and function during flow as opposed to typical *in vitro* measurements of secreted proteins, immunohistological stains, and gene expression levels after the cessation of shear stress exposure. Live video microscopy has been used as one method for monitoring the

dynamics of ECs in response to shear stress in real-time, and this procedure has been combined with image processing techniques in order to analyze cell morphology as a function of time – an approach called morphodynamics (Dieterich *et al.*, 2000).

DePaola *et al.* (2001) employed a practice that involves taking electrical measurements of cells to analyze the behavior of ECs under flow. This technique is based on measuring the electrical impedance of cells. Electrochemical impedance spectroscopy (also referred to as impedimetric sensing) has become a viable alternative to traditional techniques for a variety of biosensing applications such as immuno-binding based biosensing, DNA hybridization studies, and cytotoxicity assessment (Guan *et al.*, 2004). This technique can also be applied in order to monitor the interaction of adherent cells with an underlying substrate. Giaever and Keese (1991) were the pioneers of this specific method, known as Electric Cell-Substrate Impedance Sensing (ECIS). It was originally created for monitoring the attachment and spreading, as well as the micro-motion of WI-38 fibroblast cells.

The original ECIS technique involved culturing cells on gold electrodes, with each cell culture dish containing four small ($\sim 10^{-3} \text{ cm}^2$) and one large ($\sim 2 \text{ cm}^2$) electrode (Giaever and Keese, 1991). In order to measure impedance, the large electrode and one of the small electrodes were connected to a phase-sensitive lock-in amplifier, and an AC signal was supplied to the connection, which was completed by the electrolyte cell culture media through which current traveled. Since its development, ECIS has been used for measuring a wide array of cellular properties such as permeability, changes in shape, and for detecting pore formation in, and resealing of, the plasma membrane (DePaola *et al.*, 2001).

The performance of impedimetric sensing during the course of cell-substrate interactions of ECs under hydrodynamic shear stress, represents a promising experimental paradigm that can be used to measure and interpret cellular function and morphology in a physiologically relevant setting. The time frame of individual adaptations of cells to shear stress can vary between seconds and hours (DePaola *et al.*, 2001), so it is desirable to develop a platform that is a real-time, sensitive, and accurate evaluation of EC monolayers subjected to wall shear stress. A device was constructed to serve as an environment where adherent cells could be cultured under fluid flow conditions with an orbital shaker. Impedance was sensed from both static and orbiting cultures to confirm the method's ability to assess cell layer permeability accurately, and to determine whether trends in the data during fluid shear agreed with results of previous studies. These techniques were used to examine differences in the responses of Human Umbilical Vein Endothelial Cells (HUVECs) to unique shear stress waveforms.

The specific objectives of the study were to first, validate the measurement of cell layer resistance, which represents an assessment of permeability. The next desired achievement was to observe the effect of fluid shear stress levels, of various ranges and peak values as computed numerically, on the cellular impedance characteristics at different radial locations within an orbiting circular well. It was sought to determine whether trends in the responses of the electrical impedance of HUVECs at these varying positions correlate with data from previously published literature. It was a further intention of the study to draw conclusions about the biological responses of the cells from their impedance characteristics using microscopy, after the period of fluid shear stress.

II. REVIEW OF RELATED LITERATURE

A. The Endothelium

1. Structure and Function

The endothelium comprises a biologically active cellular monolayer that lines the inner (luminal) blood-contacting surfaces of the cardiovascular system (Young and Simmons, 2010). It is a dynamic barrier that is constantly reacting and adapting to its environment. Some of the biological functions carried out by the endothelium include control of transport across the vascular wall, and transduction of blood-borne signals, and it is involved in the regulation of vascular tone, vascular growth (angiogenesis), homeostasis, and blood clot formation (thrombosis) (DePaola *et al.*, 2001).

Blood vessels are continually subjected to various hemodynamic forces such as changes in hydrostatic pressure, cyclic stretch, and fluid shear stress induced by the pulsatile nature of blood pressure and flow (Chiu and Chien, 2011). The complex interface that the endothelium constitutes plays a key role in mechanotransduction and in the regulation of signaling events between the circulating blood and the blood vessel wall (DePaola *et al.*, 2001). This role of transducing mechanical cues from the local microenvironment is key to the nature of how the endothelium functions, and how it initiates biological responses at the molecular level that ultimately result in changes in cellular structure and function (Young and Simmons, 2010).

Both hemodynamic forces from the luminal blood (Davies, 1995), as well as

adhesive forces between cell-surface anchoring proteins (integrins) and the basement membrane (basal lamina) (Tzima, 2006) contribute to the mechanical signals that are known to regulate vascular function through the mechanotransduction-related signaling pathways that are involved (Young and Simmons, 2010). The forms that these mechanical stimuli take are known to affect vascular homeostasis and the development of cardiovascular pathologies.

The types of blood vessels that exist in the body are diverse, and the differences in the physical properties of the associated local microenvironments cause the ECs contained within them to be heterogeneous in both structure and function (Aird, 2007). ECs align parallel to the direction of blood flow in arteries, and they elongate to different aspect ratios and are less permeable to blood-borne factors than ECs found in capillary beds and veins (Thurston *et al.*, 2000). On the other hand, venous ECs are generally more permeable, their morphology is polygonal instead of elongated, and they lack specific orientation regarding the direction of blood flow (Young and Simmons, 2010). These phenotypic traits that distinguish the ECs from varying anatomic locations are closely correlated with differences in the hemodynamic environments in which the ECs reside.

These cells are anchorage-dependent, meaning that they only function when adhered to a substrate (Young and Simmons, 2010). *In vivo*, ECs adhere to the basal lamina, which is composed of various extracellular matrix (ECM) proteins such as type IV collagen, laminin, and fibronectin (Alberts *et al.*, 2002). Adhesion to the basal lamina is mediated by transmembrane integrins at the cell surface that bind to the ECM and link it to the intracellular cytoskeleton (Hynes, 1992). The integrin proteins provide a

mechanism that allows the cell to remain adherent to the ECM while resisting the blood flow-induced shear stress that acts on the cell's apical surface. Integrin proteins function in this way by creating focal adhesions that anchor the cell to the ECM, and they also serve the purpose of transducing the mechanical signals generated by hemodynamic forces (Shyy and Chien, 2002). Thus, the cell cytoskeleton, which is linked to the cell's basal surface, forms a bridge between the shear stress that acts on transmembrane proteins on the luminal side (referred to as mechanosensors) and integrins on the cell's abluminal side (referred to as mechanotransducers) (Davies, 1995).

Also of great importance to understanding the functions of the endothelium is the study of how ECs form barriers that limit the flux of certain macromolecular particles as well as other cells. The intercellular junctions formed between adjacent ECs in the monolayer do not display any specific order; they consist of an extended adherens junction zone where gap junctions and strands of tight junctions are morphologically juxtaposed (Franke *et al.*, 1988). The adherens junctions that are found in the endothelium of all vascular segments contain the vascular endothelium cadherin (VE-cadherin) and catenin complex as their main component (Dejana, 1997; Schnittler and Feldman, 1999). These structural biological components form the mechanism through which monolayer permeability is largely regulated.

2. Role in Disease

The endothelium plays a key role physiologically, as well as in the development of many different forms of pathology. Some of its many roles include providing a selective barrier for macromolecular permeability, influencing vascular remodeling through the production of growth promoting and inhibiting substances, modulating

homeostasis and thrombosis by secreting procoagulant and anticoagulant substances, mediating inflammatory responses by the expression of adhesion molecules and the production of chemokines and cytokines, and regulating vascular smooth muscle contraction through the release of vasodilators and vasoconstrictors (Chiu and Chien, 2011). Due to the complexity of its functionality, it is not surprising that the endothelium is the focal point for the development of many vascular diseases. Its dysfunction may contribute to the development of atherosclerosis, thrombosis, and their related complications.

Experimental approaches to investigating the barrier function of the endothelium and its regulation have garnered interest in pharmacology because any compound circulating in the blood that needs to interact with cells beyond the vascular wall in order to have systemic or organ-specific effects must cross the endothelial barrier (Wegener *et al.*, 1999). That is why *in vitro* permeability studies on ECs are important to the pharmacology industry – the pharmacokinetic properties of drugs need to be screened for their ability to pass through an endothelial monolayer such as the blood-brain barrier (Youdim *et al.*, 2003). This function represents one of the reasons why forming a detailed understanding of endothelial permeability is of critical importance to the field of medicine as it relates to therapeutic approaches to treating disease.

ECs are extremely important in the process of wound healing as well. When endothelial injury occurs, ECs at the edge of the wound migrate to seal the gap that is formed in the monolayer (Grasso *et al.*, 2007). The understanding of EC motility is crucial for many fundamental processes in biology and pathology because the migration of ECs is an important part of angiogenic processes that are critical to the progression of

many diseases (Lamallice *et al.*, 2007). Other types of cells, such as leukocytes and circulating cancer cells interact with the endothelium through recruitment cascades that lead to transmigration, or extravasation through the endothelium (Young and Simmons, 2010). This process of allowing cells through the endothelium is one example of why it is so important to the field of medicine to understand factors that affect the permeability of the monolayer.

3. Effect of Shear Stress

Research has demonstrated that hemodynamic forces modulate EC morphology and function both *in vivo* and *in vitro*, with endothelial responses to shear stress including electrophysiological changes, transcription factor activation and gene regulation, protein synthesis, and changes in cell structure (DePaola *et al.*, 2001). Many specific studies have shown that shear stress mediates endothelial morphological adaptations (Flaherty *et al.*, 1972), permeability (Kwei *et al.*, 2004), vasoregulation (Melkumyants *et al.*, 1989), arterial remodeling (Langille, 1996), and pathophysiological processes that contribute to the development of atherosclerosis and other cardiovascular diseases (Traub and Berk, 1998). It has become apparent that shear stress has a primary influence on the regulation of endothelial-mediated control of the vasculature. Many review articles have focused on the effect that shear stress has on EC structure and function, signaling events, and flow-induced endothelial mechanotransduction and its mediating mechanisms (DePaola *et al.*, 2001).

ECs are extremely adaptive morphologically in the presence of hemodynamic shear stress, and they have been shown numerous times to elongate and realign with the direction of flow, thus exhibiting great motility in order to reposition themselves within

the monolayer to maintain confluence (Young and Simmons, 2010). The alignment and elongation of ECs in the direction of fluid flow has been shown numerous times *in vitro* (Noria *et al.*, 1999; Girard and Nerem, 1995), and *in vivo* shear-induced responses of EC morphology have included the realignment of cell's long axis parallel to flow from perpendicular (Flaherty *et al.*, 1972). Experimental observations have shown that within a five hour period as part of the dynamic adaptive process towards responding to a new flow environment, ECs start rearranging their intercellular junctions, begin aligning in the direction of flow, and form adhesion plaques (DePaola *et al.*, 2001). Additionally, differential effects of laminar versus disturbed flow patterns have been linked to variations in cell shape as well as to the focal generation of atherosclerotic lesions (Young and Simmons, 2010).

The so-called morphodynamics approach to quantitatively analyzing shear stress-induced morphological changes in ECs with respect to time that Dieterich *et al.* (2000) employed was able to elucidate the different phases that ECs go through in response to the onset and continuation of shear stress exposure. Phase I is characterized by random cell orientation and polygonal cell shape during resting conditions or very low shear stress. Phase II occurs at the onset of shear stress, and it entails a transient increase in cell locomotion. Phase III occurs after a lag period following the onset of fluid flow, and it is the epoch when cells begin to align. Finally, Phase IV occurs within hours and it is the time when cell elongation occurs. The dynamic changes in cellular response that are seen in relation to shear stress point to the need to have real-time monitoring of ECs during flow in order to more fully understand their response.

Also of great interest are the effects of disturbed flow patterns, such as those

characterized by low and reciprocating shear stress, as well as flow separation, recirculation, and reattachment on EC responses. Unsteady shear stress patterns that reverse direction and are low in magnitude elicit different responses than high, steady shear stress created by laminar flow regarding molecular signaling, gene expression, and cell structure and function (Chiu and Chien, 2011). For example, Chiu *et al.* (1998) showed that ECs exposed to disturbed flow with very low mean shear stress values (between 0 and 0.5 dynes/cm²) in a step-flow chamber are round in shape with short actin filaments that are located mainly in the peripheral regions of the cell. Meanwhile, ECs subjected to laminar flow with relatively high shear stress levels (20 dynes/cm²) become aligned in the direction of flow and exhibit long, organized parallel actin stress fibers in their central region. *In vivo* studies have found comparable results, with ECs in low shear stress environments exhibiting peripheral actin microfilaments while high shear stress promotes central actin stress fibers (Kim *et al.*, 1989).

Regarding the aforementioned experiment that examined ECs exposed to disturbed flow in a step-flow channel, the researchers found that the cell turnover rate (mitosis) was higher as compared to cells kept in static conditions (Chiu *et al.*, 1998). Additionally, the observation was made that the DNA synthesis rate of cells in the flow reattachment region of the chamber was higher than in the laminar flow area or under static conditions. Turbulent flow patterns also induce EC turnover *in vitro* (Davies *et al.*, 1986). In contrast, high levels of laminar shear stress inhibit DNA synthesis (Chiu *et al.*, 1998) in addition to EC proliferation. The clear variation in the characteristics of the ECs as a function of the distinct shear stress patterns that groups of cells experience demonstrates the importance of understanding how these different flow environments

alter the endothelium.

4. Permeability

The barrier formed by the endothelium between the flowing blood and the underlying tissues is semi-permeable in the sense that it selectively traffics fluid, solutes, and macromolecular compounds from the vessel lumen to the interstitium in order to maintain gradients of specific proteins and other molecules between the two sides (Young and Simmons, 2010). For example, the intercellular junctions of ECs in the straight parts of the arterial tree do not allow macromolecules such as lipoproteins to pass through when they are intact and functioning normally, but these substances can breach the endothelium during EC turnover (Chiu and Chien, 2011). During normal functioning, these larger molecular substances require vesicular transport through the cell so as to pass in a transcellular fashion, while smaller molecules pass via a paracellular route through endothelial intercellular junctions (Mehta and Malik, 2006). The permeability of the overall endothelium is dependent on the junctional integrity between adjacent cells as well as the density of surface-bound proteins, and because these structures are bound on the intracellular side to the cytoskeleton, it plays a major role in regulating the flux of particles (Young and Simmons, 2010).

Just as there are variations in EC morphology based on anatomical location, there are differences in the permeability of the endothelium depending on vessel type. The ECs in capillaries and in post-capillary venules are more permeable than those in large arteries (Aird, 2007). The permeability of the endothelium changes in response to shear stress. One study showed that the albumin permeability of the monolayer increases following the onset of shear stress, and it also decreases back to its baseline value after

fluid flow is terminated (Jo *et al.*, 1991). This result demonstrates that flow-induced shear stress plays a role in regulating permeability, and it shows that CCF systems that incorporate permeability measurements are valuable to the field of study (Young and Simmons, 2010).

Disturbed flow (as opposed to steady laminar flow) impacts EC morphology, turnover rate, and other biochemical events; it also affects the permeability of the endothelium. Regions of the vasculature such as vessel branch points, where the blood flow is disturbed, exhibit increased permeability to macromolecules (Chiu and Chien, 2011). These *in vivo* observations of the effect of disturbed flow on endothelial permeability have been reproduced in many *in vitro* studies. For example, Phelps *et al.* (2000) used a step-flow channel in order to show that the transendothelial transport of dextran in the area of flow reattachment is significantly higher as compared to that in the laminar flow region.

Based on the results obtained from various studies, it appears that the increased cell turnover found in areas of disturbed flow may provide a mechanism that leads to increased permeability. ECs in disturbed flow regions of the rabbit thoracic aorta *in vivo* have higher turnover rates than those in other anatomical locations where flow is laminar (Davies *et al.*, 1997). Also, the cells in disturbed flow regions of the step-flow chamber likewise exhibit higher rates of mitosis compared to those in other regions where flow is unidirectional (Chiu *et al.*, 1998).

In addition to cell division rates, the modulation of the expression and structure of intercellular junctional proteins such as catenins and VE-cadherin through a disturbed flow-driven mechanism likely provides insight into how these flow patterns increase

endothelial permeability (Chiu and Chien, 2011). Studies performed by creating an experimental constriction in part of the rat aorta show strong staining of VE-cadherin at EC borders where flow is pulsatile with a net forward component as compared to the post-stenotic dilation site where flow levels are lower and reciprocating (Miao *et al.*, 2005). *In vitro* studies by the same group showed that six hour-duration exposure to either low and reciprocating (0.5 ± 4 dynes/cm² at 1 Hz) or pulsatile (12 ± 4 dynes/cm² at 1 Hz) flow disrupts VE-cadherin and its associated protein β -catenin at cell borders. However, the researchers found that these junctional molecules once again become continuous along cell borders after twenty-four hour exposure to pulsatile, but not reciprocating flow. Irregular distributions of gap junction proteins are also observed in areas of disturbed flow, which may contribute to increased macromolecular permeability of the endothelium (Chiu and Chien, 2011).

It appears that it is not solely disturbed flow, but also the diminution or total lack of flow that increases endothelial inter-cell permeability. ECs exposed to strong laminar flow show the strong expression of tight junctions, while cells in low shear stress environments display lower expression levels thereof (Yoshida *et al.*, 1995). Static culture conditions cause tight junctions to be either poorly developed or completely absent from macrovascular ECs *in vitro* (Craig *et al.*, 1998). Additional evidence that lends itself to the hypothesis that sustained flow improves monolayer barrier function was found by Yoshida *et al.* (2005) when the group demonstrated an increase in tight junction formation in ECs after twenty-four to forty-eight hours of shear stress exposure. Taken together, these observations support the notion that shear stress has a large impact on endothelial barrier function, and that the study of flow as it relates to the dynamic

alterations of permeability of the monolayer is a worthwhile endeavor.

5. Flow Effects on Pathology

Although the involvement of the vascular endothelium in pathogenic processes such as atherosclerosis was established long ago, more recent investigations have implicated shear stress-dependent effects on the endothelium as contributing to the ability of certain known risk factors to manifest themselves in cardiovascular disease (Traub and Berk, 1998). Certain types of hemodynamic forces are necessary for the proper physiological functioning of ECs, and others can induce dysfunction through adverse effects on cell signaling and gene expression, which may contribute to the generation of vascular pathologies (Chiu and Chien, 2011).

Over time, evidence has mounted that low shear stress is a factor that contributes to the development of atherosclerosis (Davies *et al.*, 2005). This claim is supported in part by the observation of preferential plaque formation at arterial branches and curvatures where local flow is characterized by recirculation eddies and changes in direction, in addition to the activation of atherogenic genes in the ECs subjected to low and reciprocating shear stress *in vivo* (Chiu and Chien, 2011). Meanwhile, it is known that the straight part of the arterial vasculature, which is exposed to sustained laminar blood flow, is generally spared from atherosclerotic lesions with the coincident up-regulation of anti-oxidant and growth arrest genes in ECs. Thus, laminar and disturbed flow patterns appear to contribute to protection against or increased likelihood of atherosclerosis, respectively. Shear stress, acting through effects on endothelial gene expression, has been implicated as a modulating factor that results in this phenomenon (Davies *et al.*, 2005).

Observations made *in vivo* demonstrate that relative changes in shear stress as opposed to absolute levels have a major effect on vascular homeostasis and remodeling (Chiu and Chien, 2011). A study in which blood flow to the common carotid artery of rabbits was reduced by 70% resulted in a 21% decrease in diameter within a two-week period (Langille and O'Donnell, 1986). This arterial constriction was shown to be endothelium-dependent because it was not relieved by a vascular smooth muscle cell (SMC) relaxant, suggesting that structural changes in the vessel wall occurred as opposed to SMC contraction. Arterial remodeling responses to shear stress level changes require an intact, functional endothelium, and they act so as to make compensatory alterations that maintain a range of mean shear stress levels in the arterial system of approximately 15-20 dynes/cm² (Chiu and Chien, 2011).

There is a series of bicuspid valves located throughout the superficial and deep veins in the human body that are responsible for preventing the reflux of blood when standing in the upright position (Chiu and Chien, 2011). However, the reflux of blood through dysfunctional valves may contribute to venous hypertension, which may in turn cause EC dysfunction and inflammation, ultimately leading to the development of varicose veins, deep vein thrombosis, and chronic venous insufficiency (Bergan *et al.*, 2006). Changes in hemodynamic forces impacting the vein wall such as shear stress may induce inflammation, and subsequently the remodeling of venous walls and valves, contributing to varicose veins and other venous pathologies (Pascarella *et al.*, 2005). A specific example that links altered shear stress, the endothelium, and venous disease is a study performed by Bergan *et al.* (2008). The study involved a surgical alteration to produce venous hypertension and altered shear stress, which led to an inflammatory

reaction in the vein wall driven by endothelial activation and neutrophil infiltration, resulting in thrombus formation. Taken together, these examples involving both the arterial and venous systems illustrate how hemodynamic forces modulate EC responses and lead to pathological states involving atherosclerotic plaque formation, thrombosis, as well as vascular remodeling (Chiu and Chien, 2011).

Further research has demonstrated some of the cellular mechanisms through which shear stress contributes to endothelial dysfunction. The vascular geometries that induce disturbed flow patterns with a low net forward component such as branch points and curvatures lead to impaired endothelial nitric oxide (NO) production, while laminar flow in the straight segments of arteries maintains vascular homeostasis and increases NO release by ECs (Cooke, 2003). Because NO production is diminished by disturbed flow, the endothelium-dependent vasodilation of coronary arteries is impaired at branch sites (McLenachan *et al.*, 1990), which has serious implications for cardiac health. Given the links that have been established between hemodynamic effects such as disturbed flow patterns and endothelial dysfunction, further research may be able establish the direct mechanisms that predispose specific vascular regions to pathophysiological processes and help contribute to hemodynamic-based strategies for preventing and treating both the underlying cause of, as well as the complications resulting from, atherosclerosis and thrombosis (Chiu and Chien, 2011).

6. Barrier Function Effects on Pathology

Disturbed shear stress profiles and their contributions to monolayer gap formation and cell loss from the substrate *in vitro* have been detailed in previous studies (Davies *et al.*, 1986; DePaola *et al.*, 1992). Several studies have made note that atherosclerotic

plaques tend to form at sites of low shear stress and flow separation *in situ* (Ku *et al.*, 1985) where increased endothelial permeability occurs (Yoshida *et al.*, 1995). These data may help elucidate the mechanisms by which disturbed flow, acting through effects on the endothelium, spur the formation of plaques in regions of disturbed flow *in vivo* (Seebach *et al.*, 2000).

Pathological conditions other than atherosclerosis are associated with increased endothelial permeability as well. For example, the loss of intercellular junctional integrity and hence barrier function often indicates a breach in the monolayer and a subsequent inflammatory processes (Young and Simmons, 2010). SMC proliferation and excess matrix protein synthesis cause lesions in arterial walls, and these processes are usually initiated by endothelial dysfunction and inflammatory cell recruitment, which involves an increase in monolayer permeability (Doran *et al.*, 2008). The implication of the role of EC permeability in pathology indicates the need to study these phenomena in the context of their contributions to disease states, as opposed to simply the effects of shear stress alone.

B. Measurement Systems

1. General Considerations

Given the importance of the endothelium to various biological processes, it makes sense that methods would be developed to objectively measure cellular functions and properties. The use of animal experimental models comes with not only ethical but also experimental drawbacks, and so various *in vitro* techniques, many of which involve the culture of ECs on porous membranes, serve as alternative methods for assessing barrier

function (Wegener *et al.*, 1999). However, many other modalities of culturing ECs have been demonstrated successfully as a means to quantitatively measure certain aspects of EC behavior when subjected to various types of stimuli. One example of the benefits that could be reaped from using novel cell culture models is the ability to monitor morphological changes quantitatively in real-time during drug screening experiments (Wegener *et al.*, 1999).

The study of mechanical-biological reactions of ECs requires engineered tools to maintain cultures in controlled environments while exposing them to mechanical stimuli (Young and Simmons, 2010). Many microfluidic approaches have been pursued for this purpose. These systems benefit from the advantage of having small length scales that require minute sample volumes; they can often be fabricated using soft lithography allowing fast turnaround times from design to implementation (Li *et al.*, 2003). These types of systems benefit from geometries that guarantee low Reynolds numbers and laminar flow patterns (Young and Simmons, 2010). Because the fabrication process involving elastomeric replica molding allows for straightforward fabrication (Li *et al.*, 2003), it is simple to produce multichannel networks of varying configurations (Young and Simmons, 2010). While this process allows for highly integrated microfluidic circuits, the alignment of features in separate patterning steps is difficult compared to traditional photolithography because of the flexibility of elastic materials such as polydimethylsiloxane (PDMS) (Li *et al.*, 2003).

Flow studies on ECs have traditionally been performed with analyses including immunostaining, mRNA and protein extraction, and culture media collection for molecular secretion measurements (Young and Simmons, 2010). These metrics are

difficult to study with the miniscule sample volumes involved in microfluidic studies. Additional concerns are drawn from studies that have shown that PDMS can absorb hydrophobic molecules (Toepke and Beebe, 2006), and that uncrosslinked oligomers can leach out from bulk PDMS into cell culture media (Regehr *et al.*, 2009). Most macro-scale CCF systems are built for reliable long-term use with materials that are usually autoclaveable and optically transparent for visualization; however, the devices designed by micro-scale engineers have the tendency to be too cumbersome and complex for transition to another lab, limiting the marketability and portability of these designs (Young and Simmons, 2010).

Macro-scale systems are not without their own drawbacks. They usually require large amounts of dedicated lab space and reagent volumes, and they are best suited for labs focused on endothelial studies where targeted molecules can be analyzed in-house and high-throughput is not necessary (Young and Simmons, 2010). Meanwhile, researchers using microfluidic approaches may benefit from the ability to do complex cellular manipulations and analyses on a fully integrated platform using lab-on-a-chip approaches (Yeo *et al.*, 2011). However, micro-scale CCF systems have the burden of their own set of biological concerns that come along with the high surface area-to-volume ratios involved in these devices: faster nutrient depletion and waste accumulation as well as the potential increase in the sensitivity of cellular populations to minor fluctuations in culture conditions may adversely affect biological outcomes (Young and Simmons, 2010). What biologists need from engineers is a focus on designing devices for ease of use from an end-user perspective, an emphasis on standardization methods for repeatable applications, and evidence of fidelity in extrapolating established macro-scale results to

the micro-scale environment. Also, considerations should be made to allow for quantitative real-time measurements of the endothelium throughout the course of a study (Wegener *et al.*, 1999), as opposed to merely end-point biochemical measurements that are limited to specific molecular markers and do not assess barrier function more directly.

2. Adhesion Assay

Adhesion assays measure the attachment strength between anchorage-dependent cells and their underlying substrate using two methods: 1) counting the fraction of cells that detach after exposure to a specific shear stress level, and 2) formulating an estimate of the total force per bond between a cell and the substrate (Young and Simmons, 2010). These assays use CCF systems to quantify the affinity and binding strength of cells on a specific surface so as to improve the understanding of adhesion properties and cell-matrix interactions.

The first method is a general measure of adhesion strength that assesses the overall preference of a certain cell type for a particular surface, whereas the second method is a specific measure of bond strength requiring knowledge of the number of bonds between each cell and the substrate as well as the contact area of the cells and models to estimate bond and force distributions (Young and Simmons, 2010). Parallel plate flow chambers (PPFCs) are the CCF system traditionally used for carrying out adhesion assays (Olivier and Truskey, 1993). The use of a PPFC to perform an adhesion assay involves loading cells into the device, allowing them to adhere, and then incrementally increasing shear stress to ramp the force dissociating cells from the substrate (Young and Simmons, 2010). The PPFC is created by sealing a gasket with a rectangular contact area to a glass slide and leaving two openings at either end of the chamber, which results in a uniform

channel height along the path of flow (Chiu and Chien, 2011). Because the flow chamber is uniform throughout the device and a given sample is treated with only one condition at any given moment, these types of devices are limited to the study of one experimental condition at a time (Young and Simmons, 2010).

Because of this limitation, PPFCs have been modified to taper height or width along the path of flow to generate variable levels of shear stress at different locations within the chamber (Xiao and Truskey, 1996). Radial and circumferential flow patterns have also been used in adhesion assays to create shear stress ranges from non-uniform velocity fields (Young and Simmons, 2010). Radial flow designs utilize divergent flow from a central point, or convergence to a sink. Circumferential flow produces shear stress gradients in a radial direction. Designs to produce these types of fluid motion can be described as radial flow chambers (Goldstein and DiMilla, 2002), and spinning disk apparatuses (Horbett *et al.*, 1988). Besides the drawback of difficulty in producing multiple levels of shear stress in one device, CCF systems designed to measure adhesion with regards to individual bond strength may require significant modifications to enable microscopic visualization for estimating cell-to-surface bond areas (Young and Simmons, 2010).

For a given experiment using the PPFC to steadily increase shear stress until cells dissociate from the substrate, the flow rate must be adjusted manually (often by changing settings on a syringe pump) (Young and Simmons, 2010). This inconvenience is another drawback of these types of assays. Microfluidic approaches have provided increased efficiencies of experimentation by enabling experimenters to test multiple conditions in parallel, such as the method developed by Kantak *et al.* (2003) wherein different

substrate coatings were used in four individual microchannels on the same chip. This configuration, however, required the use of multiple syringes to avoid cross-contamination. The use of multiple parallel microchannels within a network makes it possible to avoid the need for more than one syringe hook-up, but it opens the possibility of cross-contamination at branch-points (Young and Simmons, 2010). Finally, Gutierrez and Groisman (2007) employed a network of microchannels each of which produces variable shear stress levels in parallel, thus allowing both continuous variation in fluid dynamic conditions to be created along with other distinctions in experimental conditions among separate cell populations in the network.

3. Migration Assay

Migration assays are intended to quantify cell motility by measuring the speed of transit through a barrier or membrane, across a two-dimensional surface, or within a three-dimensional gel or scaffold (Young and Simmons, 2010). The most common means of testing motility is the use of a trans-well migration assay (also called a Boyden chamber assay), wherein cells are cultured on one side of a porous membrane and attracted to the other side by chemotaxis where fluorescence is usually used for detection (Chen, 2005). These assays are popular for studying EC function by culturing a monolayer on the membrane with the use of leukocytes or cancer cells as the migrating cell because it simulates the process of extravasation of these circulating cells *in vivo* (Young and Simmons, 2010).

The other type of migration assay usually tracks the movement of cells along a two-dimensional surface, which is biologically relevant because ECs will typically migrate in order to maintain confluence over the substrate (Young and Simmons, 2010).

Specific implementations of this assay include the Teflon fence assay, where an obstacle on the plane is removed allowing migration into an open area (Pratt *et al.*, 1984), and the scratch assay, a type of wound healing study where a fully confluent EC layer is scratched and migration is initiated to fill in the gap in the monolayer (Weber *et al.*, 1999).

The migration assay can be improved by incorporating shear stress effects on ECs so as to increase the biological relevance of the study by observing behavior under fluid flow (Young and Simmons, 2010). The combination of the assay with shear stress effects has been achieved by incorporating a bar into the path of flow in a PPFC to generate shear stress gradients and induce EC migration (Tardy *et al.*, 1997). In a similar fashion for wound healing studies, EC monolayers have been scratched before being exposed to fluid flow in a PPFC (Albuquerque and Flozak, 2001).

In addition to fluorescent detection, cells can be monitored in migration assays by time-lapse video microscopy (Young and Simmons, 2010) or by using the morphodynamics approach of Dieterich *et al.* (2000). Possible concerns involved with using fluid flow to produce chemical gradients (as is often done by mixing laminar fluid streams in microchannels) for chemotactic studies is that shear stress effects may obscure or confound results that are intended to measure cell migration towards a chemical source. Researchers found recently that shear stress gradients in a microchannel can spur migratory responses from cells (Young and Simmons, 2010).

4. Shear Stress Response Studies

Studies of the fundamentals of how shear stress affects ECs have mostly utilized CCF systems for controlled *in vitro* experiments that attempt to mimic physiological

conditions while reproducing observations made *in vivo* (Young and Simmons, 2010). The use of pulsatile flow with a clear direction allows for an analysis of the cellular and molecular bases of mechanotransduction under flow conditions that simulate what actually occurs in the vasculature (Chiu and Chien, 2011). Morphological responses such as the elongation of cells in the direction of flow have become validation measures for determining whether CCF systems such as PPFCs can reproduce observations made *in vivo* with fidelity (Young and Simmons, 2010). A variety of systems have been developed for applying shear stress to ECs *in vitro* in order to study the mechanisms of their responses under these conditions; such systems include PPFCs, cone-and-plate viscometers, parallel disk viscometers, orbital shakers, and rectangular or tubular capillary tubes (Chiu and Chien, 2011).

Most of these studies revolve around the careful selection of shear stress magnitudes and waveforms to mimic physiological conditions and to allow for the straightforward determination of effects on cell monolayers, with laminar steady flow as the most common choice because of the simplicity of calculating theoretical shear stress values (Young and Simmons, 2010). PPFCs and cone-and-plate viscometers produce uniform shear stress levels on ECs and involve large enough cellular populations to yield sufficient biological material for traditional endpoint assessments of molecular signaling and gene expression (Chiu and Chien, 2011). These biochemical analyses of ECs that have been studied as responses to shear stress include protein synthesis, and production and secretion of vasodilators, vasoconstrictors, thrombogenic factors, and cytokines (Young and Simmons, 2010).

Some of the benefits of the PPFC device result from the geometry being simple,

which allows for the analytical solution of velocity and pressure fields based on the theory of viscous flow in ducts (Young and Simmons, 2010). Additionally, the equipment permits easy media sampling and exchange as well as cell culture accessibility both physically and for microscopic visualization (Brown, 2000). The cone-and-plate viscometer consists of a mechanism that generates flow by the rotation of a cone around its axis, which is oriented perpendicular to the surface of a flat plate (Chiu and Chien, 2011). Because both the local relative velocity and separation between the cone and plate surfaces varies linearly with radial position, a spatially homogeneous level of shear stress is produced on both surfaces (Brown, 2000). Some of the benefits of using a cone-and-plate viscometer include the feasibility of doing microscopic visualization (although it can be somewhat cumbersome), and the small fluid volume required (Chiu and Chien, 2011).

Blood flow during the cardiac cycle is pulsatile, so other experiments have employed unsteady flow waveforms such as oscillatory and non-reversing pulsatile in order to examine the dynamic effects on ECs of pulsatility variables such as frequency, amplitude, and degree of flow reversal (Helmlinger *et al.*, 1996). Reciprocating flow pumps have been used in conjunction with PPFCs to study the effects of this type of unsteady shear stress on ECs (Hsu *et al.*, 2001). However, the use of oscillating flow within the standard PPFC does not allow for the study of the responses of ECs to multiple flow patterns in the same device simultaneously (Chiu and Chien, 2011). The drive-mechanism of a cone-and-plate viscometer has been modified so as to produce pulsatile shear stress waveforms. Blackman *et al.* (2002) pursued this approach with a process that produced a dynamic, arterial-like waveform of fluid flow that mimics the conditions in

the human aorta. This use of the cone-and-plate viscometer still subjects the entire cell population to only one shear stress waveform.

As mentioned in the section on the adhesion assay, the modification of the PPFC to employ a tapered channel has provided a means of varying shear stress levels linearly along the path of flow as in the device used by Usami *et al.* (1993). While this type of device can enable the study of the effects of more than one shear stress level within one experimental trial it is still limited to steady flow waveforms that do not vary with time. The use of more complex, disturbed flow patterns has been achieved with the PPFC by placing a vertical step near the inlet (creating a backward-facing step-flow) and with the cone-and-plate viscometer by placing a rectangular obstacle (Chiu and Chien, 2011). The flow profile in the step-flow channel is characterized by a recirculation eddy immediately downstream of the step, followed by a region of flow reattachment, and then a unidirectional laminar flow that is reestablished further downstream (Hsu *et al.*, 2001). Although the EC responses to both laminar and disturbed flows can be studied in a step-flow channel, it is difficult to use standard immunostaining techniques to analyze the effects of the disturbed flow pattern because the local fluid dynamic environment in the channel varies with a length scale of only tens to hundreds of micrometers and thus only a few cells are exposed to flow disturbances (Chiu and Chien, 2011).

Other tools used to study EC responses to fluid flow include capillary tubes, which do not yield enough biological material for some bioassay analyses, and parallel disk viscometers and orbital shakers, both of which result in variable shear stress levels across the monolayer surface (Chiu and Chien, 2011). Orbital shaker shear stress studies usually employ standard cell culture dishes in which cells are seeded, grown and

contained using traditional methods (Dardik *et al.*, 2005). These dishes are then placed upon an orbiting surface that induces fluid flow within the dish. Unlike the cone-and-plate viscometer of Blackman *et al.* (2002), which relies on a micro-stepper motor and timing belt to achieve an arterial-like shear stress waveform, the advantages of using an orbital shaker include not only variable shear stress levels at different radial positions, but also pulsatile fluid flow that occurs as a result of the orbital motion without sophisticated equipment.

Microfluidics represents another means to overcome the shortcomings of only being able to test one condition at a time encountered with PPFC and cone-and-plate viscometers, potentially by creating a more high-throughput method to expedite the experimental process (Young and Simmons, 2010). While these microfluidic systems allow for low Reynolds numbers and guaranteed laminar flows, attention must be paid to channel aspect ratios to ensure that wall effects on velocity profiles do not interfere with the generation of desired shear stress levels. Furthermore, the aim of many of the traditional CCF devices (PPFCs and cone-and-plate viscometers) is to allow for the collection of enough cells for analysis by a variety of bioassays (Chiu and Chien, 2011), and microchannels may not contain enough cells for these purposes. Another major challenge of performing shear stress response studies with microfluidic devices is the need for long-term viability of the cells, which is not necessary in adhesion assays, and the need to achieve a confluent monolayer of cells with proper cell-to-cell contacts, the absence of which has been demonstrated to impact the normal cellular response (Young and Simmons, 2010).

5. Permeability Assay

The goal of permeability assays is to assess the structural integrity of an endothelial monolayer regarding its ability to prevent the flux of particles from the luminal to the abluminal side. Two methods are used for this purpose: 1) tracking the movement of specific molecules from one side to the other, and 2) measuring transendothelial electrical resistance (TER) by passing a current, measuring a voltage across the monolayer, and using Ohm's law (Young and Simmons, 2010). The first method is a direct measure of the barrier function of the monolayer because the flux of specific particles is tracked and quantified. The second method is based on the assumption that the endothelial monolayer can be treated as an obstacle that impedes the flow of electrical current. To carry out these studies, endothelial cells are grown on a porous membrane to separate the compartment above (luminal) from that below (abluminal). This method has been applied successfully to mimic both the micro- and macrovasculature of the body (Wegener *et al.*, 1999). Specifically, ECs are usually grown on inserts bearing the membranous material, the insert is then placed in a well plate, and the molecule that is most commonly tracked across the monolayer in the first type of study is albumin (Young and Simmons, 2010). The permeation rate of the protein or molecule is usually quantified by labeling the substance with radioisotopes of fluorescence chromophores (Wegener *et al.*, 1999).

The combination of shear stress response studies with permeability assays is useful because it has been demonstrated that albumin permeability increases at the onset of shear stress and it decreases back to baseline after fluid motion is terminated, suggesting that flow-induced shear stress regulates permeability (Jo *et al.*, 1991), and that

CCF systems that incorporate permeability measurements are valuable (Young and Simmons, 2010). Despite this finding, not many studies have focused on the shear stress-dependent modulation of endothelial barrier function. Aside from shear stress, the endothelial permeability can be tested under the influence of various types of chemical and mechanical stimuli in comparison with a control in order to gain insights into the mechanisms that underlie endothelial barrier function.

The incorporation of shear stress effects into a permeability study is usually somewhat difficult from an experimental standpoint because hydrostatic pressure must be precisely controlled in the luminal and abluminal fluid compartments while producing fluid flow through the region above the cells and simultaneously allowing access to the region below the cells for chemical sampling purposes (Young and Simmons, 2010). A precise level of transendothelial pressure must be maintained during subjection of the monolayer to shear stress in order not to skew the detection of permeability. Hence, the complexity of these systems often means that they are limited to labs dedicated solely to endothelial studies where target molecules can be analyzed and high-throughput studies are not necessary.

Measurements of the electrical resistance of tissues have traditionally been used to evaluate the barrier function of epithelial cell layers that form the interfaces between biological compartments in the body (DePaola *et al.*, 2001). It has now become very common to determine the TER of confluent cell layers as a direct measure of the barrier properties of endothelial monolayers (Wegener *et al.*, 1999). ECs still must be cultured on a supporting porous membrane in the same way that they are for other types of permeability assays, and for this purpose trans-well cell culture inserts can be seated in

standard cell culture well dishes while cell growth occurs followed by the relocation of the inserts to the apparatus that is used to make the TER measurements (Young and Simmons, 2010). The fact that cell culture well inserts must be transferred from their original environment to the apparatus is somewhat inconvenient and increases the likelihood of contamination. Additional complications can arise when performing TER measurements of macrovascular endothelial cells because of the typically low resistance of this cell type (less than $5 \Omega\text{-cm}^2$) (DePaola *et al.*, 2001). This low value makes it difficult to distinguish between the resistances of the cell layer itself and those of the bathing cell culture media and the cables connecting to the device measuring resistance, all of which are arranged in series. This problem represents a drawback of using this widespread DC technique. It is of note that the authors of a review article on macro- and microscale fluid flow systems stated that they were not aware of any studies using microfluidic devices to study EC permeability (Young and Simmons, 2010).

C. Impedance Sensing

1. Origination

Although many studies of ECs that analyze the shear stress-induced effects seek to target endpoint measures of secreted factors, protein, and mRNA, the viability of using these elements as experimental outcomes is limited to the use of cultures large enough to produce adequate biological material for analysis (Young and Simmons, 2010).

Additionally, these types of biochemical measures can only elucidate the state of cellular activity at the end of some predetermined time period versus a control, and they do not provide real-time insight into the dynamic changes that cells undergo throughout the

course of shear stress exposure.

Many studies seek to gain insights into the structure and morphology of ECs subjected to shear stress as their outcome measures (Young and Simmons, 2010). Levesque and Nerem (1985) showed that morphological responses of cells in the form of elongation and preferential orientation in the direction of flow require twenty-four to forty-eight hours before the alterations can be detected. Some adaptations such as the full restoration of linear adherens junctions at the borders of ECs after exposure to shear stress may take up to ninety-six hours to complete (Noria *et al.*, 2004). However, other cellular reactions to fluid flow, such as the regulation of specific shear stress response elements may occur in less than six hours (Davies *et al.*, 1997). Furthermore, some endothelial responses to shear stress have a time frame that varies from seconds to hours (DePaola *et al.*, 2001). For example, the quantitative analysis of shear stress-induced morphologic changes of ECs as a function of time, called morphodynamics, showed that there is a rapid down-regulation of cell fluctuations (zigzag movements) and a transient increase in locomotion following the onset of shear stress (Seebach *et al.*, 2000).

The technique of morphodynamic analysis, while able to detect cellular changes in real-time, still has some limitations. The measurement of electrical impedance values as a function of time has been used historically in bioimpedance investigations to examine the frequency dispersions of biological tissues (Rahman *et al.*, 2009). Giaever and Keese (1991) developed a method to detect changes in cell morphology in real-time called ECIS, which they touted as being less difficult and time-consuming than recording time-lapse video microscopy and processing large amounts of data. Another advantage over microscopic observations that the authors suggested was a level of sensitivity that

could detect changes in cell diameter on a nanometer scale or subnanometer changes in the distance between the ventral surface of the cell and the substrate – beyond the resolution of optical microscopy.

ECIS is based on electrochemical impedance spectroscopy (also called impedimetric sensing), which has been used for various types of biosensing applications, and a subset of this type of impedimetric sensing that is cell-based in nature makes use of living cells for detecting such things as environmental conditions, cell-drug interactions, and infections (Ziegler, 2000). ECIS and most other cell-based impedimetric biosensors work based on alterations of the electrical impedance of the electrode-cell interface as a result of the adhesion and motility of anchorage-dependent cells such as ECs (Rahman *et al.*, 2009). Giaever and Keese originally demonstrated the use of ECIS to monitor the adhesion and locomotion, permeability, change in shape, and alteration in function under various drug and biochemical treatments of WI-38 fibroblasts (Giaever and Keese, 1991; Giaever and Keese, 1993).

2. Background

Electrochemical impedance spectroscopy is traditionally based on the principle of applying an AC voltage of a known frequency and amplitude to a system and recording the amplitude and phase-shift of the output AC current (Gamry Instruments, 2008). The excitation signal can be expressed as a function of time in the form:

$$E(t) = E_o \sin(\omega t) \quad (1)$$

where $E(t)$ is the applied potential at time t , E_o is the amplitude of the signal, and ω is the

radial frequency (in radians/second). The radial frequency can be expressed in terms of the frequency, f (in Hertz) as:

$$\omega = 2\pi f \quad (2)$$

The output current can be expressed by the following function:

$$I(t) = I_o \sin(\omega t + \phi) \quad (3)$$

where $I(t)$ is the output current at time t , I_o is the amplitude of the signal, ω is the radial frequency (in radians/second), and ϕ is the phase-shift angle. The impedance, Z , can then be given as an expression analogous to Ohm's Law as:

$$Z = \frac{E(t)}{I(t)} = \frac{E_o \sin(\omega t)}{I_o \sin(\omega t + \phi)} = Z_o \frac{\sin(\omega t)}{\sin(\omega t + \phi)} \quad (4)$$

where Z_o is the impedance magnitude, and ϕ is the impedance phase-shift angle. In this case the impedance is described in terms of magnitude and phase, but it can also be expressed as a complex value (Gamry Instruments, 2008). The input-output response relationship of electrochemical systems is not linear, so in normal practice the amplitude of the applied voltage is kept low enough to make the system pseudo-linear. The amplitude of the input AC voltage is typically in the range of 1 to 10 mV to meet this requirement.

The ECIS method of Giaever and Keese (1991) is a slight variation on

electrochemical impedance sensing. In their system, one of four small ($\sim 10^{-3} \text{ cm}^2$) electrodes and one large ($\sim 2 \text{ cm}^2$) electrode on the bottom of the cell culture dish were connected to a phase-sensitive lock-in amplifier with the cell media electrolyte solution completing the circuit (Giaever and Keese, 1991). A 4 kHz AC voltage source of 1 Volt-amplitude was then applied across a $1 \text{ M}\Omega$ resistor to obtain an approximate constant current source. Treating the system as a series resistor and capacitor, the in-phase and out-of-phase voltages that are output are approximately proportional to the resistance and capacitive reactance, respectively. The model assumes that resistive currents can flow between the ventral surface of the cells and the substrate as well as between the cells, and that capacitive currents can flow through the cell membrane. The resistance of the tissue culture media appears in series with the impedance of the electrodes and any attached cells, and it dominates the measurement except when one of the electrodes is sufficiently small. Giaever and Keese (1991) asserted that in this case, the resistance due to the small electrode is several times larger than the resistance through the media, and the impedance of the attached cells is clearly revealed. Additionally, the result of differences in the area of one electrode versus another, when great enough, will cause the overall impedance to be dominated by the smaller electrode, the cell layer on top, and the media completing the circuit, while contributions due to the larger electrode will be negligible (Wegener *et al.*, 1999).

Giaever and Keese (1991) noted that as WI-38 fibroblasts attach and spread on top of the smaller electrode, they constrict the effective area available for current to flow, causing as large as an eight-fold increase of the systems overall impedance. Fluctuations continue after the cells have reached full confluence and stop growing at the onset of

contact inhibition (Gaiever and Keese, 1993). These continual variations in impedance were attributed to vertical motions of the cells and changes in the resistance of cell layer. By measuring both the in-phase and out-of-phase voltages and applying cell model calculations, the authors claimed that these two effects could be isolated.

Based on knowledge of the resistivity of the media, the capacitance of the cell membrane, and the average diameter of the cells, the authors applied certain simplifying assumptions to the overall shapes of the cells, modeling them as circular disks or rectangles with widths equal to the diameters used (Gaiever and Keese, 1991). They used these models for cell shape and dimensions to deduce information about spacing between the ventral cell surface and the substrate, as well as the resistance of intercellular gaps. The calculated distances from the substrate agreed reasonably well with data from interference reflection microscopy, but they were found to be highly dependent on the assumed cell shape. Their cell model calculations showed that an average change of less than one nanometer in the distance separating the ventral surface of the cells and the substrate could be discerned, far outpacing the ability of optical microscopes, and thus offering excellent sensitivity in real-time, making ECIS a unique measure of cell morphology and motility while at the same time allowing the evaluation of multiple factors in a single experimental trial. An example they cited was the ability to differentiate the effects of various attachment proteins on the cell layer resistance (Gaiever and Keese, 1993). For this evaluation, distinct electrodes were coated with individual proteins and data was obtained for each one during the same experiment.

3. Basics of Implementation

The TER of a confluent monolayer of ECs can vary from $3 \Omega\text{-cm}^2$ to greater than

1000 $\Omega\text{-cm}^2$ depending on the specific cell type (Seebach *et al.*, 2000). Because the determination of TER by traditional permeability assays with trans-well cell culture inserts is difficult when the cell layer resistance is low (DePaola *et al.*, 2001), ECIS offers a means of identifying the value of this impedance parameter in a fashion that is more generally applicable (Wegener *et al.*, 1999). Since the initial development of ECIS, advancements and adaptations of the technique have continued to improve on the original implementation. Giaever and Keese (1991) briefly described a mode of impedance sensing where multiple AC frequencies are passed through the cell layer, but most of the data they reported was based on detecting impedance at a single frequency (4 kHz). Tiruppathi *et al.* (1992) applied this single-frequency technique to observe the responses of pulmonary microvessel and artery cells to stimulation with thrombin.

Aside from monitoring changes in the real and imaginary components of impedance at a single frequency, the parameterization of the electrode-cell system at multiple distinct frequencies has also been employed, although to a lesser extent (Rahman *et al.*, 2009). Hence, the impedance of the electrode with adherent cells on its surface can be determined at one frequency as a function of time, or as a function of frequency in a spectrometric mode (Wegener *et al.*, 1999). Additionally, advancements have been made to the cell model assumptions used in the original ECIS implementation, and these variations of the simplifications used by Giaever and Keese have continued to advance the understanding of the physico-chemical environment found at the cell-electrode interface (Rahman *et al.*, 2009). One example was the model that Lo and Ferrier (1998) employed, which approximated the cell shape as a rectangle with two semicircular half-disks attached at either end. By using this model to calculate the

separation in between adjacent cells as well as the distance between cells and the substrate, they were able to demonstrate that cell-substrate separation increases with temperature and that the change is reversible.

Important design considerations that are necessary to ensure valid impedance sensing include having the proper area ratio of the small electrode to the large electrode so that the contributions of the larger electrode are negligible (Wegener *et al.*, 1999). The small electrode is commonly referred to as the recording (or working) electrode (RE), and the larger electrode is called the counter electrode (CE). A modification of the original ECIS device that Giaever and Keese used that contains eight recording electrodes instead of four is called ECIS-8W1E, and it has a RE to CE area ratio of approximately 1:300 (RE size of 0.049 mm^2 , and CE size of 18 mm^2) (Rahman *et al.*, 2009). The impedance sensing device developed by Wegener *et al.* (1999), which has three recording electrodes and one counter electrode uses a recording electrode to counter electrode area ratio of approximately 1:100 (RE size of 3 mm^2 , and CE size of 380 mm^2). The RE area and the RE:CE ratio are key design parameters that must be set properly so that the impedance of the cell layer is not masked by the resistance due to the cell culture media (Giaever and Keese, 1991; Wegener *et al.*, 1999). The bipolar impedance of the RE/CE configuration of ECIS encompasses the interactions of the electrode-electrolyte interface, the cell layer, and the measurement leads and insulator-coated portions of the electrodes (Rahman *et al.*, 2009). Hence, accurate data modeling and analysis techniques are necessary to extract the parameters of these various components of the overall system.

4. Circuit Models and Frequency Response

The ECIS method of Giaever and Keese (1991) modeled the electrodes, cell layer,

and culture media as a simple series resistor and capacitor, and in order to obtain an accurate overall representation of the physical parameters of the cells, they had to make assumptions about cell shape. Since the original development of ECIS, advances have been made that improved on the accuracy and validity of the technique. These improvements have included more sophisticated circuit models and the extension of the single-frequency detection of impedance to a spectrometric mode (Rahman *et al.*, 2009; Wegener *et al.*, 1999). A diagram of the electrical network used by Giaever and Keese (1991) is shown in Figure 1.



Figure 1. A schematic representation of the circuit model that Giaever and Keese (1991) used to represent the electrochemical system. R is a resistor, and C is a capacitor.

A key improvement has been a more physically realistic model of the electrochemical behavior of the electrode-electrolyte interface. For an ideally polarizable electrode (with no charge transfer across the surface) in contact with a conductive solution, the impedance of the element should be well modeled by that of a parallel plate capacitor. The impedance of this circuit component is given by the following equation:

$$Z = \frac{1}{i\omega C} \quad (5)$$

where Z is the impedance, i is the imaginary number, ω is the radial frequency (in radians/second), and C is the capacitance (Gamry Instruments, 2008). However, in most

practical situations, capacitive effects in electrochemical environments are modeled by the constant phase element (CPE), and it is misleading to model the interfacial electric double layer that forms at the electrode-electrolyte surface with a capacitor (Rahman *et al.*, 2009). This simplifying assumption causes a modeling error that influences all parameters of the system (Zoltowski, 1998).

The deviation of the electrochemical behavior of the electrode from that of a capacitor has been attributed to surface roughness effects and chemical inhomogeneity in the electrode's uppermost molecular layer (Wegener *et al.*, 1999). The impedance of a CPE is expressed by the following equation:

$$Z_{CPE} = \frac{1}{(i\omega)^n A} \quad (6)$$

where Z_{CPE} is the impedance of the CPE, A is the magnitude of the element, i is the imaginary number, ω is the radial frequency (in radians/second), and n is a parameter that is referred to as the power factor, the value of which is somewhere between zero and one such that if $n = 1$, the impedance of the CPE is the same as that of an ideal capacitor, and if $n = 0$, the impedance of the CPE is the same as that of an ideal resistor (Rahman *et al.*, 2009).

The impedance of the electrode-electrolyte system without cells is expected to be that of a series combination of a CPE (representing the interface at the electrode surface) and a resistor (representing the electrolyte solution) (Wegener *et al.*, 1999). The Bode diagram of such a system is a slope followed by a plateau, representing a transition from capacitive to resistive behavior as the frequency increases from low to high, and the

frequency-response of an ECIS-8W1E system with Hank's Balanced Salt Solution only shows this type of behavior, with the phase angle of impedance transitioning from capacitive to resistive between 100 Hz and 100 kHz (Rahman *et al.*, 2009). Similarly, Seebach *et al.* (2000) reported that between 10 Hz and 10 kHz, the impedance of the system is representative of the CPE, whereas between 10 kHz and 1 MHz the frequency-independent resistance of the bulk media determines the overall impedance.

The addition of the cell layer is expected to alter the interfacial impedance parameters of the CPE because the cells form close contact with the electrode (Rahman *et al.*, 2009). Wegener *et al.* (1999) demonstrated this type of result; they found that the values of A and n changed in the presence of cells, and they could not offer a complete explanation for the phenomenon, but they said that its continued investigation is ongoing. Because the cell layer covers the surface of the electrodes, but there is a space between the cells basal side and the electrode surface that is filled with culture media, the impedance of the cells should be in series with that of the electrode-electrolyte interface (Rahman *et al.*, 2009).

Attempts have been made at developing circuit models to represent the cell layer as a way of obviating the need to make assumptions regarding cell size and geometry as was necessary using the original methodology of Giaever and Keese (1991). Goda *et al.* (2005) modeled the cell layer as two parallel resistor/capacitor combinations in parallel with each other, one representing the cell membrane and the other one signifying the intercellular separation. This circuit was placed in series with the impedance of the electrode polarization and the bulk solution. A diagram of the electrical network they used to represent the cell layer is shown in Figure 2.

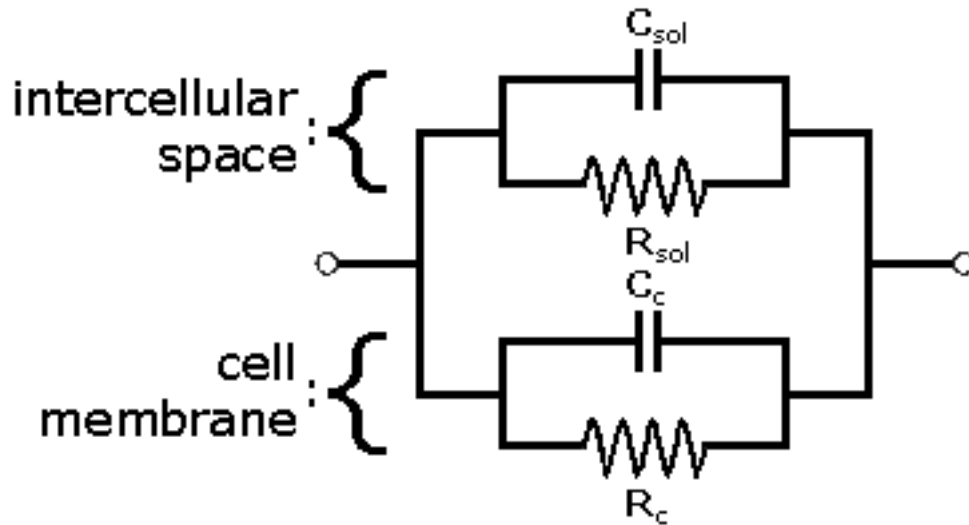


Figure 2. A schematic representation of the circuit model that Goda *et al.* (2005) used to represent the cell layer. R_{sol} is the resistance of the media between cells, and C_{sol} is the capacitance of the media between cells. R_c is the resistance of the cell membrane, and C_c is the capacitance of the cell membrane.

Simpler representations of the adherent cells that rely on a smaller number of individual circuit elements may provide a more accurate model of the electrochemical behavior that also better represents monolayer structure and physiology. AC impedance characteristics that resemble a parallel combination of a resistor and a capacitor have been reported for epithelial cells using a sinusoidal current clamp in a process called conductance scanning applied to paracellular and transcellular regions (Gitter *et al.*, 1997). The paracellular current route is between cells and through tight junctions, and the transcellular route is across the basal plasma membrane, traversing the cytoplasm and then out through the apical plasma membrane (Wegener *et al.*, 1999). An additional transcellular route across the lateral membrane, through the cytoplasm, and out through

the apical membrane can be neglected when cell types with leaky tight junctions such as fibroblasts and ECs are used (Lo *et al.*, 1995). A diagram of the electrical network that best modeled impedance data for the cell-electrolyte system in the study by Gitter *et al.* (1997) is shown below in Figure 3.

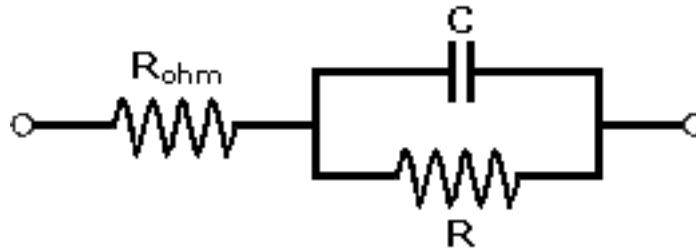


Figure 3. A schematic representation of the circuit model that best fit data from conductance scanning of unilayered epithelia (Gitter *et al.*, 1997). R_{ohm} represents the ohmic resistance of the media, and R and C represent the parameters of the parallel resistive and capacitive combination in the circuit, respectively.

In terms of modeling the cell membrane itself, it is important to consider that it is composed of a phospholipid bilayer that acts as an insulator except for ion channels that selectively conduct transcellular currents (Rahman *et al.*, 2009). It is appropriate to model the dielectric properties of the cell membrane as a parallel combination of a resistor and a capacitor (Wegener *et al.*, 1999). The specific membrane resistance of most barrier-forming cells is greater than $1000 \Omega\text{-cm}^2$ (Powell, 1981). Therefore, it can be expected that most resistive currents through EC monolayers will be conducted by the intercellular space and the tight junctions that link neighboring cells (Wegener *et al.*, 1999). The generally accepted value for cell membrane specific capacitance is $1 \mu\text{F}/\text{cm}^2$ (Rahman *et al.*, 2009). Because both the basal and apical cell membranes must be

considered to effectively be in series (lateral membranes in ECs can be neglected due to their small surface area), the specific capacitance of a monolayer of cells that are devoid of membrane folding is expected to be $0.5 \mu\text{F}/\text{cm}^2$ (Wegener *et al.*, 1999).

To summarize these findings, in the absence of a cellular monolayer, the impedance behavior of an electrochemical system can be described as a series connection of an ohmic resistor and a CPE (Seebach *et al.*, 2000). The experiments involving ECs that Wegener *et al.* (1999) performed using an impedance spectrum of 10 Hz – 2 MHz revealed that the electrical characteristics of the cell layer can be modeled by a parallel combination of a resistor and capacitor. Seebach *et al.* (2000) used the same circuit model to represent the impedance characteristics of ECs from 10 Hz – 1 MHz. A diagram of these two electrical networks is shown below in Figure 4.

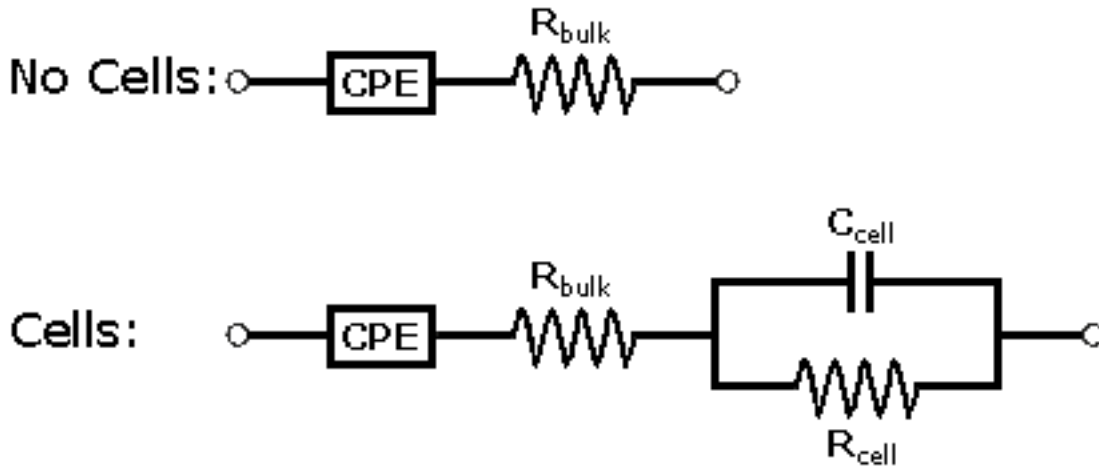


Figure 4. A schematic representation of the circuit models that Wegener *et al.* (1999) used. The CPE is the constant phase element, R_{bulk} is the resistance of the cell culture media, C_{cell} is the capacitance of the cell layer, and R_{cell} is the resistance of the cell layer.

The presence of the confluent cell monolayer significantly increases the impedance in the range from 1 kHz to 300 kHz (Seebach *et al.*, 2000). The resistance

and capacitance of the cell layer are overall quantities that include the contributions of different subcellular structures and therefore contain information pertaining to cell morphology (Wegener *et al.*, 1999). The spectral region above 1 MHz exhibits similar impedance characteristics in both the presence and absence of cells, implying that this section of data is attributable to the dielectric material that is used to insulate the unexposed portions of electrodes (Rahman *et al.*, 2009).

5. Specific Methods and Results

The original ECIS device of Giaever and Keese (1991) was fabricated by deposition of gold electrodes onto 60 mm polystyrene cell culture dishes using vacuum evaporation. More recent studies have incorporated fluid flow with impedance sensing. DePaola *et al.* (2001) constructed a flow chamber that was designed for use with the impedance sensing methodology of Giaever and Keese. It was composed of two parallel plates with a machined recess (1x25x60 mm) that defined the path of flow connected to a flow loop that incorporated a pump, a reservoir, and a damper. Inside of the flow chamber there were eight small electrodes (0.05 mm²) and one large electrode (1 cm²). The top plate was Teflon and it contained the inlet and outlet ports as well as a glass window that allowed sample visualization. The bottom plate with the machined recess contained the electrodes and contacts for connecting to the ECIS system, as well as a glass plate allowing for visualization. The chamber was sealed with a medical-grade silicon gasket that was held together by four screws to avoid fluid leakage.

In a similar fashion to that of Giaever and Keese, DePaola *et al.* (2001) used a 1 μ A AC signal at 4 kHz applied between the RE and CE. They monitored voltage changes between electrodes with a lock-in amplifier to measure impedance. The cellular

monolayer was modeled as a resistor and capacitor in series. They subjected bovine aortic endothelial cells (BAECs) that had been grown to confluence on the electrode surfaces to 10 dynes/cm^2 either for a single five-hour uninterrupted period of flow or for two consecutive thirty-minute periods separated by a two-hour interval with no flow. Results of the study demonstrated an increase in TER to 1.2 to 1.3 times the baseline value after fifteen minutes of flow followed by a decrease to 1.1 and 0.85 times baseline after thirty minutes and five hours of total flow time, respectively. Capacitance decreased following the onset of flow and then after slightly overshooting it decreased again for the remainder of the five-hour flow experiment (DePaola *et al.*, 2001). Capacitance changes were within 5% of their baseline value for the two thirty-minute flow periods separated by two hours without flow. The observed changes in endothelial impedance were found to be reversible with the cessation of flow. Their results indicated that changes in monolayer impedance could be correlated to known changes in EC structure and function in the presence of fluid flow by deducing morphological information from the measured impedance parameters.

The impedance sensing approach of Wegener *et al.* (1999) incorporated a device that had a distinct design but relied on similar fabrication techniques. Gold films were vacuum evaporated onto a standard microscope slide (76x26x1 mm) after a pre-evaporation step with chromium to improve adhesion. The upper part of a glass vial with a threaded top was cut-off and mounted onto the microscope slide with non-cytotoxic glue. A glass inlet that was integrated into the screw cap allowed for the addition of chemical compounds as well as the microscopic observation of the cells. Gold traces led to contacts where connections were made to a relay module that interfaced with a SI-

1260 continuous-wave impedance analyzer (Solatron Instruments, Farnborough, UK).

For impedance measurements, 20 mV amplitude voltages (peak-to-peak) were supplied as the excitation signal (to ensure an adequate signal-to-noise ratio), and impedance magnitude and phase-shift angle were determined as functions of frequency from 10 Hz to 2 MHz (Wegener *et al.*, 1999). The spectrometric data was fit with a non-linear least-squares algorithm to a circuit representing the electrochemical system, which was modeled as a parallel resistor and capacitor in series with a CPE and a resistor. Results were obtained for confluent monolayers of BAECs under control conditions and following stimulation with the synthetic beta-adrenoceptor agonist isoproterenol. They found that under control conditions, the specific resistance of the cells was $3.6 \pm 0.6 \Omega\text{-cm}^2$ and the specific capacitance was $0.6 \pm 0.1 \mu\text{F/cm}^2$ with a sample size of thirty. The results that the group obtained in the spectrometric mode demonstrated the ability to perform high-precision measurements of TER and capacitance of macrovascular ECs.

Another attempt at examining the effects of shear stress on impedance characteristics used ECs from porcine pulmonary trunks (PSECs). The system employed by Seebach *et al.* (2000) consisted of a cone-and-plate viscometer with integrated steel capillaries for media exchange. The bottom plate was a glass slide with vacuum evaporated gold electrodes that allowed for microscopic imaging and time-lapse video recording. The electrode arrangement comprised three small REs (0.05 cm^2) and one large CE (6 cm^2). An inert ring of polymer was adhered to the culture glass with non-cytotoxic glue to separate the measuring area within the shear space from the electrode contact region. Short cables were soldered to these peripheral gold areas outside of the ring, and connections were made to a SI-1260A impedance spectrometer (Solatron

Instruments, Farnborough, UK).

The impedance magnitude was determined as a function of frequency in a range from 10 Hz to 1 MHz (Seebach *et al.*, 2000). Spectrometric data was fit with a non-linear least-squares algorithm to the same circuit model that was used by Wegener *et al.* (1999). Shear stress was applied to the confluent ECs in twenty-four minute increments with alternating static periods of the same duration (Seebach *et al.*, 2000). These experiments were carried out such that five periods of shear stress exposure alternated with five quiescent periods, and shear stress magnitudes were either applied in increasing (2, 5, 10, 20, and then 50 dynes/cm²) or decreasing order (50, 20, 10, 5, and then 2 dynes/cm²). Also, one characteristic experiment was performed in which 10 dynes/cm² was applied continuously for ten hours.

It was observed that higher shear stress values caused a greater increase in TER after a two to four minute lag period (Seebach *et al.*, 2000). Shear stress levels of 5 dynes/cm² induced a 5% increase in TER within eighteen to twenty minutes, whereas levels of 50 dynes/cm² caused an approximately 15% increase in TER within ten minutes. Continuous shear stress of 10 dynes/cm² caused an initial increase of TER to roughly 7.5% above baseline followed by a downtrend that brought it below 85% of its original value until about the six-hour time-point when it began to recover slowly. The capacitance of the cell layer remained nearly constant throughout the duration of the experiment, and no gap formation in the PSECs was detected as determined by video observation. Overall, their results demonstrated a shear stress-dependent graduated regulation of TER.

Finally, a brief discussion of one other methodology for impedance sensing is

warranted. Rahman *et al.* (2009) developed a model to parameterize impedance data from 100 Hz to 10 MHz that accounted for polymer-coated electrode regions. They noted that commercially available two-port impedance analyzers have been increasingly used for cell-based impedimetric sensing, and the group itself made use of an Agilent 4294A precision impedance analyzer (Agilent Technologies, Santa Clara, CA). The output AC voltage signal was 10 mV in amplitude (peak-to-peak), which they mentioned satisfies the linearity requirement of impedance spectroscopy. They measured the impedance of ovarian cancer epithelial cells with an ECIS-8W1E device, and average parameters were calculated by normalizing resistances and capacitances to the area of the RE (0.049 mm²).

D. Orbital Flow

1. Motivation

Some of the advantages that arise when using an orbital shaker to drive fluid motion for shear stress response studies include the simplicity of culturing cells. While many systems fully enclose the cellular environment to prevent leaks and contamination, this approach restricts access to the sample during the course of the experiment (Young and Simmons, 2010). Most orbital shaker shear stress studies use conventional cell culture dishes (Dardik *et al.*, 2005), thus simplifying the process of seeding and maintaining cells. In addition, many labs have access to conventional orbital shakers.

An unsteady pulsatile type of fluid flow should be considered as opposed to steady continuous flow to model the *in vivo* hemodynamic environment more closely (Young and Simmons, 2010), and studies have demonstrated unique, time-dependent

adaptations to cell morphology under varying flow conditions involving steady, oscillatory, or pulsatile (with and without reversing patterns) fluid motion (Helmlinger *et al.*, 1991). The majority of studies use steady shear stress in a range from ten to forty dynes/cm² (Young and Simmons, 2010). However, the magnitude of shear stress in the venous system of humans ranges from one to six dynes/cm² (Chiu and Chien, 2011).

Some studies have used step-flow chambers to create disturbed flow patterns that mimic vascular regions where atherosclerotic lesions are known to originate, and to produce shear stress gradients where multiple flow conditions can be tested at the same time (Young and Simmons, 2010). Similarly, systems using an orbital shaker do not create a uniform shear stress level across the entire monolayer (Chiu and Chien, 2011). Although most permeability assays are done with cells under static conditions, it is desirable to perform such measurements while cells endure fluid flow given the known role of shear stress-regulated EC components affecting monolayer permeability (Young and Simmons, 2010).

2. Shear Stress

A shearing stress is defined as the force per unit area where the force vector lies in the plane of the area on which it is acting (Halliday *et al.*, 2001). The equation for shear stress is given below:

$$\tau = \frac{F}{A} \quad (7)$$

where τ is the shearing stress (in newtons/cm²), F is the force (in newtons) acting in the plane of area A (in cm²). Dardik *et al.* (2005) described an equation for the maximum

shear stress in an orbiting dish, but no derivation was given and the formula itself does not depend on the height of the fluid:

$$\tau_{max} = a\sqrt{\eta\rho(2\pi f)^3} \quad (8)$$

where τ_{max} is the maximum shear stress acting on the bottom of the orbiting cylinder (in newtons/cm²), a is the radius of orbit (in cm), η is the viscosity of the medium (in kg/m-s), ρ is its density (in kg/m³), and f is the frequency of the orbital rotation (in revolutions/second). The above equation for the maximum wall shear stress in an orbiting cylinder was referenced from Ley *et al.* (1989) and Kraiss *et al.* (2000). When Stokes' second problem is extended to the case of an orbiting infinite plate beneath a fluid layer of large height, an equation develops that is identical to Equation (8) (Chakraborty *et al.*, 2012). This analytical solution provides a single wall shear stress value, but the levels of shear that are generated in a dish on an orbital shaker are non-uniform.

Thomas *et al.* (2011) described the results of a computational fluid dynamics (CFD) simulation of flow in an orbiting dish at orbital speeds of 60, 90, 120, 150, 180, and 210 rpm assuming the same constant values that were used by Dardik *et al.* (2005). The density of the liquid in the dish was taken to be 997.3 kg/m³, with a viscosity of 0.00101 kg/m-s (Thomas *et al.*, 2011). Equation (8) has been commonly used to estimate shear stress values in orbiting dishes. It results in a single shear stress value for the entire dish, whereas the CFD simulation demonstrated significant variation in shear stress over the bottom surface of the dish. For example, at 120 rpm, shear stress levels are low towards the center of the dish, with a radial profile of increasing shear stress that peaks

near the edge of the dish.

Approximate peak wall shear stress values from the CFD simulation were listed as follows for radial locations of 4.25 mm, 12.8 mm, and 16.4 mm from the center of the dish (Thomas *et al.*, 2011). At 60 rpm, wall shear stress was nearly constant at 0.4 dynes/cm² at all three radial positions. At 150 rpm, the peak wall shear stress was approximately 6.5 dynes/cm² at 4.25 mm, 9.5 dynes/cm² at 12.8 mm, and 16 dynes/cm² at 16.4 mm. The author also produced a plot comparing the analytical solution to Stokes' second problem, the average shear stress value from the center of the dish, and the area average shear stress value based on all three radial positions examined (see Appendix for plot). At 60 and 90 rpm, the shear stress level from the center of the dish was nearly the same as the area average value, and the analytical value was roughly 1 dyne/cm² higher.

III. SYSTEM DESIGN

A. Specifications

1. Overall Dimensions

The device that was designed for conducting cell culture and impedance sensing was rectangular with a flat surface on which cells were grown. A circular well was placed on top of this surface to contain the cell culture. The circular geometry made it possible to create circumferential fluid flow within the culture space when the device was placed on an orbital shaker. Electrode patterns were defined such that certain areas were exposed to contact the cellular environment, and other regions were insulated to conduct electrical signals to contact pads where external connections were made.

The overall dimensions of the device that supported cell growth on its surface were 42 mm by 47 mm. The size of the well that was placed on top of this surface was 40 mm by 40 mm in outer dimensions, with a circular inner diameter of 35 mm. This circular well with a square outer profile was placed on the device surface using alignment marks to ensure that electrode patterns corresponded with precise radial locations within the well. This positioning resulted in a 1 mm margin between the outer edges of the well and the edges of the device itself on three sides. The length between the remaining outer side of the well and the corresponding edge of the device was 6 mm, which left enough room for the contact pads where external electrical connections were made.

2. Electrodes

Electrodes used for recording were arranged in three rows in the radial direction, each row being 120 degrees apart from the other two. These three rows of electrodes were assigned labels of A, B, and C. Rows A and C had six REs, which were spaced 2.5 mm apart from each other. Row B had seven REs, six of which were located at the same radial distances as the six in rows A and C, plus another RE at the center of the circular well. This design made it possible to do recordings from three REs at radial locations of 2.5 mm, 5.0 mm, 7.5 mm, 10.0 mm, 12.5 mm, and 15.0 mm, and one RE at the center of circulation. Each RE had a diameter of 200 μm , which equates to an area of 0.031 mm^2 .

A total of six CEs were patterned onto the device surface. Three of the six were circular in shape with a diameter of 5 mm (area of 19.63 mm^2), and they were placed directly between the three rows of REs with their centers located at a distance of 10.0 mm from the center of the circular well. These three circular CEs were numbered one through three for identification. The other three CEs were long and narrow, and they extended along the length of the rows of REs with portions cut out along their lengths where the REs could be placed in close proximity. These cutout parts of the long CEs contained semicircular regions where the REs were juxtaposed with a 200 μm radial distance separating them. These linear shaped CEs were labeled A, B, and C corresponding to the row of REs to which they were adjacent. CEs A and C had approximate areas of 13.35 mm^2 , and CE B had an approximate area of 15.65 mm^2 . This design ensured that no RE to CE area ratio was less than about 1:430. A diagram illustrating the device layout is shown in Figure 5.

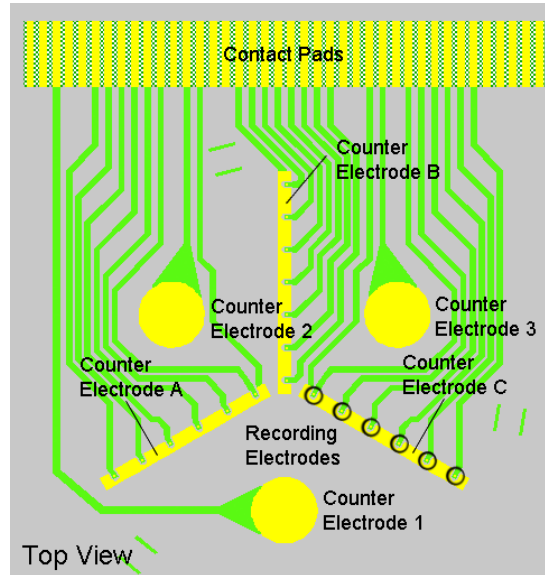


Figure 5. A schematic representation of the device, showing recording electrodes from rows A, B and C, as well as all six counter electrodes and the contact pads. Yellow regions show exposed metal surfaces, and green regions are insulated.

B. Benefits

1. Cell Culture

The employed design has many beneficial aspects that facilitate its use in performing routine cell culture while allowing permeability measurements by impedance sensing. Because it is a macroscale device with an open well design, seeding and maintenance of cells can be performed in a routine way that is essentially the same as the practice used in standard cell culture. The placement of a removable cover on top of the well enables media changes using sterile technique, which minimizes the risk of contamination. The dimensions of the culture area are the same as those for a standard 35 mm polystyrene cell culture dish, simplifying reagent volume and concentration calculations.

2. Permeability Measurement

Because this system uses impedance sensing to measure the TER of monolayers, there is no need for culturing cells on porous membranes or trans-well inserts that need to be moved to a different location from where the cultures are maintained. Permeability can be measured without the use of separate fluid compartments on the luminal and abluminal sides of the cells or the need to draw samples to measure permeating chemicals. Because the generation of fluid flow over the monolayer is possible while measuring permeability at the same time, the cells can be subjected to shear stress without the concern of precisely controlling the pressure in multiple fluid compartments.

3. Shear Stress Generation

When the device is placed on a conventional orbital shaker, fluid flow is induced within the well, and the shear stress generated on the bottom takes on a pulsatile waveform. This type of flow can be created without sophisticated equipment, and it is more physiologically relevant than a steady, constant flow in its ability to model the *in vivo* hemodynamic environment (Young and Simmons, 2010). Because the shear stress generated with an orbital shaker is non-uniform (Chiu and Chien, 2011), this system allows for the evaluation of multiple conditions at once, which increases experimental throughput. This advantage comes without the drawbacks associated with the use of microfluidic systems to test multiple conditions in parallel, such as concerns about the fidelity of comparing results from microchannels to those of established macroscale studies (Young and Simmons, 2010). Because impedance sensing is used to evaluate cellular responses to shear stress in real-time, the system does not rely solely on endpoint biochemical measures that assess ECs at the termination of a period of fluid flow.

IV. MATERIALS AND METHODS

A. Cell Culture Device

1. Fabrication

The help of a colleague at the University was employed for carrying-out the fabrication process used to create the cell culture device. This individual used microfabrication techniques including photolithographic patterning to define features on the substrate that supported the cell culture and enabled impedance sensing. First, a piece of borosilicate glass was cleaned in Nanostrip (a stabilized mixture of sulphuric acid and hydrogen peroxide). The glass is then prebaked at 150 degrees Celsius for at least 5 min and allowed to cool. Shipley 1827 photoresist (MicroChem, Newton, MA) is then spun onto the glass surface. The SUSS MicroTec Mask Aligner (SUSS Microtec, Garching, Germany) was used to align the device for photolithographic patterning of gold electrodes, which were deposited along with traces and contacts.

Chromium and gold, or nickel and gold, were sputtered onto the substrate surface. The metal layers were deposited using the Lesker PVD-75 Sputtering System (Kurt J. Lesker Company, East Sussux, UK), and a liftoff method was used. The entire surface was subsequently covered with a 1 μm -thick layer of silicon dioxide (to serve as an electrical insulator) by Oxford PECVD (plasma-enhanced chemical vapor deposition).

The device was then coated again with Shipley 1827 photoresist (MicroChem, Newton, MA) by spin coating, and the device was aligned with the SUSS MicroTec

Mask Aligner (SUSS Microtec, Garching, Germany). This photolithographic step was used to open up windows in the silicon dioxide layer for exposed electrode regions and contacts. The silicon dioxide was etched using a MARCH RIE (reactive ion etch) system (Nordson MARCH, Concord, CA).

2. Culture Well

A polymer was cast to make the 35 mm diameter well that defined the cell culture environment. First, a mold was constructed from a square glass base onto which pieces of plastic were glued. Rectangular pieces of plastic, each having a length of 40 mm, were glued to each other and the glass base. These pieces defined the square outer profile of the PDMS well. A piece of plastic tubing with a 35 mm diameter was placed on the glass in the center of the square and glued down from the inner side. The uncured polymer was poured into the space between the outer square and the inner cylinder.

Sylgard 184 (Dow Corning, Midland, MI) was used as the PDMS base and curing agent. The uncured base and curing agent were mixed in a 10:1 ratio, poured into the mold, and heat-cured at approximately 100 degrees Fahrenheit for six hours to produce the well with a square outer profile and a cylindrical inner shape where the cell culture was to be maintained. The PDMS well was then removed from the mold by cutting away the glued plastic, releasing the cured polymer. It was placed on top of the substrate facedown on the side that had been cured on glass to form a watertight seal around the edges of the device.

A removable cover for the well was cast from PDMS by molding a piece of clay into a rectangle that was slightly wider than 40 mm by 40 mm, gluing it onto the bottom of a plastic dish, and using it as a negative. Uncured PDMS pre-polymer was poured

onto the clay negative in the dish, to a height slightly above the top of the mold. After the PDMS was heat-cured for six hours at 100 degrees Fahrenheit, a square shaped cut in the PDMS that left a margin of several millimeters from the edge of the clay in the center of the plastic dish defined the outer edge of the cover. This cut allowed the center section of PDMS to be freed from the plastic dish, and then the clay mold was taken out of the cutout polymer, revealing the defined cover shape. This process resulted in a square shaped cover that fit onto the outer edges of the device's circular well, and served as a mechanism to prevent contamination of the cell culture, while allowing easy access for media exchanges. An image of the device with the completed PDMS well on top is shown below in Figure 6.

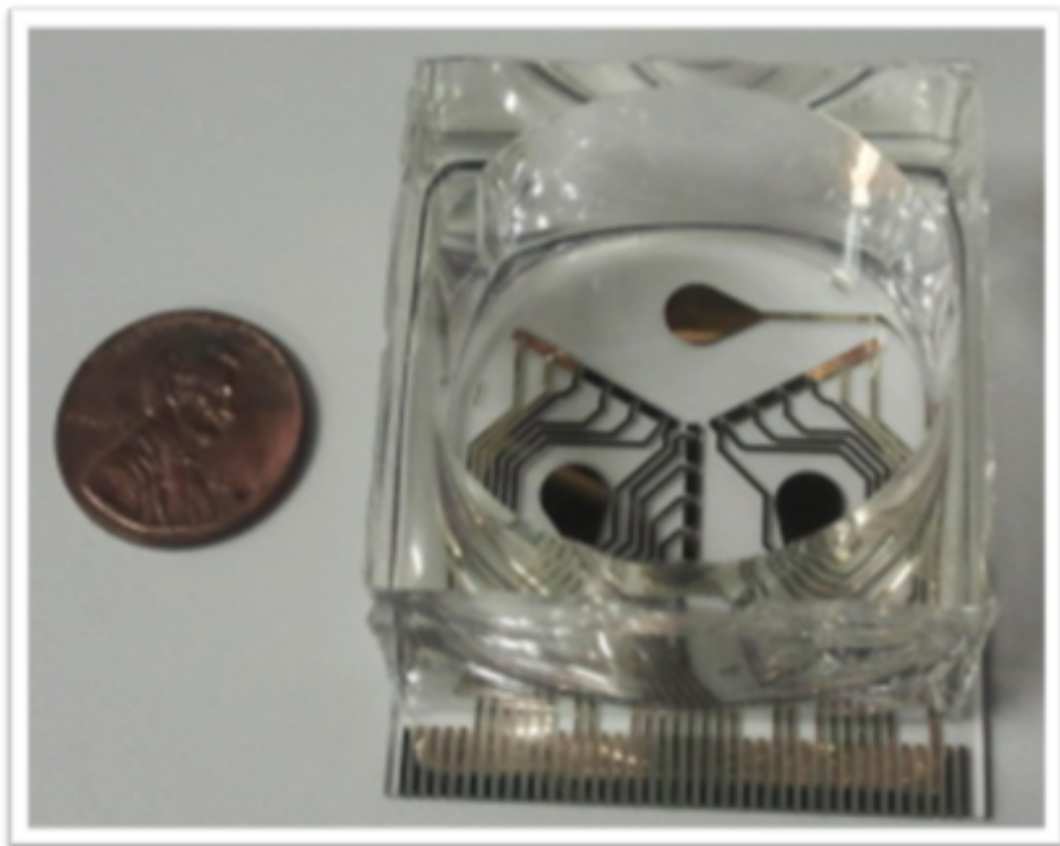


Figure 6. A photograph of the device with the PDMS well on its surface.

B. Attachment and Spreading

1. Cell Culture

The first experiment that was performed involved seeding cells on the device and monitoring attachment and spreading as a validation measure to ensure that the impedance of the cell layer went up as the percent coverage of cells on the device surface increased. The device was first sterilized by submersion in 70% ethanol inside a piece of autoclaved glass, followed by UV-sterilization overnight. The device surface was then coated with 1 ml of Attachment Factor (Life Technologies, Carlsbad, CA), which is a sterile solution containing 0.1% gelatin, and left at room temperature for three hours.

HUVECs that had been grown to confluence in a T-25 cell culture flask (Corning, Corning, NY) were dissociated with 0.25% trypsin and seeded onto the device at passage six at 11.3% surface coverage based on a 125,000 cells/cm² confluence level. The cells were cultured in Medium 200 (Life Technologies, Carlsbad, CA) liquid medium, which is intended for the culture of human large vessel ECs. Low Serum Growth Supplement (Life Technologies, Carlsbad, CA) was added to the media to produce final concentrations of 2% volume/volume fetal bovine serum, 1 µg/ml hydrocortisone, 10 ng/ml human epidermal growth factor, 3 ng/ml basic fibroblast growth factor, and 10 µg/ml heparin. The media was also supplemented with Penicillin-Streptomycin-Glutamine (Life Technologies, Carlsbad, CA) to final concentrations of 100 units/ml penicillin, 100 µg/ml streptomycin, and 0.292 mg/ml L-glutamine to support cell growth and prevent bacterial contamination.

2. Experimental Procedure

Cells were allowed to seed for twenty-four hours in a standard cell culture

incubator that maintained conditions at 5% CO₂ and 95% air at 37 degrees Celsius and 85% relative humidity. On every day subsequent to Day 0, up to and including Day 9, cells were removed from the incubator, the culture media was changed, and impedance data was recorded for thirty minutes under static fluid conditions. The volume of cell culture media used in all experiments was 2.0 mL. Following the collection of impedance data, the device was placed on an inverted microscope under bright-field illumination and the percentage of the device surface area covered by cells was estimated by visual inspection. The cells were then returned to the incubator until the impedance recordings on the subsequent day.

C. Shear Stress Response

1. Cell Culture

The device was sterilized and prepared with Attachment Factor (Life Technologies, Carlsbad, CA) in the same manner as for the attachment and spreading experiment. After growing to confluence in a T-75 cell culture flask (Corning, Corning, NY), HUVECs were dissociated with 0.25% trypsin and seeded on the device at passage six at 80% surface coverage based on a 125,000 cells/cm² confluence level. The media and supplements used to maintain cells were the same as those used for the attachment and spreading experiment.

2. Experimental Procedure

Cells were seeded, attached, and grown to confluence over forty-eight hours in a standard cell culture incubator. Following this period, the ECs had reached confluent coverage of the device surface, and the culture was moved to an environmental chamber

for the purpose of conducting the shear stress exposure and impedance sensing experiment. The environmental chamber maintained ambient conditions of 5% CO₂ and 95% air at 37 degrees Celsius and 85% relative humidity. Once the device had been placed inside the environmental chamber and allowed to equilibrate for fifteen minutes, a baseline recording of impedance data was taken under static fluid conditions. The cell media was changed preceding this equilibration period to control for ions consumed and excreted by the ECs. The volume of cell media used during the experiment was 2.0 mL, which corresponds to a fluid height of 2.0 mm in the circular well. This step was necessary because it had been observed that dramatic changes in the conductivity of the media occur following long periods of time (twenty-four to forty-eight hours) without cell media exchange, which can greatly reduce measured impedance. Therefore, in order to ensure that impedance measurements were properly controlled, the media in the circular well of the device was always changed before impedance sensing.

A Barnstead/Lab-Line Lab Rotator 1314 orbital shaker (Marshall Scientific, Brentwood, NH) with an orbital diameter of 0.95 mm that had been placed inside of the environmental chamber before the experiment was turned on and set to a rotation speed of 75 rpm, with the cell culture on top. The impedance of the device and the contained monolayer was analyzed for each sampled RE/CE combination every fifteen minutes for a two-hour period, after which the cell culture was removed from the environmental chamber and placed on an inverted microscope under bright-field illumination. Microscopic images were captured using a 10X objective lens to observe and document cell morphology after shear stress exposure.

An Agilent 4294A Precision Impedance Analyzer (Agilent Technologies, Santa Clara, CA) with an Agilent 42941A impedance probe (Agilent Technologies, Santa Clara, CA) connected to a pair of leads, completed circuits through the PCB and the device for the measurement of experimental data. A photograph illustrating the setup in its entirety is shown in Figure 8. The device with a cell culture contained in its circular well is seated in the card socket that was soldered to the PCB. The ribbon cable connecting to the outside of the chamber is attached to the PCB for data acquisition.

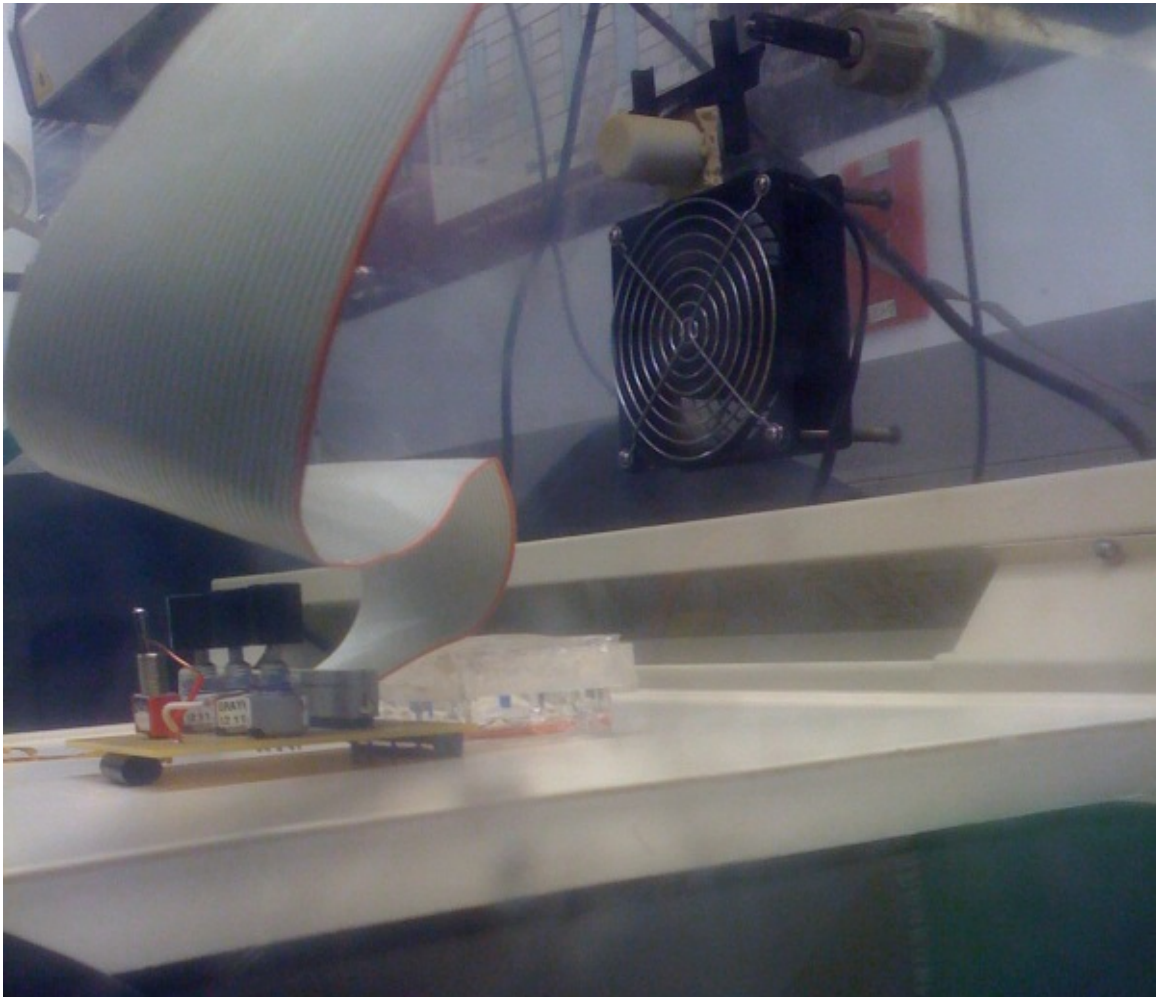


Figure 8. The device used for impedance sensing inside the environmental chamber.

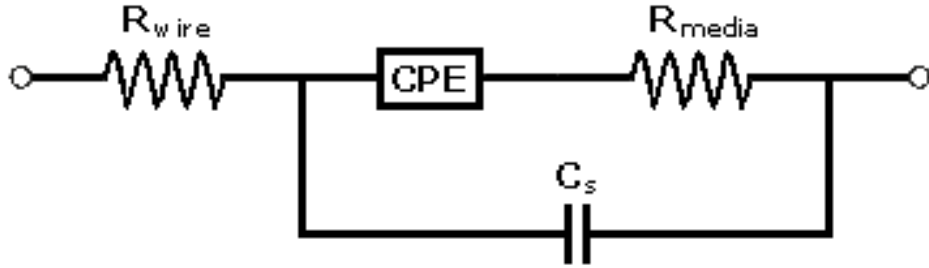
2. Settings

The impedance analyzer was calibrated with both open and short connections. In all of the experimental cases, AC voltages with a 10 mV root-mean-square value were supplied between electrodes. The impedance of the device with only media and attachment factor was compared to that of the device with media, attachment factor, and cells. The magnitude and phase of impedance were recorded over the entire frequency range of the analyzer (40 Hz to 110 MHz). Five frequency sweeps were averaged to produce the impedance dataset for the measurement of any given RE/CE combination.

3. Circuit Model

Every circuit component that was used in the electrical networks that modeled the electrochemical systems represented part of the physical setup. A resistor modeled the connections to the impedance analyzer and the gold electrodes. This resistor was in series with a circuit representing the electrochemical system. The electrode-electrolyte interface, the cell layer when present, and the media plus attachment factor, comprised a series portion of the circuit defining the system, which was placed in parallel with the part of the circuit representing insulated portions of the substrate. The electrode-electrolyte interface was modeled by a CPE in series with the cell layer when present, which was modeled by a parallel resistor and capacitor combination, both of which were in series with a resistor, which represented the bulk media and the attachment factor. A capacitor modeled currents through dielectric portions of the substrate that prefer this path at high frequencies. A diagram of the circuit models used for the system with and without cells is shown below in Figure 9.

No Cells:



Cells:

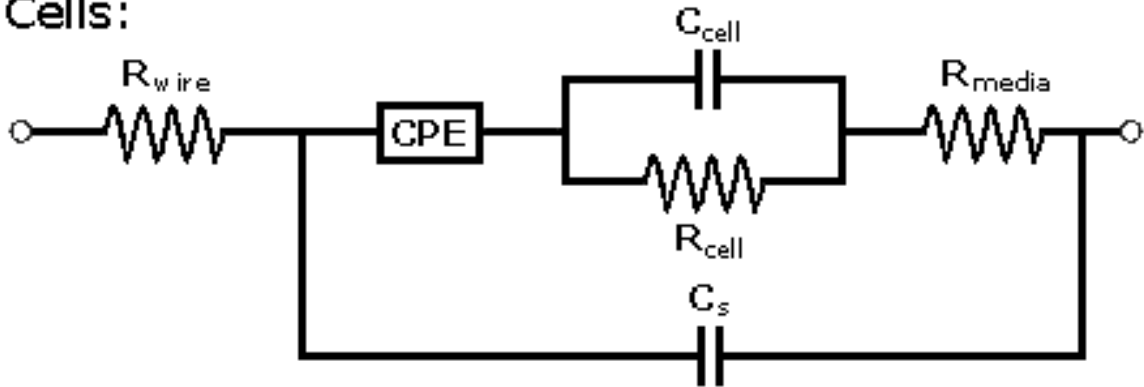


Figure 9. A schematic of the electric circuits fit to impedance data, both with and without cells. R_{wire} represents the leads, contacts, and metal traces. The CPE models the electrode surface electric double-layer. It is in series with the parallel combination of R_{cell} and C_{cell} , representing the cell layer resistance and capacitance, respectively. With or without cells, R_{media} , which is the bulk media and attachment factor resistance, is in series with the CPE, and when ECs are present, with the parallel RC cell layer. C_s is the coating capacitance through dielectric insulators of metal conductors in the substrate.

4. Fit Parameters

All impedance measurements were plotted with ZView (Scribner Associates, Southern Pines, NC) impedance analysis software. Log-log plots of impedance versus frequency were created, and data was fit to the circuit models in Figure 9 in the frequency

range from 40 Hz to 9 MHz. The empirical data was fit by least-squares regression to the representative circuit model. During circuit fitting for the recording with media and attachment factor only (no cells), the values of all four of the circuit components were set as free. From the results of the best-fit model without cells, the values of R_{wire} , R_{media} , and C_s were applied as fixed values for the circuit fits from experiments with cells, while the values of the CPE, R_{cell} , and C_{cell} were left free to determine alterations in the electric double-layer, the cell layer resistance, and the cell layer capacitance, respectively. This procedure was used because the resistance of the wires and connections was not expected to change. The resistance of the bulk media should not change either, because it is always replaced with fresh media at the beginning of the experiment. Additionally, the capacitance of the substrate itself can be assumed to remain constant, whether cells are present or not. The wire resistance, media resistance, and substrate capacitance, were fixed so that they did not change during circuit fitting of the results with cells. Instead, only the parameters of the CPE, the cell layer resistance, and the cell layer capacitance were allowed to vary, in order to fit the impedance data of the device with cells.

5. Electrode Configurations

In the attachment and spreading experiment, five REs were used for impedance sensing in combination with two CEs each, for a total of ten RE/CE configurations. The impedance of each RE was measured through a connection with either its adjacent linear CE or one of the neighboring circular CEs. Cells spread from their original attachment seeding density on Day 0, to reach 95% surface coverage, as evidenced by microscopic visual estimation on Day 9. These recordings were done under static fluid conditions.

During the shear stress response study, impedance was analyzed from individual

REs at radii of 5.0 mm, 7.5 mm, 10.0 mm, and 12.5 mm, plus two REs at a 15.0 mm radial distance from the center of the well. All data acquired with cells under hydrodynamic wall shear stress was done with confluent monolayers. The long, thin CEs within 200 μm of each sampled RE were used in conducting the bipolar impedance sensing of ECs under dynamic shear stress. Every RE was paired with its row's linear CE during the fluid flow experiments.

V. RESULTS

A. Attachment and Spreading

1. Circuit of Best Fit

The values of the best fit of the empirical data to the two circuit models yielded values for cell layer resistance and capacitance, as well as the CPE when cells were present, and values for wire resistance, media resistance, and substrate capacitance from measurements with just media, that were held as fixed constants in these circuit fits. It was found that cell layer resistance increases, and cell layer capacitance decreases, as cell area coverage of the device increases. Cell layer resistance (the same as TER) increased roughly two- to four-fold from the day after seeding (Day 1) to the day it peaked (either Day 8 or 9 for all REs except one that peaked on Day 3). Meanwhile, measured capacitance decreases as cell spreading occurs, often falling by nearly two orders of magnitude over the same time period. Both of these effects serve to increase the measured impedance of the cell layer circuit component parameters, as electrical impedance is directly proportional to resistance, and inversely proportional to capacitance, as described in Equation (5).

All of the circuit component values for best fits from three time-points for each RE and CE combination measured during the attachment and spreading experiment are shown in Tables 1 – 5. Earlier time-points with low cell coverage often did not fit the cell layer circuit model as characterized with low error percentages for fit circuit

components. However, later time-points, i.e. when the cell layer was more confluent, more accurately fit circuit components. Error percentages are calculated by changing best-fit circuit component parameters until an equally good fit is produced using a higher value and a lower value. The difference between these higher and lower values and the best-fit circuit element is taken and divided by the best-fit value, yielding the percentage error.

Table 1

Circuit Parameters for a Recording Electrode of Row A-5.0mm from the Center with Counter Electrodes A and 1

Recording Electrode A-5.0mm		Counter Electrode A													
R-cell		C-Cell		R-wire		CPE-A		CPE-n		R-media		C-substrate			
	Value	% Error	Value	% Error	Value	% Error	Value	% Error	Value	% Error	Value	% Error	Value	% Error	
Media Only					209.6 Ω	1.65%	4.014E-09 $\Omega^{-1}s^n$	0.92%	0.93	0.10%	1731 Ω	0.78%	4.987E-04 pF	0.74%	
Day 1	15%	2756 Ω	19.3%	1.464E-02 pF	12.9%	209.6 Ω	N/A	5.533E-09 $\Omega^{-1}s^n$	4.0%	0.96	0.6%	1731 Ω	N/A	4.987E-04 pF	N/A
Day 2	30%	8309 Ω	8.1%	5.751E-03 pF	5.6%	209.6 Ω	N/A	6.233E-09 $\Omega^{-1}s^n$	3.7%	0.94	0.6%	1731 Ω	N/A	4.987E-04 pF	N/A
Day 8	90%	10279 Ω	2.5%	1.161E-03 pF	2.0%	209.6 Ω	N/A	6.673E-09 $\Omega^{-1}s^n$	2.6%	0.92	0.4%	1731 Ω	N/A	4.987E-04 pF	N/A

Recording Electrode A-5.0mm		Counter Electrode 1													
R-cell		C-Cell		R-wire		CPE-A		CPE-n		R-media		C-substrate			
	Value	% Error	Value	% Error	Value	% Error	Value	% Error	Value	% Error	Value	% Error	Value	% Error	
Media Only					390.6 Ω	1.15%	3.994E-09 $\Omega^{-1}s^n$	0.97%	0.94	0.11%	1798 Ω	0.85%	4.851E-04 pF	0.90%	
Day 1	15%	3407 Ω	17.6%	1.227E-02 pF	11.6%	390.6 Ω	N/A	5.343E-09 $\Omega^{-1}s^n$	4.4%	0.97	0.6%	1798 Ω	N/A	4.851E-04 pF	N/A
Day 2	30%	8095 Ω	9.8%	5.858E-03 pF	6.7%	390.6 Ω	N/A	6.045E-09 $\Omega^{-1}s^n$	4.5%	0.95	0.7%	1798 Ω	N/A	4.851E-04 pF	N/A
Day 8	90%	11853 Ω	2.7%	9.534E-04 pF	2.4%	390.6 Ω	N/A	6.467E-09 $\Omega^{-1}s^n$	3.2%	0.93	0.5%	1798 Ω	N/A	4.851E-04 pF	N/A

Table 2

Circuit Parameters for a Recording Electrode of Row A-7.5mm from the Center with Counter Electrodes A and 1

Recording Electrode A-7.5mm			Counter Electrode A															
	R-cell		C-Cell		R-wire		CPE-A			CPE-n		R-media		C-substrate				
	Value	% Error	Value	% Error	Value	% Error	Value	% Error	% Error	Value	% Error	Value	% Error	Value	% Error			
Media Only					206.4 Ω	1.94%	3.710E-09	$\Omega^{-1}s^n$	0.99%	0.94	0.11%	1883 Ω	0.77%	4.561E-04	pF	0.78%		
Day 1	15%	4517 Ω	13.9%	1.240E-02	pF	9.6%	206.4 Ω	N/A	4.873E-09	$\Omega^{-1}s^n$	3.2%	0.96	0.5%	1883 Ω	N/A	4.561E-04	pF	N/A
Day 3	45%	8154 Ω	3.5%	3.628E-03	pF	2.4%	206.4 Ω	N/A	5.494E-09	$\Omega^{-1}s^n$	1.9%	0.94	0.3%	1883 Ω	N/A	4.561E-04	pF	N/A
Day 8	90%	9206 Ω	4.0%	9.475E-04	pF	3.5%	206.4 Ω	N/A	6.423E-09	$\Omega^{-1}s^n$	3.9%	0.91	0.6%	1883 Ω	N/A	4.561E-04	pF	N/A

Recording Electrode A-7.5mm			Counter Electrode 1															
	R-cell		C-Cell		R-wire		CPE-A			CPE-n		R-media		C-substrate				
	Value	% Error	Value	% Error	Value	% Error	Value	% Error	% Error	Value	% Error	Value	% Error	Value	% Error			
Media Only					384.5 Ω	1.34%	3.767E-09	$\Omega^{-1}s^n$	1.04%	0.94	0.12%	1933 Ω	0.84%	4.387E-04	pF	0.95%		
Day 1	15%	4710 Ω	10.6%	1.154E-02	pF	10.6%	384.5 Ω	N/A	4.743E-09	$\Omega^{-1}s^n$	3.9%	0.97	0.6%	1933 Ω	N/A	4.387E-04	pF	N/A
Day 3	45%	8641 Ω	4.9%	3.518E-03	pF	3.3%	384.5 Ω	N/A	5.368E-09	$\Omega^{-1}s^n$	2.8%	0.94	0.4%	1933 Ω	N/A	4.387E-04	pF	N/A
Day 8	90%	10244 Ω	3.7%	7.659E-04	pF	3.5%	384.5 Ω	N/A	6.321E-09	$\Omega^{-1}s^n$	4.0%	0.91	0.6%	1933 Ω	N/A	4.387E-04	pF	N/A

Table 3

Circuit Parameters for a Recording Electrode of Row A-10.0mm from the Center with Counter Electrodes A and 1

		Recording Electrode A-10.0mm				Counter Electrode A									
		R-cell		C-Cell		R-wire		CPE-A		CPE-n		R-media		C-substrate	
		Value	% Error	Value	% Error	Value	% Error	Value	% Error	Value	% Error	Value	% Error	Value	% Error
Media Only						220.5 Ω	2.43%	4.278E-09 $\Omega^{-1}s^n$	0.94%	0.91	0.11%	2024 Ω	0.76%	3.413E-04 pF	0.88%
Day 1	15%	4371 Ω	33.4%	1.447E-02 pF	22.6%	220.5 Ω	N/A	4.592E-09 $\Omega^{-1}s^n$	7.3%	0.98	1.1%	2024 Ω	N/A	3.413E-04 pF	N/A
Day 3	45%	6826 Ω	15.6%	6.033E-03 pF	10.5%	220.5 Ω	N/A	5.071E-09 $\Omega^{-1}s^n$	6.1%	0.95	0.9%	2024 Ω	N/A	3.413E-04 pF	N/A
Day 9	95%	8780 Ω	4.4%	1.257E-03 pF	3.4%	220.5 Ω	N/A	6.5E-09 $\Omega^{-1}s^n$	3.8%	0.91	0.6%	2024 Ω	N/A	3.413E-04 pF	N/A

		Recording Electrode A-10.0mm				Counter Electrode 1									
		R-cell		C-Cell		R-wire		CPE-A		CPE-n		R-media		C-substrate	
		Value	% Error	Value	% Error	Value	% Error	Value	% Error	Value	% Error	Value	% Error	Value	% Error
Media Only						395.5 Ω	1.40%	4.314E-09 $\Omega^{-1}s^n$	0.81%	0.91	0.09%	2061 Ω	0.97%	3.256E-04 pF	0.87%
Day 1	15%	4359 Ω	35.5%	1.510E-02 pF	24.1%	395.5 Ω	N/A	4.567E-09 $\Omega^{-1}s^n$	7.6%	0.98	1.1%	2061 Ω	N/A	3.256E-04 pF	N/A
Day 3	45%	6785 Ω	16.3%	6.172E-03 pF	10.9%	395.5 Ω	N/A	5.049E-09 $\Omega^{-1}s^n$	6.3%	0.95	0.9%	2061 Ω	N/A	3.256E-04 pF	N/A
Day 9	95%	9123 Ω	5.1%	1.200E-03 pF	4.0%	395.5 Ω	N/A	6.664E-09 $\Omega^{-1}s^n$	4.5%	0.90	0.7%	2061 Ω	N/A	3.256E-04 pF	N/A

Table 4

Circuit Parameters for a Recording Electrode of Row B-2.5mm from the Center with Counter Electrodes B and 2

Recording Electrode B-2.5mm			Counter Electrode B				CPE-n		R-media		C-substrate				
	R-cell		C-Cell		R-wire		CPE-A		CPE-n		R-media		C-substrate		
	Value	% Error	Value	% Error	Value	% Error	Value	% Error	Value	% Error	Value	% Error	Value	% Error	% Error
Media Only					152.7 Ω	3.56%	3.409E-09 $\Omega^{-1}s^n$	1.18%	0.95	0.13%	1921 Ω	0.81%	3.904E-04 pF	0.96%	
Day 1 15%	5318 Ω	2.9%	2.714E-03 pF	2.0%	152.7 Ω	N/A	5.624E-09 $\Omega^{-1}s^n$	1.9%	0.95	0.3%	1921 Ω	N/A	3.904E-04 pF	N/A	
Day 2 30%	9041 Ω	2.9%	3.566E-04 pF	4.1%	152.7 Ω	N/A	8.34E-09 $\Omega^{-1}s^n$	3.7%	0.88	0.5%	1921 Ω	N/A	3.904E-04 pF	N/A	
Day 3 45%	22047 Ω	1.6%	1.377E-04 pF	3.7%	152.7 Ω	N/A	6.883E-09 $\Omega^{-1}s^n$	3.3%	0.91	0.5%	1921 Ω	N/A	3.904E-04 pF	N/A	

Recording Electrode B-2.5mm			Counter Electrode 2				CPE-n		R-media		C-substrate				
	R-cell		C-Cell		R-wire		CPE-A		CPE-n		R-media		C-substrate		
	Value	% Error	Value	% Error	Value	% Error	Value	% Error	Value	% Error	Value	% Error	Value	% Error	% Error
Media Only					310.9 Ω	1.45%	3.447E-09 $\Omega^{-1}s^n$	0.81%	0.95	0.09%	1937 Ω	0.57%	3.695E-04 pF	0.76%	
Day 1 15%	5870 Ω	3.6%	2.381E-03 pF	2.6%	310.9 Ω	N/A	5.809E-09 $\Omega^{-1}s^n$	2.6%	0.94	0.4%	1937 Ω	N/A	3.695E-04 pF	N/A	
Day 2 30%	8776 Ω	2.9%	4.259E-04 pF	3.8%	310.9 Ω	N/A	7.994E-09 $\Omega^{-1}s^n$	3.6%	0.89	0.5%	1937 Ω	N/A	3.695E-04 pF	N/A	
Day 3 45%	20489 Ω	1.7%	1.665E-04 pF	3.5%	310.9 Ω	N/A	6.97E-09 $\Omega^{-1}s^n$	3.4%	0.91	0.5%	1937 Ω	N/A	3.695E-04 pF	N/A	

Table 5

Circuit Parameters for a Recording Electrode of Row B-7.5mm from the Center with Counter Electrodes B and 2

Recording Electrode B-7.5mm			Counter Electrode			B									
R-cell		C-Cell		R-wire		CPE-A		CPE-n		R-media		C-substrate			
Value	% Error	Value	% Error	Value	% Error	Value	% Error	Value	% Error	Value	% Error	Value	% Error		
Media Only				161.7 Ω	3.56%	3.385E-09 $\Omega^{-1}s^n$	0.88%	0.95	0.10%	1892 Ω	0.56%	3.021E-04 pF	0.91%		
Day 1	15%	7974 Ω	31.4%	1.583E-02 pF	22.9%	161.7 Ω	N/A	3.369E-09 $\Omega^{-1}s^n$	5.6%	0.99	0.8%	1892 Ω	N/A	3.021E-04 pF	N/A
Day 4	60%	9375 Ω	5.0%	2.911E-03 pF	3.6%	161.7 Ω	N/A	5.56E-09 $\Omega^{-1}s^n$	2.4%	0.90	0.4%	1892 Ω	N/A	3.021E-04 pF	N/A
Day 9	95%	11883 Ω	1.3%	1.680E-04 pF	2.6%	161.7 Ω	N/A	4.804E-09 $\Omega^{-1}s^n$	2.2%	0.93	0.3%	1892 Ω	N/A	3.021E-04 pF	N/A

Recording Electrode B-7.5mm			Counter Electrode			2									
R-cell		C-Cell		R-wire		CPE-A		CPE-n		R-media		C-substrate			
Value	% Error	Value	% Error	Value	% Error	Value	% Error	Value	% Error	Value	% Error	Value	% Error		
Media Only				318.9 Ω	2.19%	3.499E-09 $\Omega^{-1}s^n$	0.90%	0.95	0.10%	1919 Ω	0.59%	2.851E-04 pF	1.06%		
Day 1	15%	6766 Ω	32.0%	1.551E-02 pF	22.8%	318.9 Ω	N/A	3.349E-09 $\Omega^{-1}s^n$	5.8%	0.99	0.9%	1919 Ω	N/A	2.851E-04 pF	N/A
Day 4	60%	9490 Ω	6.0%	2.754E-03 pF	4.3%	318.9 Ω	N/A	5.619E-09 $\Omega^{-1}s^n$	3.0%	0.90	0.5%	1919 Ω	N/A	2.851E-04 pF	N/A
Day 9	95%	10979 Ω	1.3%	1.830E-04 pF	2.5%	318.9 Ω	N/A	4.781E-09 $\Omega^{-1}s^n$	2.2%	0.93	0.3%	1919 Ω	N/A	2.851E-04 pF	N/A

2. Average Specific Values

Cell layer specific resistance was defined as the TER measurement normalized to the area of the RE (0.031 mm²). This quantity represents the specific resistance value for the cell layer, which is a measure of resistance of the cell layer times the area of electrode. These values were computed as an average of the two separate measures of TER from one RE, with either of its two corresponding CEs on the day of its peak value, normalized to the area of the RE. The peak in cell layer resistance was reached on Day 8 or 9 for every RE, except for one out of the five electrodes, which experienced its highest TER on Day 3. An overall average specific resistance was computed for all five REs. Values for specific TER are reported in $\Omega\text{-cm}^2$ in Table 6 below. Percent error is the average derived from the best fit circuit for the cell layer resistances used to calculate mean specific TER, and overall average percent error is from all five of the REs. The results show an overall average specific TER of 3.87 $\Omega\text{-cm}^2$ with a standard deviation of 1.39 $\Omega\text{-cm}^2$ (n = 5). The range of specific TER among the sampled electrodes is roughly $\sim 3 - 7 \Omega\text{-cm}^2$.

Table 6

TER Values Normalized to RE Area to Produce Specific Cell Layer Resistance

Recording Electrode	Day	Average Specific TER	Percent Error
A-5.0mm	Day 8 90%	3.43 $\Omega\text{-cm}^2$	2.60%
A-7.5mm	Day 8 90%	3.01 $\Omega\text{-cm}^2$	3.85%
A-10.0mm	Day 9 95%	2.77 $\Omega\text{-cm}^2$	4.75%
B-2.5mm	Day 3 45%	6.59 $\Omega\text{-cm}^2$	1.65%
B-7.5mm	Day 9 95%	3.54 $\Omega\text{-cm}^2$	1.30%
Overall Average		3.87 $\Omega\text{-cm}^2$	2.83%

3. Constant Phase Element

In addition to surveying changes in TER, observations of the behavior of the CPE in the presence and absence of cells were done as well. The results showed a drop in the impedance of the CPE when cells were present in the device well, versus when it contained only media. This phenomenon shows an alteration in the CPE, which models the electrode-electrolyte interfacial electric double layer, when cells were present, in contrast to when they were absent. An overall average of the A , and n parameters from Equation (6) was calculated from all ten RE/CE configurations. These values were then used to find the absolute magnitude of impedance of the CPE from the circuit fit at each of the three time-points with cells reported in Tables 1 – 5, as well as with only media. The impedance magnitude of the CPE values averaged from all REs was lower at each time-point with cells compared to conditions with just media and attachment factor.

Table 7

Constant Phase Element Parameters at Different Averaged Culture Time-Points

	Condition Average	CPE-A	CPE-n	Impedance Magnitude at 100 Hz	Impedance Magnitude at 1000 Hz
no cells	Overall Average of Media Only	3.782E-09 $\Omega^{-1}s^n$	0.94	619,426 Ω	71,120 Ω
	Overall Average of Time-point 1	4.780E-09 $\Omega^{-1}s^n$	0.97	403,959 Ω	43,285 Ω
cells	Overall Average of Time-point 2	6.077E-09 $\Omega^{-1}s^n$	0.92	438,516 Ω	52,721 Ω
	Overall Average of Time-point 3	6.249E-09 $\Omega^{-1}s^n$	0.91	454,827 Ω	55,956 Ω

4. Bode Plot

An example log-log plot of impedance magnitude as a function of frequency with data from the RE of Row A that was 5.0 mm from the center of the well and CE A is given in Figure 8. In this figure, data is shown over the frequency range from 1 kHz to 1

MHz. The black plot, illustrating the device with media and attachment factor only, shows a greater magnitude of impedance versus the device on Day 8 of cell growth (shown in blue) at low frequencies (slightly greater than 1 kHz). This behavior is representative of the altered CPE characteristics with cells versus without cells shown in Table 7. At higher frequencies within the spectrum shown in Figure 10, from roughly 3 kHz to 200 kHz, the electrode has higher impedance on Day 8 versus when it has just media and attachment factor.

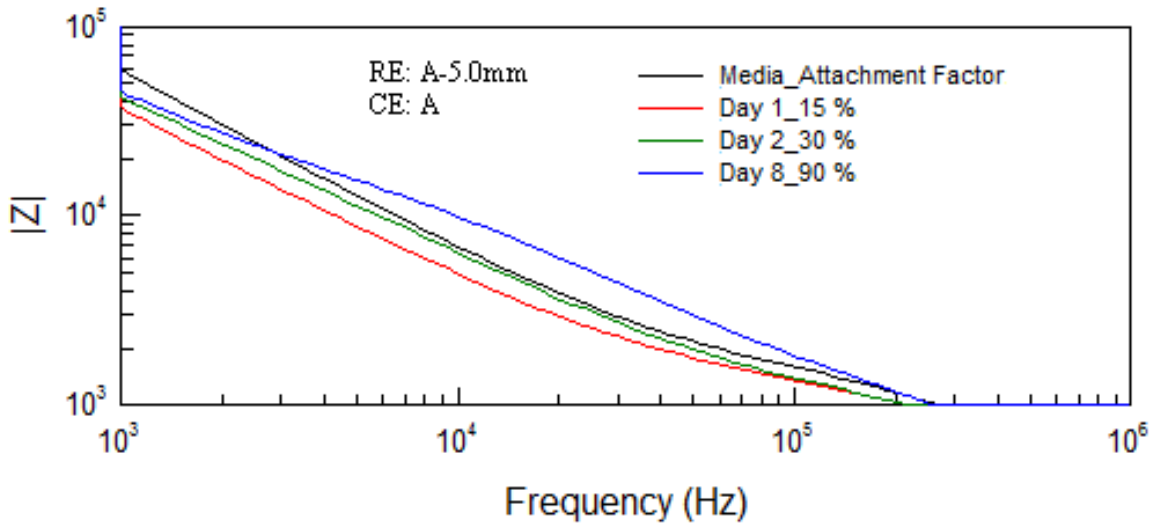


Figure 10. Impedance Bode plot from the RE of row A at a 5.0 mm radius and CE A, with just media and attachment factor (black), and on Day 1 (red), Day 2 (green), and Day 8 (blue) with cells. Data is shown between 1 kHz and 1 MHz.

5. Phase Plot

A plot of the phase angle of impedance comparing the device with cells to the device containing only media and attachment factor is shown in Figure 11. The data demonstrated that the phase angle began to increase from -90 degrees towards zero (indicating a transition from capacitive to resistive behavior) at about 1 kHz for the

device with cells, and at more than 10 kHz without cells for this particular RE. The same RE and CE were used for the phase plot that produced the data for Figure 10 – the RE of Row A at a 5.0 mm distance from the center of the well and CE A.

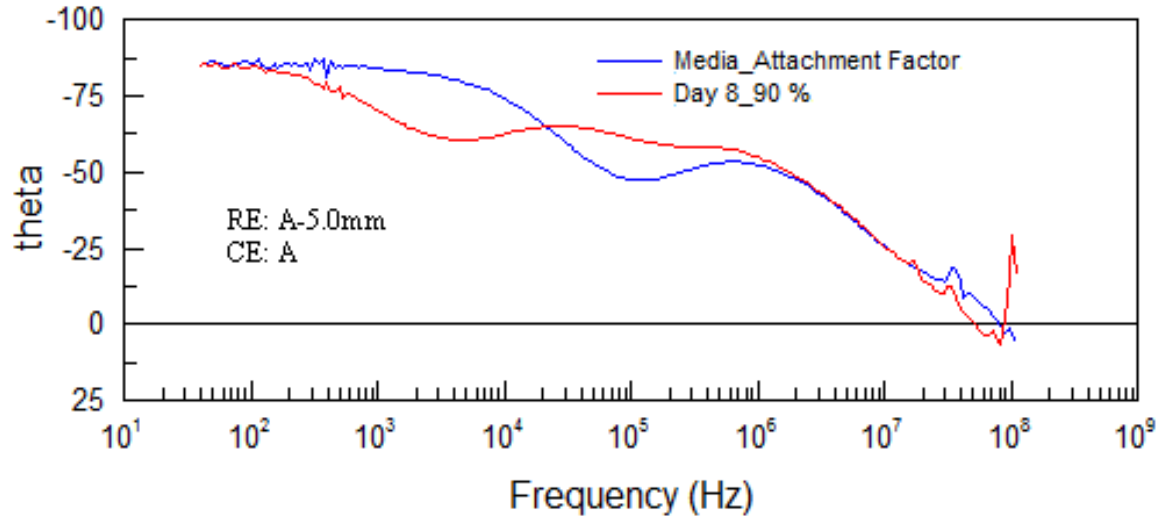


Figure 11. Impedance phase plot from the RE of row A at a 5.0 mm radius and CE A for media and attachment factor (blue), and with cells on Day 8 (red). Data from the full spectrum of impedance sensing (40 Hz to 110 MHz) is shown.

6. Nyquist Plot

A plot that displays the real versus the imaginary components of impedance is used to show differences at distinct frequencies between the device with and without cells in Figure 12. Once again, the RE of Row A that was 5.0 mm from the center of the well and CE A were used for the RE/CE configuration, in this case to demonstrate changes in the real and imaginary components of impedance with and without cells. The impedance data for the device with media only, was compared to the impedance data for the device on Day 8 of HUVEC growth.

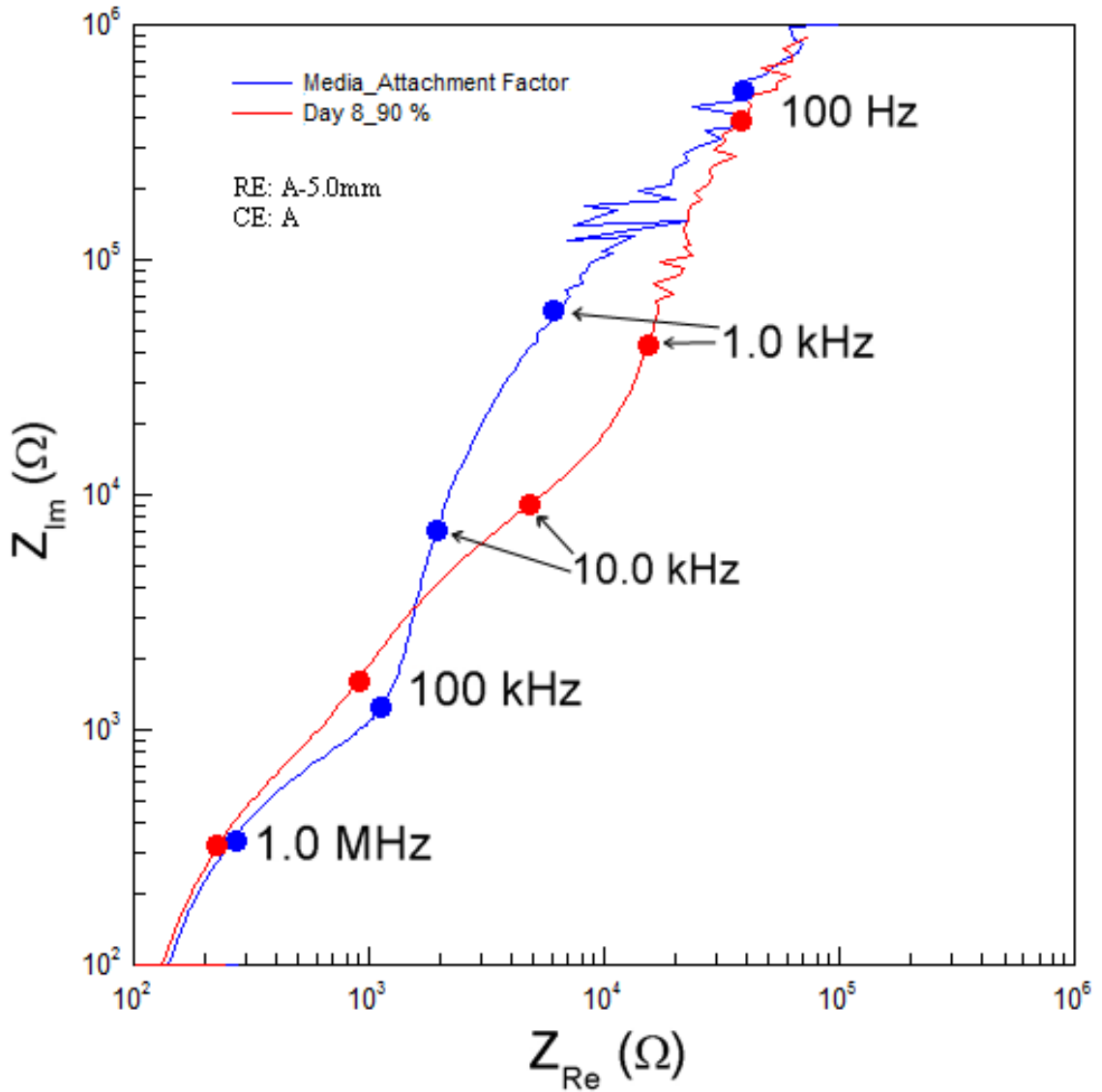


Figure 12. Nyquist plot of data from the RE of row A at a 5.0 mm radius and CE A for just media and attachment factor (blue), and for cells on Day 8 (red). The coordinates of real versus imaginary impedance are shown at distinct frequencies for the two conditions (with and without cells).

B. Shear Stress Calculations

1. Analytical Calculation

Using values for the orbit diameter of the device (0.95 cm) during fluid flow

experiments, the density of culture media (997.3 kg/m^3), and the viscosity of the culture media (0.00101 kg/m-s), which are the same values used by Dardik *et al.* (2005), an analytical calculation that the group describes as maximum theoretical shear stress was made. This value has also been described to represent a shear stress level of constant magnitude acting across the central part of the bottom of an orbiting dish (Thomas, 2007). Using the experimental speed of 75 rpm, the orbital shear stress was calculated using the aforementioned formula of Equation (8). The use of this equation yields a wall shear stress value of 2.1 dynes/cm^2 .

2. Computational Model

Colleagues at our institution performed a CFD simulation using our physical parameters (Thomas *et al.*, 2011) and assuming the same above-mentioned constant values of Dardik *et al.* (2005). The dimensions of the system were taken into account for this CFD model, which generated the wall shear stress values acting on the bottom surface of an orbiting dish. The computational model assumed a cylinder radius of 1.75 cm, a height of 2.0 cm, a static fluid height of 2.0 mm, an orbit radius of 0.95 cm, and an orbital speed of 75 rpm. Wall shear stress values were given as a function of angular position within the cylinder, throughout one orbit, at varying radii in table format as part of the supplied CFD results. The radii used were 2.5 mm, 5.0 mm, 7.5 mm, 10.0 mm, 12.5 mm, and 15.0 mm. The peak magnitude and the range of shear stress values were given for each of these radial positions. The maximum wall shear stress at 5.0 mm was 1.44 dynes/cm^2 with a range of 0.98 dyne/cm^2 to 1.44 dynes/cm^2 ; at 7.5 mm the maximum was 1.61 dynes/cm^2 with a range of 0.88 dyne/cm^2 to 1.61 dynes/cm^2 ; at 10.0 mm the maximum was 1.78 dynes/cm^2 with a range of 0.77 dyne/cm^2 to 1.78 dynes/cm^2 ;

at 12.5 mm the maximum was 2.29 dynes/cm² with a range of 0.65 dyne/cm² to 2.29 dynes/cm²; and at 15.0 mm the maximum was 2.07 dynes/cm² with a range of 0.45 dyne/cm² to 2.07 dynes/cm². A visualization of the shear stress contour created on the bottom of the orbiting cylinder in the simulation was supplied by our colleagues in the form of Figure 13, which is seen below (units in dynes/cm²). All computed values are in the Appendix.

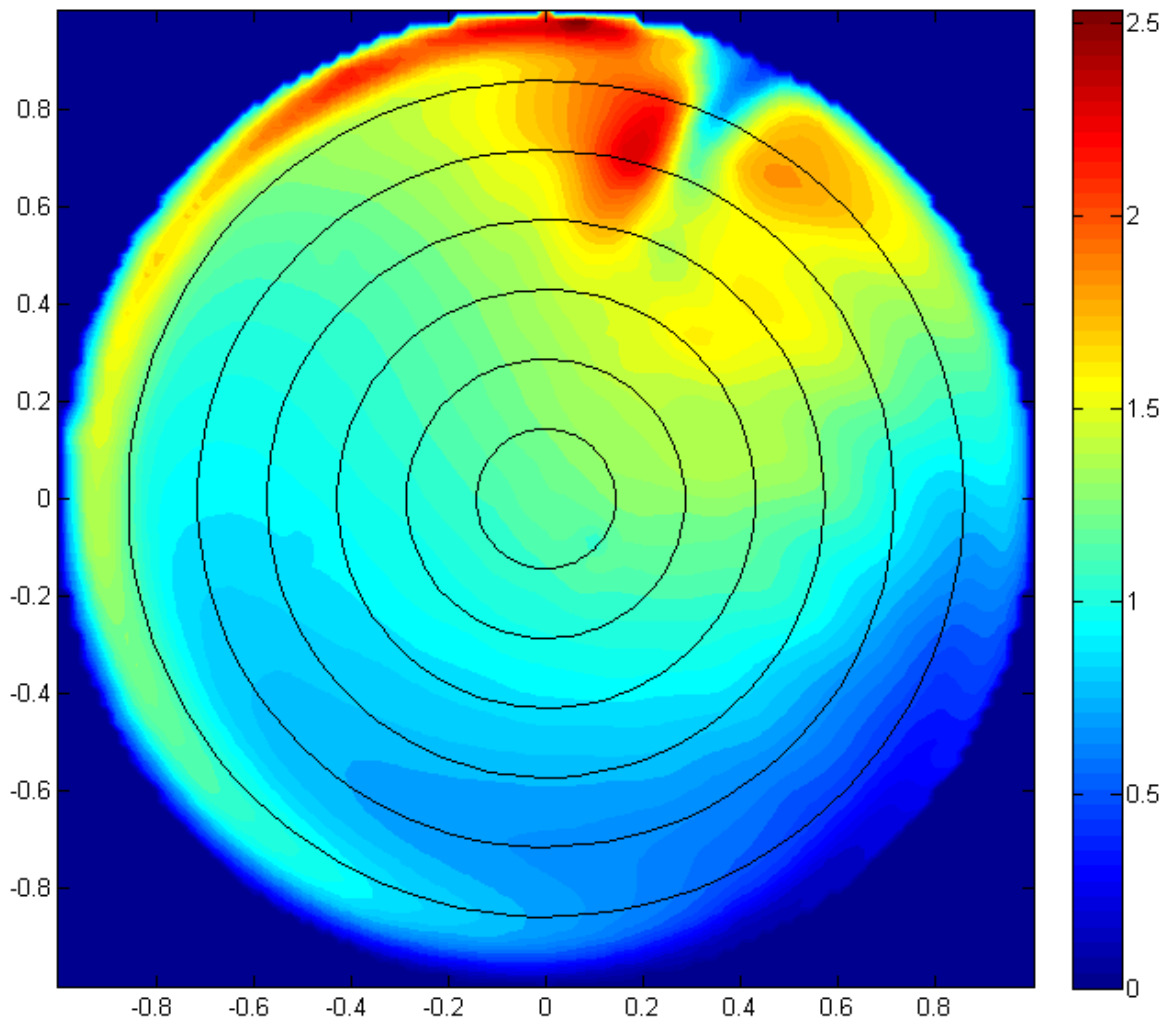


Figure 13. A contour plot of wall shear stress magnitude and the radii examined. Units of shear stress magnitude are shown in dynes/cm².

C. Shear Stress Response

1. Cell Layer Resistance

An examination of the changes in TER over the two-hour shears stress exposure period was done in the consideration of RE radial position during fluid flow. The TER measures were normalized to their baseline values, meaning the resistances of the cell layer for each RE immediately prior to the onset of hydrodynamic shear stress. Plots of the normalized TER as a function of time, with fifteen-minute intervals, were generated for each RE that was surveyed during the study. Percentage errors between the circuit model of best fit and a fit of equivalent accuracy were shown as error bars for these plots. The RE of Row B that was 15.0 mm from the center of circulation, produced a set of normalized TER values displayed in Figure 14, using bipolar impedance sensing with the CE from Row B.

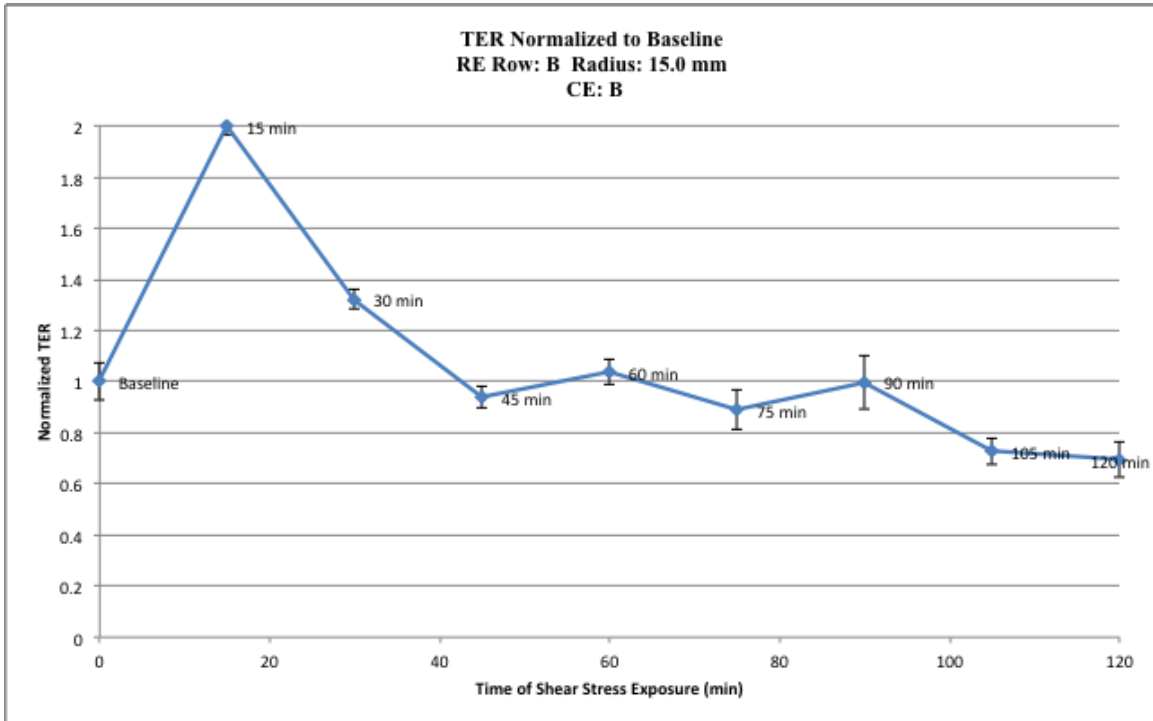


Figure 14. TER normalized to its baseline value and plotted over two hours of shear stress exposure for the RE of Row B at a radius of 15.0 mm. Error bars are plus or minus the percentage deviation of TER from a circuit element of similar goodness of fit.

Monolayer resistance increased approximately two-fold within the first fifteen minutes of shear stress exposure, followed by a decline that left it still above its baseline value after thirty minutes of total fluid flow time. From there it hovered around baseline, then dropped to 70% of the original TER after two-hours of fluid flow. The RE sampled in this case was positioned at a 15.0 mm radius from the center of circulation during fluid flow.

The RE that was at a radius of 15.0 mm (the maximum of any of the device electrodes) in Row A as opposed to Row B was coupled with CE A. The plot of TER from this electrode configuration, both immediately preceding and during the two hours of fluid flow, is shown in Figure 15.

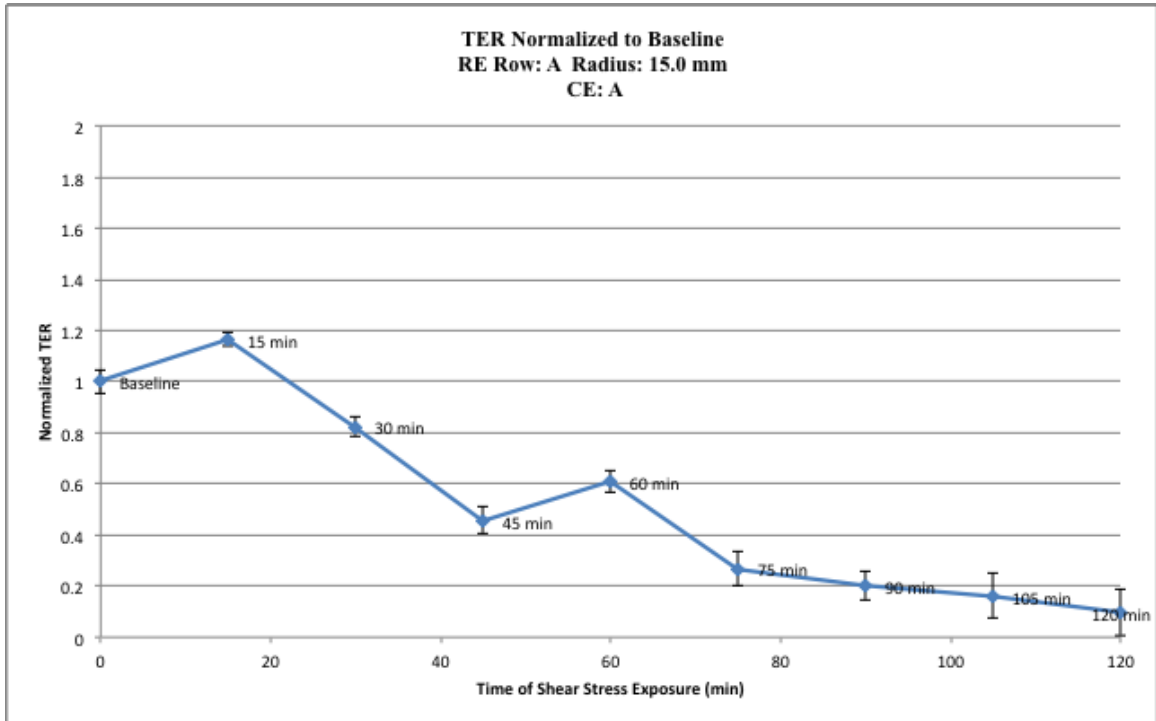


Figure 15. TER normalized to its baseline value and plotted over two hours of shear stress exposure for the RE of Row A at a radius of 15.0 mm. Error bars are plus or minus the percentage deviation of TER from a circuit element of similar goodness of fit.

For this RE, TER increased to almost 20% above its baseline value after fifteen minutes of shears stress exposure. It then dropped below baseline after thirty minutes and continued to descend for the remainder of the two hours. By the end of the time period, it had dropped all the way down to about 10% of its original baseline value, from before the onset of fluid flow.

REs at the incrementally smaller radial positions of 12.5 mm, 10.0 mm, 7.5 mm, and 5.0 mm along Row A were also surveyed during circumferential fluid flow as a way of examining the effect of varying shear stress waveform on cellular response. The TER data over time is given for the RE of Row A at 12.5 mm from the center in Figure 16.

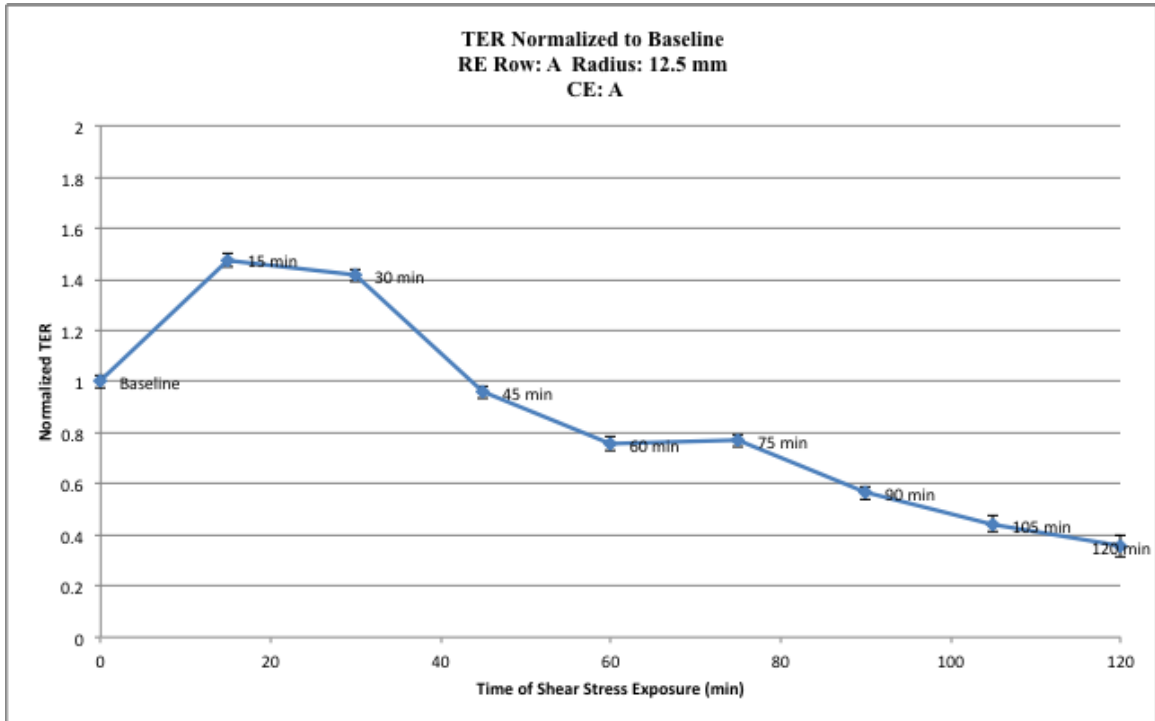


Figure 16. TER normalized to its baseline value and plotted over two hours of shear stress exposure for the RE of Row A at a radius of 12.5 mm. Error bars are plus or minus the percentage deviation of TER from a circuit element of similar goodness of fit.

At this radial position, the TER increased to almost 1.5 times its baseline value. It stayed slightly above 1.4 times baseline after thirty minutes, and then it dropped below the basal value and continued dropping to below 40% of baseline after two hours of shear stress exposure. The same initial increase in TER within fifteen minutes of the onset of fluid flow was observed for the two electrodes at the 15.0 mm radius that were reported on already in Figure 14 and Figure 15. Moving to REs closer to the center of the device well, the TER data over time is given for the RE of Row A at 10.0 mm from the center in Figure 17.

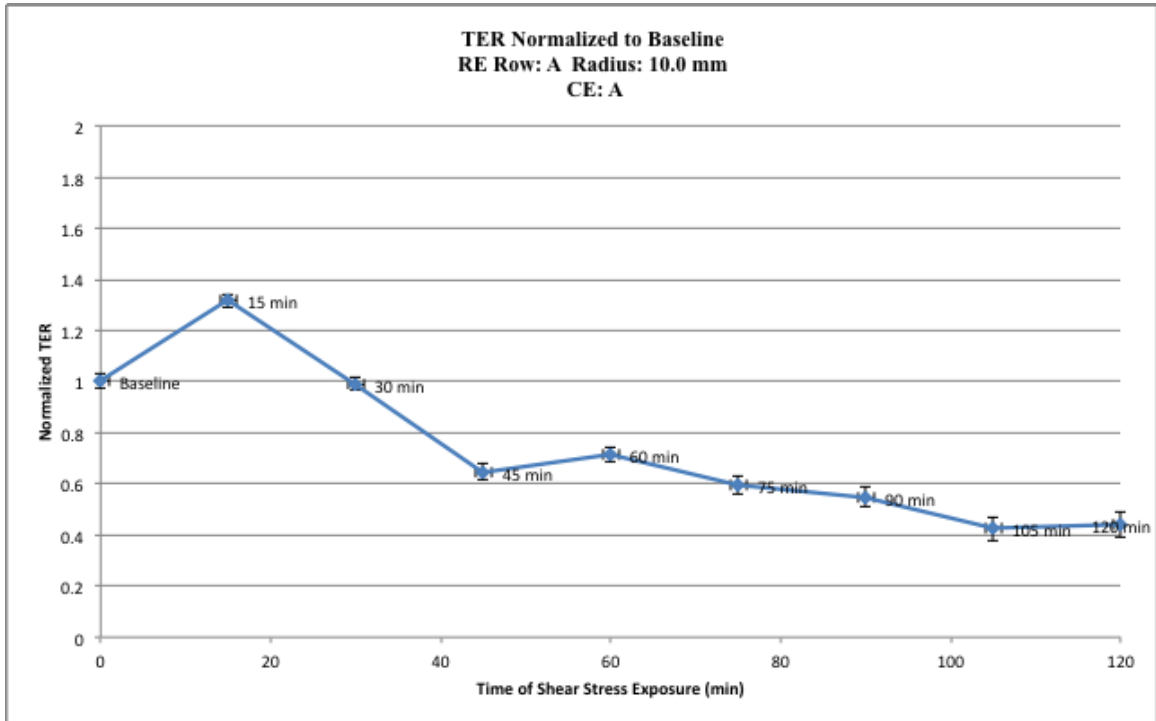


Figure 17. TER normalized to its baseline value and plotted over two hours of shear stress exposure for the RE of Row A at a radius of 10.0 mm. Error bars are plus or minus the percentage deviation of TER from a circuit element of similar goodness of fit.

The RE in Row A at 10.0 mm from the center of the well showed an increase in TER in the first fifteen minutes of fluid flow to over 1.3 times the baseline resistance. This phenomenon of increased TER after fifteen minutes occurred for all previously reported electrodes. However, the TER increase after fifteen minutes of the RE at a 10.0 mm radius in Row A pictured in Figure 17 was not as large in magnitude as it was for the RE at radius 12.5 mm in Row A in Figure 16, which in turn was not as large as the increase in TER after fifteen minutes for the RE at radius 15.0 mm in Row B in Figure 14. After peaking at 1.3 times baseline, the TER in Figure 17 decreased to slightly below baseline after thirty minutes and then falls to slightly above 40% of baseline at two hours. The TER data over time is given for the RE of Row A located 7.5 mm from the center of

the device's circular well in Figure 18.

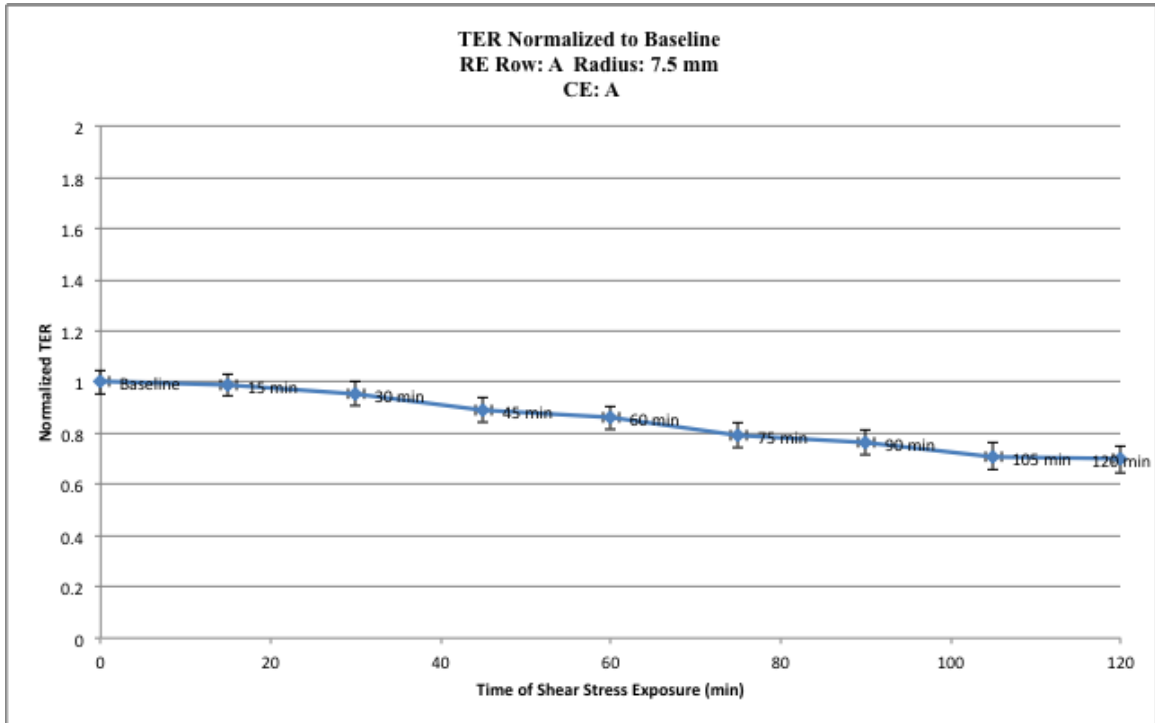


Figure 18. TER normalized to its baseline value and plotted over two hours of shear stress exposure for the RE of Row A at a radius of 7.5 mm. Error bars are plus or minus the percentage deviation of TER from a circuit element of similar goodness of fit.

TER did not increase after fifteen minutes for the RE of Row A at a radius of 7.5 mm. It stayed approximately at baseline before decreasing slowly for the rest of the study. After two hours of shear stress, the cells exhibited a TER of about 70% of baseline. This behavior of not demonstrating an initial increase in TER after fifteen minutes of flow sets these ECs apart from the ECs on REs at greater distances from the center of circulation. The RE at a 7.5 mm radius in Row A did not show an initial spike in EC monolayer resistance, which differentiates its sensed cellular response from those of the other REs reported thus far. The innermost electrode surveyed was at a 5.0 mm radius in Row A, and its TER is plotted as a function of time in Figure 19.

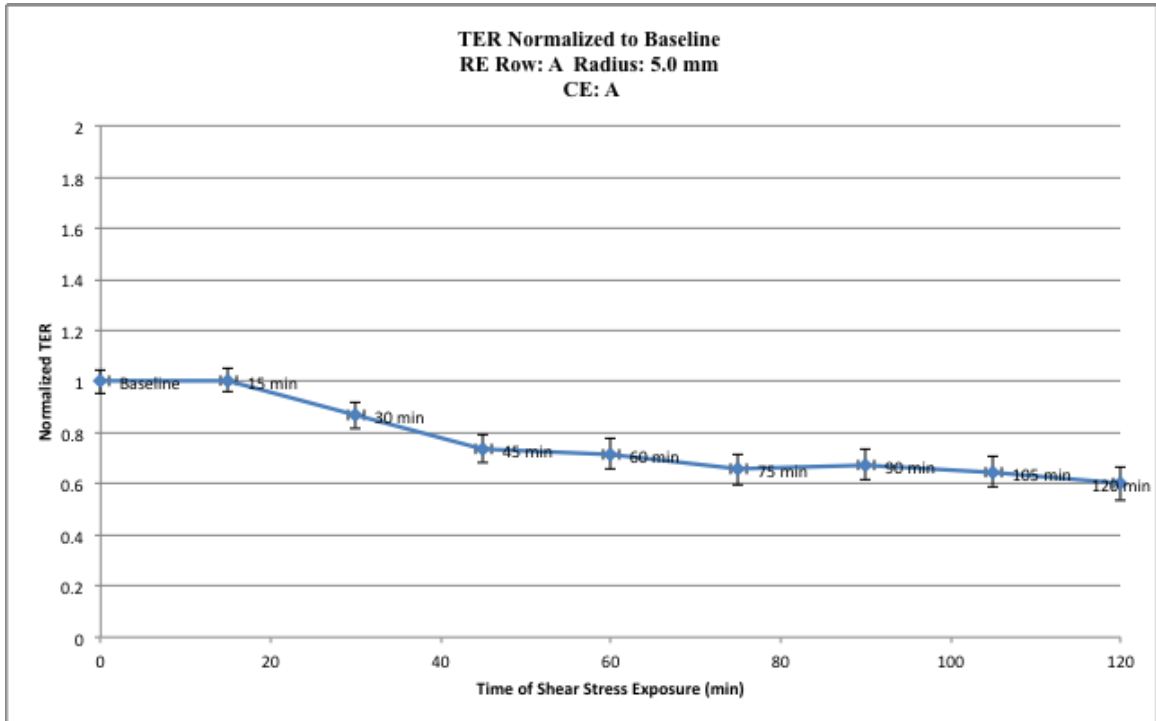


Figure 19. TER normalized to its baseline value and plotted over two hours of shear stress exposure for the RE of Row A at a radius of 5.0 mm. Error bars are plus or minus the percentage deviation of TER from a circuit element of similar goodness of fit.

The cells on this RE also did not show an increase in TER after fifteen minutes. Once again, as for the RE pictured in Figure 18, it stayed relatively unchanged after fifteen minutes, at which time it began to decline. The TER of the electrode at 5.0 mm from the center pictured in Figure 19 also declined steadily from thirty minutes onward. TER at the end of the two hours of shear stress was approximately 60% of its initial value.

2. Cell Layer Capacitance

Changes in the value of the capacitor that models the cell layer in terms of capacitance increases were all within three-fold of the baseline value. In one set of impedance data, namely that of the RE from Row B pictured in Figure 20, cell layer

capacitance dropped to roughly a quarter of its baseline value before increasing to slightly above baseline at the end of the two-hour period. This drop represented the largest relative decrease in cell layer capacitance observed over the two-hour time course.

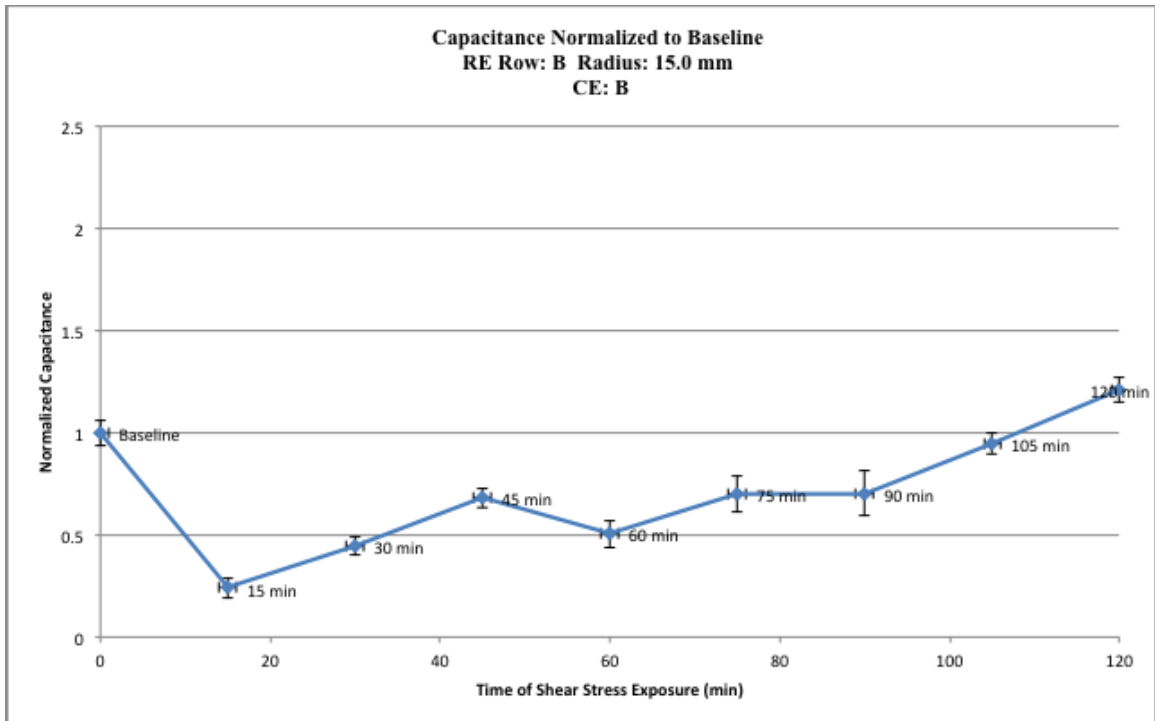


Figure 20. Cell layer capacitance normalized to its baseline value and plotted over two hours of shear stress exposure for the RE of Row B at a radius of 15.0 mm. Error bars are plus or minus the percent deviation of capacitance from a circuit element of similar goodness of fit.

The cell layer capacitance of the RE of Row A at a 15.0 mm radius also dropped during the first thirty minutes of fluid flow, although not as severely as for the case shown in Figure 20. This capacitance data from an RE at the same radius is shown below in Figure 21.

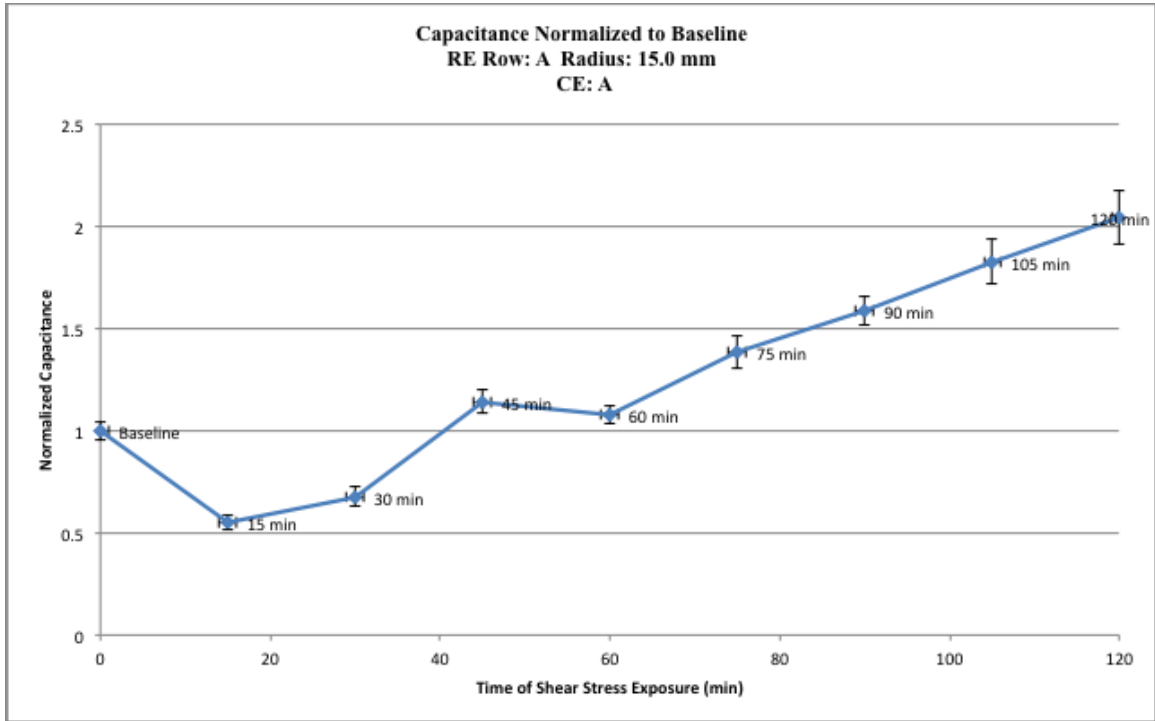


Figure 21. Cell layer capacitance normalized to its baseline value and plotted over two hours of shear stress exposure for the RE of Row A at a radius of 15.0 mm. Error bars are plus or minus the percent deviation of capacitance from a circuit element of similar goodness of fit.

The cell layer capacitance decreased to almost half of its original value, before recovering, for the cell model circuit fit to the impedance of the cells on top of the RE described in Figure 21. It eventually reached a level of more than twice baseline at the end of the two-hour period of shear stress exposure. A similar sort of pattern was observed for the cells at a radial distance of 12.5 mm as shown in Figure 22.

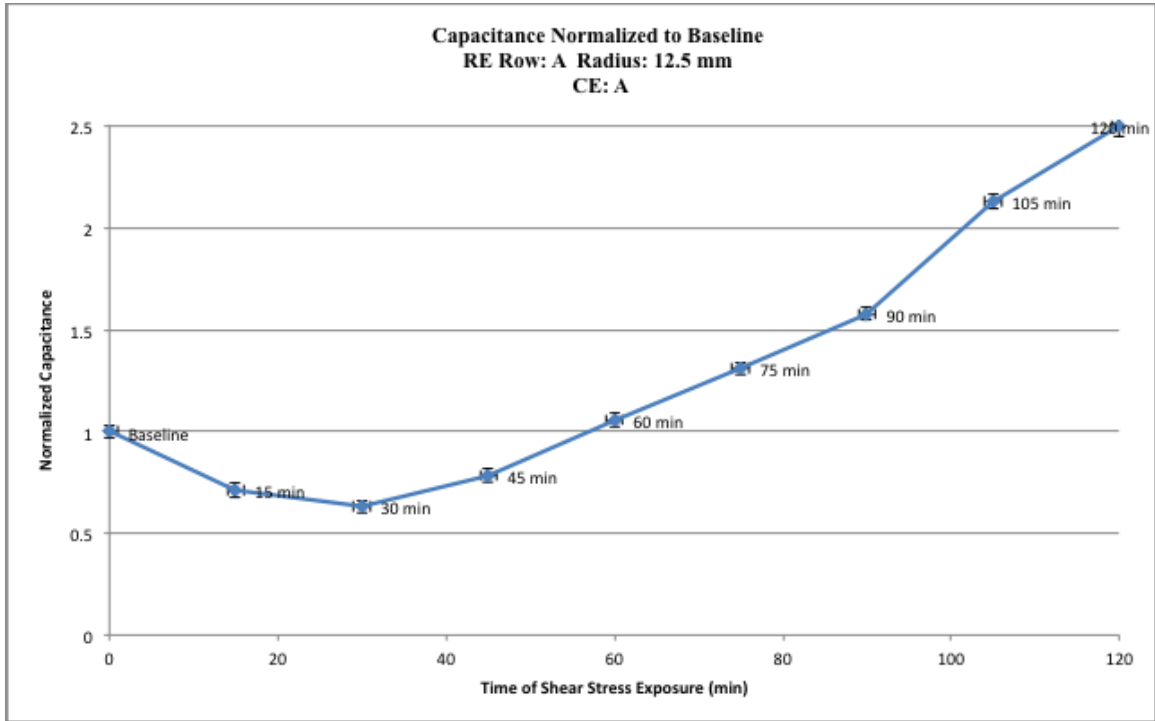


Figure 22. Cell layer capacitance normalized to its baseline value and plotted over two hours of shear stress exposure for the RE of Row A at a radius of 12.5 mm. Error bars are plus or minus the percent deviation of capacitance from a circuit element of similar goodness of fit.

The cell layer capacitance stayed below its baseline value but above 50% of that level over the course of the first forty-five minutes of shear stress exposure. This drop in the capacitance of the EC layer at the onset of flow has been observed for every RE presented so far, but this one lasts longer in duration, taking sixty minutes to recover above baseline. At the end of two hours, the measured cell layer capacitance is about 2.5 times baseline. The case is similar for the RE of Row A at a radius of 10.0 mm shown in Figure 23. It presents a case where the period of shear stress causes the measured cell layer capacitance to initially drop about 30%, followed by an increase to over 2.5 times baseline.

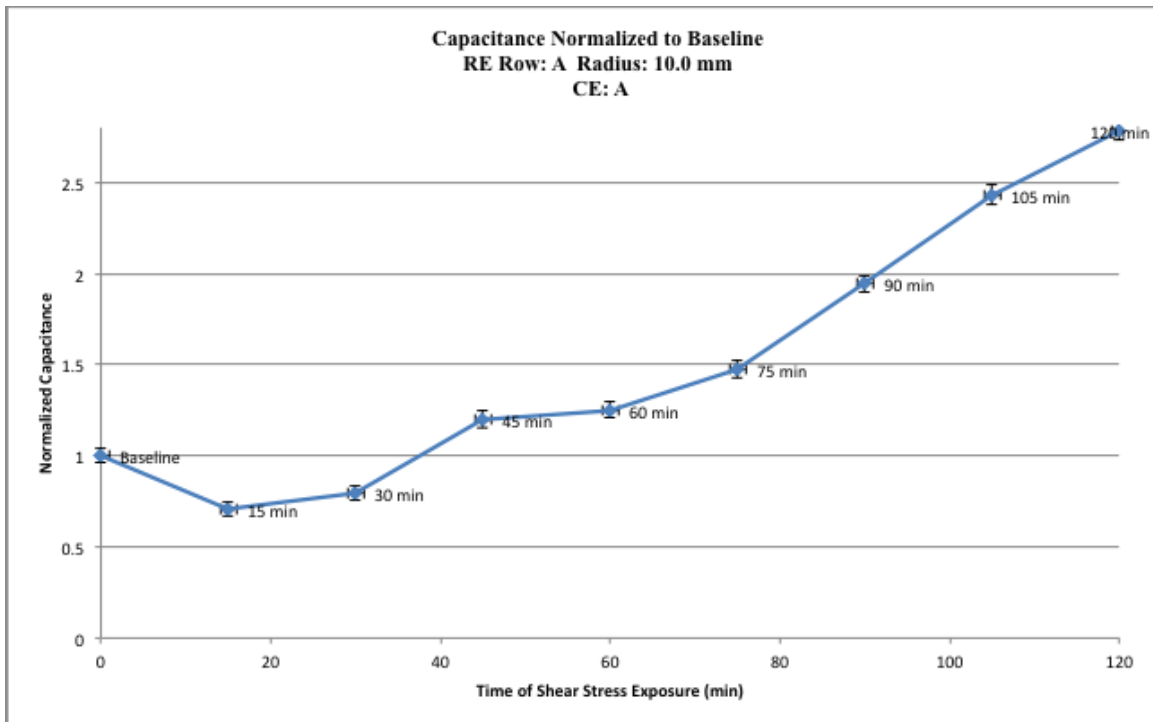


Figure 23. Cell layer capacitance normalized to its baseline value and plotted over two hours of shear stress exposure for the RE of Row A at a radius of 10.0 mm. Error bars are plus or minus the percent deviation of capacitance from a circuit element of similar goodness of fit.

At lower radial positions within the well than those described so far, a similar type of behavior in normalized capacitance was observed. TER did not change dramatically when measured for REs at radii of 5.0 mm and 7.5 mm as shown in Figures 18 and 19. However, at these same radii, capacitance either doesn't increase nearly as much towards the end of the experiment as for many of the reported cases, or it doesn't exhibit much of an initial drop in capacitance after fifteen minutes of shear stress exposure. This initial drop in cell layer capacitance following the onset of fluid flow occurred for impedance taken from every RE except one. The overshoot of relative capacitance above its baseline at later time-points during shear stress exposure is far less

for the RE at a 7.5 mm radius, which is depicted in Figure 24, than for others described.

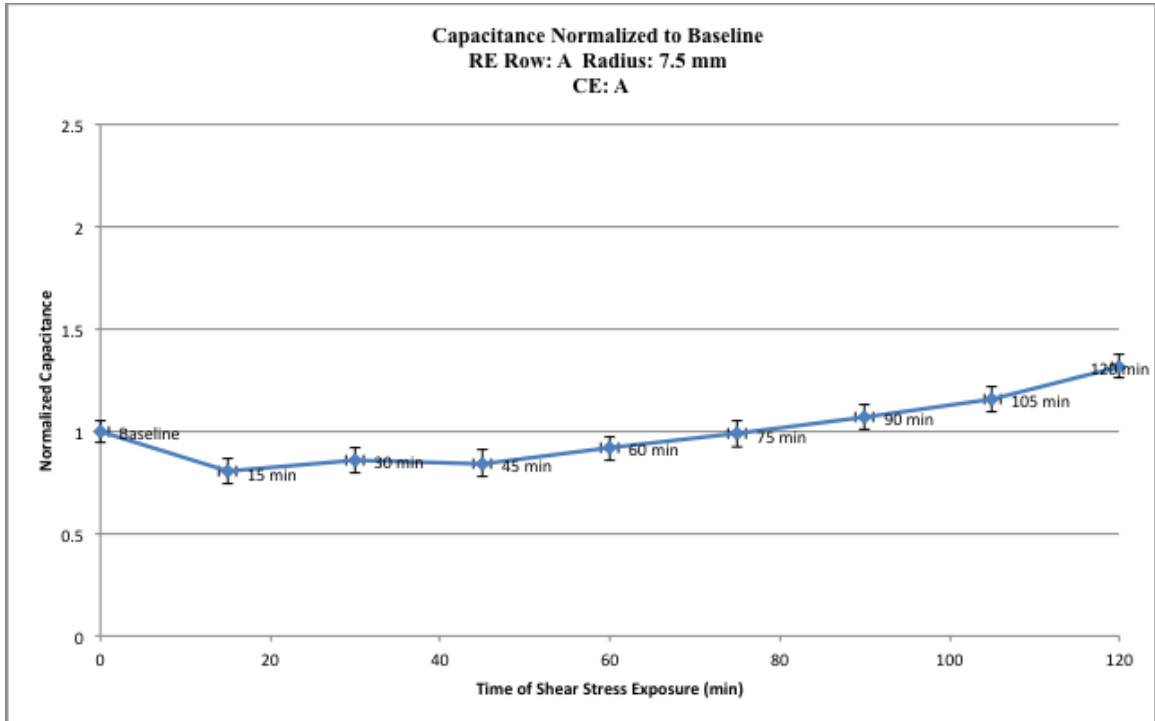


Figure 24. Cell layer capacitance normalized to its baseline value and plotted over two hours of shear stress exposure for the RE of Row A at a radius of 7.5 mm. Error bars are plus or minus the percent deviation of capacitance from a circuit element of similar goodness of fit.

Figure 25 demonstrates how the measured cell layer capacitance of the RE at a 5.0 mm radius stays virtually unchanged after fifteen minutes; it declines only slightly. It then increases to over two-fold higher than its baseline capacitance, similar to the characteristic time-responses of measured capacitance seen at other radial positions.

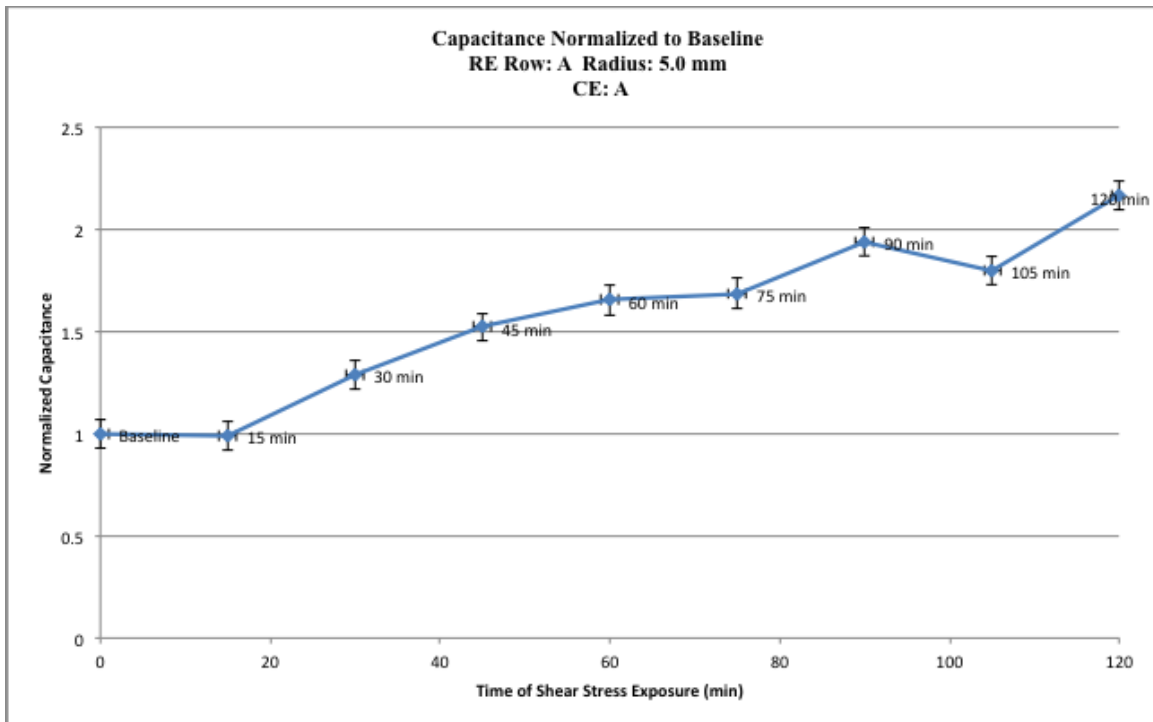


Figure 25. Cell layer capacitance normalized to its baseline value and plotted over two hours of shear stress exposure for the RE of Row A at a radius of 5.0 mm. Error bars are plus or minus the percent deviation of capacitance from a circuit element of similar goodness of fit.

3. Bode Plot

A plot of the magnitude of impedance versus frequency on a log-log scale reveals changes that occur for one of the cell-covered electrodes when the ECs forming a monolayer on the bottom of the device are subjected to shear stress. During static conditions before shear stress exposure, the impedance varies visually on the Bode plot for the electrode without cells, in contrast to the electrode with cells. Following the onset of shear stress, the impedance of the electrode increases in the same range of AC frequencies that can be used to visually discern between the cell-covered electrode and the electrode with only media and attachment factor. This frequency range is from 3 kHz

to 200 kHz. The same bandwidth can be used to visually detect the increase in TER after fifteen minutes of cellular shear stress exposure by inspection of the Bode plot. This visual discrimination of impedance magnitude in the given range of frequencies is confirmed quantitatively with variations in TER measured according to circuit parameter fitting (Figure 14). The Bode Plot for the RE of Row B at a radius of 15.0 mm is shown in Figure 26.

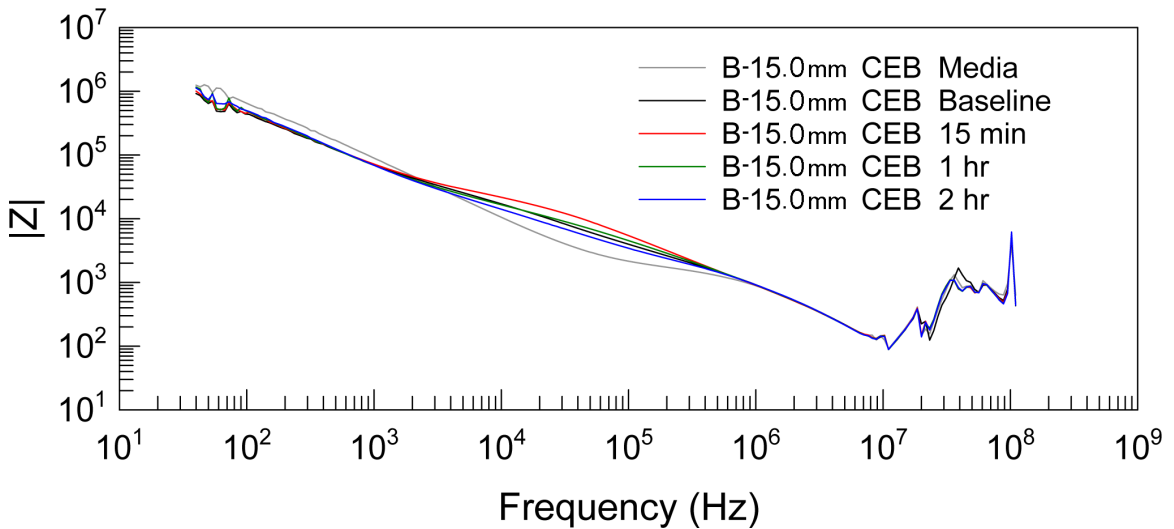


Figure 26. A Bode plot of the impedance of the electrochemical system over the full spectrum of recording frequencies (40 Hz to 110 MHz). Data is shown for the RE from Row B at a radius of 15.0 mm. Impedance is plotted for the device containing media and attachment factor (grey), HUVECs at static conditions immediately before fluid flow (black), and HUVECs at 15 minutes (red), 1 hour (green), and 2 hours (blue) of shear stress on the orbital shaker.

Impedance magnitude as a function of frequency is higher for the device with media and attachment factor only between 40 Hz and about 1 kHz in Figure 26. This result illustrates the altered behavior of the CPE with and without cells present that is

described in Table 7. In that table, it is shown how the electrode-electrolyte interfacial characteristics represented by the CPE change with the presence of cells so as to increase impedance at 100 Hz and at 1 kHz.

4. Microscopic Images

A visual record was made of images of the HUVECs on certain sections of the device surface after shear stress exposure. For this purpose an inverted microscope with bright-field illumination was used. A 10X objective lens revealed changes in cell morphology after two hours of shear stress exposure. Cells appear to undergo gap formation during this time period. This observation provides a possible explanation for the increase in cell layer capacitance at later time-points as seen in Figures 20 – 25. This statement can be made according to Seebach *et al.* (2000), who asserted that when capacitance values become artificially high, the disparity is useable as a formal indicator of gap formation in the cell monolayer. A microscopic image captured near the RE from Row A at a 5.0 mm radius, this RE having the lowest peak shear stress magnitude of the radial positions examined in the study (1.44 dynes/cm^2) according to the supplied CFD model results, is shown in Figure 27. Additionally, a microscopic image taken near the RE from Row A at a radius of 12.5 mm, the radius that had the highest peak shear stress magnitude (2.29 dynes/cm^2) of all the radii surveyed in the supplied CFD simulation that applied to the study, is pictured in Figure 28.

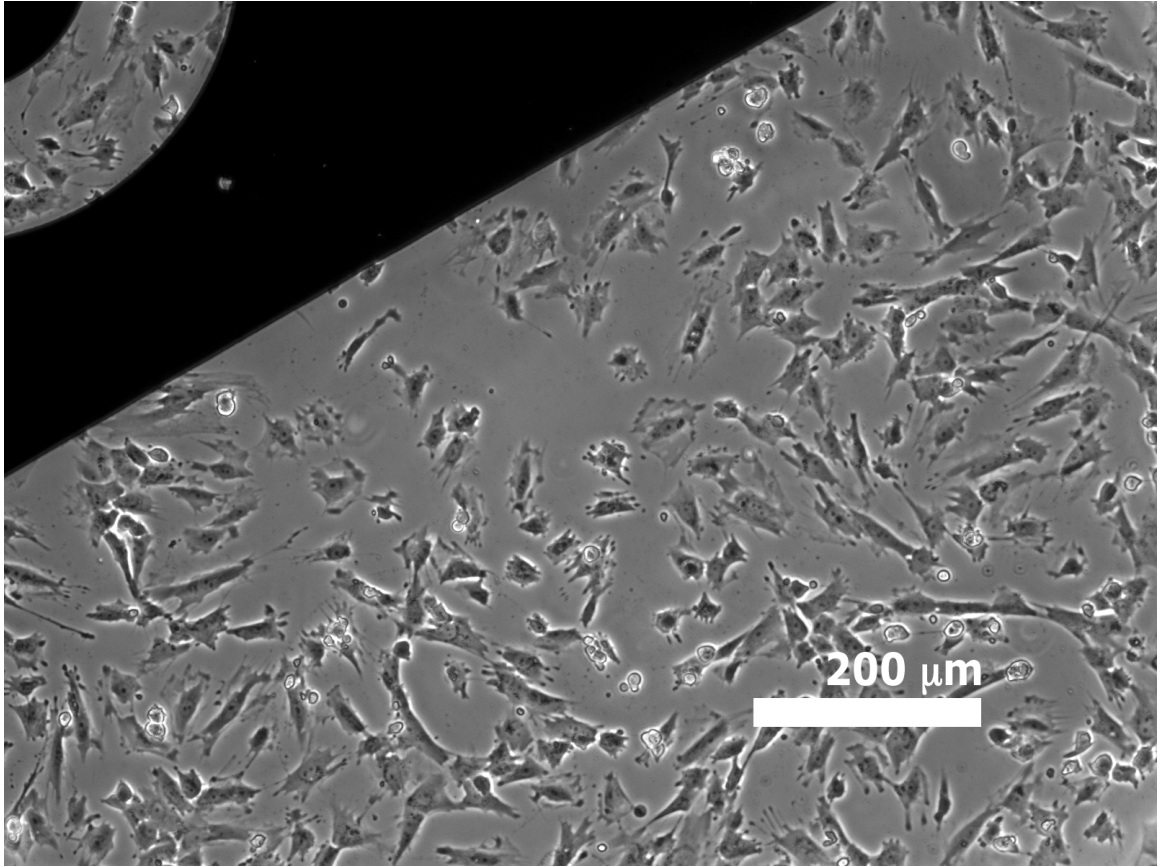


Figure 27. An image of the device surface in the vicinity of the electrode of Row A at a radius of 5.0 mm after two hours of shear stress exposure of HUVECs taken with an inverted microscope under bright-field illumination.

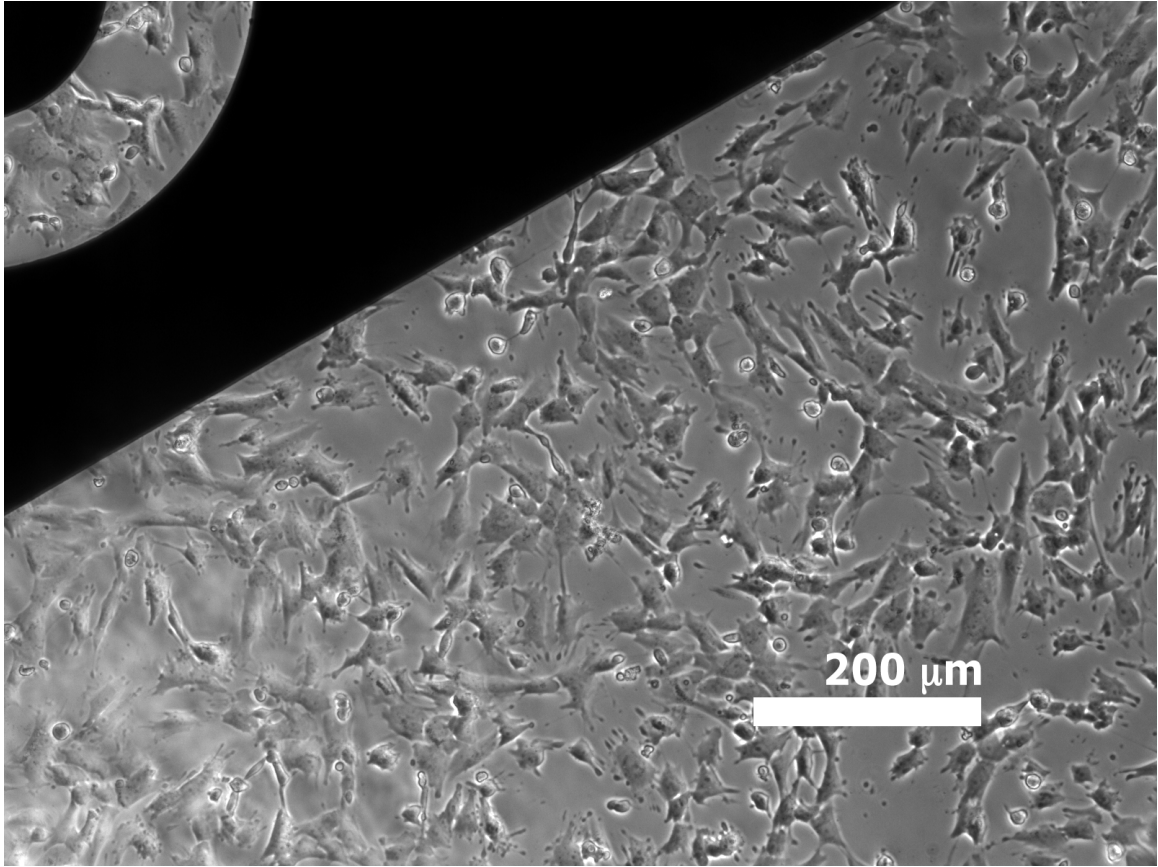


Figure 28. An image of the device surface in the vicinity of the electrode of Row A at a radius of 12.5 mm after two hours of shear stress exposure of HUVECs taken with an inverted microscope under bright-field illumination.

VI. DISCUSSION

A. Attachment and Spreading

1. Cell Layer Resistance

The specific TER is a value that normalizes resistance to electrode area. Based on results from every sampled RE on the day of peak resistance, the overall mean of specific TER was $3.87 \Omega\text{-cm}^2$ with a standard deviation of $1.39 \Omega\text{-cm}^2$ ($n = 5$). The range of specific TER among the sampled electrodes was found to be $2.77 \Omega\text{-cm}^2$ to $6.59 \Omega\text{-cm}^2$ as seen in Table 6. As previously reported, resistive values for a confluent monolayer of ECs can range from $3 \Omega\text{-cm}^2$ to greater than $1000 \Omega\text{-cm}^2$ (Seebach *et al.*, 2000). Wegener *et al.* (1999) used impedance sensing and found a specific cell layer resistance of $3.6 \pm 0.6 \Omega\text{-cm}^2$ ($n = 30$) for BAECs. Both of the aforementioned groups used the same type of circuit model, involving parallel resistive and capacitive elements, to model the cell layer (Figure 4). The presented work also employed these circuit components in the same arrangement to represent the cell layer for curve fitting. The measured TER values demonstrate the ability of the process that has been described for impedance sensing to produce data that agree with established reported results. The percentage error deviations from best-fit circuit elements to those producing equally good fits were low on the day of peak cell layer resistance, which usually occurs when the cell layer on the device is nearly confluent. Therefore, it can be stated with confidence that empirical data supports the validity of presented TER measurements for the endothelial monolayer.

2. Constant Phase Element

The A and n parameters of the CPE from Equation (6) change in the presence of cells as contrasted with the absence of cells. The effect of these changes on the magnitude of impedance was to increase the impedance of the CPE at frequencies of 100 Hz and 1000 Hz in the absence of cells versus the presence of cells as shown in Table 7. This observation may be reflective of an effect involving focal adhesions, which physically anchor cells to the proteins of the ECM (Shyy and Chien, 2002). An alteration in the electrode-electrolyte interfacial properties could cause changes in the CPE, which models this component of the system. Therefore, it may be the presence of focal adhesions between cells and the protein coating on the electrode surface that results in a lowering of CPE impedance, as measured for the electrochemical system.

Wegener *et al.* (1999) made the observation that the CPE electrical characteristics changed as a function of the presence or absence of BAECs on the electrodes used for impedance sensing. At the time of their study publication, the authors had no complete explanation for the changes in CPE parameters, but they stated that research is ongoing. Furthermore, it was mentioned by Rahman *et al.* (2009) that because cells form close contact with the electrode during these studies, the interfacial impedance parameters should be expected to change in the presence of cells. These published results point to a possible explanation for the altered CPE parameters observed in the presented work.

B. Shear Stress Response

1. Cell Layer Resistance

A wide variety of effects on the endothelial monolayer have been observed in

response to exposure to fluid flow *in vitro*. These effects include increased monolayer permeability to macromolecular compounds, changes in intercellular junctional structure, and cell migration, as well as biochemical and physiological modifications (DePaola *et al.*, 2001). Dardik *et al.* (2005) showed differential effects on BAECs at independent locations within an orbiting six-well dish. The results of a CFD simulation that was supplied to our group showed different peak magnitudes of wall shear stress that occurred on the bottom of the orbiting cylinder. The simulated peak shear stress values that occurred at radial locations corresponding to REs that were sampled during the shear stress response study were pertinent to the interpretation of results. The maximum in dynes/cm² for one orbit at 5.0 mm was 1.44 dynes/cm², at 7.5 mm it was 1.61 dynes/cm², at 10.0 mm it was 1.78 dynes/cm², at 12.5 mm it was 2.29 dynes/cm², and at 15.0 mm it was 2.07 dynes/cm². These same radial positions were surveyed during the impedance sensing experiments with fluid flow while the device orbited at 75 rpm.

For all of the REs at radial locations of 10.0 mm or greater, there was an initial spike in TER above baseline after fifteen minutes of shear stress exposure. The only electrodes that did not exhibit this TER overshoot were at radial locations of 5.0 mm, and 7.5 mm. This result demonstrates a measureable observation of shear stress-correlated cellular properties. Although the absolute change in the maximum wall shear stress, calculated numerically in the simulation as it pertained to radial locations in the study, was low, at a difference of 0.85 dyne/cm², the normal physiological range of shear stress values experienced in the venous system is 1 – 6 dynes/cm² (Chiu and Chien, 2011). The HUVECs used in the study were cells of the venous system, so this setting represents a physiologically relevant environment in which EC function is assessed. Cellular effects

correlated with radial locations within the dish may be the result of varying shear stress levels and/or waveforms within the orbiting circular well.

Using BAECs in flow-based impedance sensing experiments, DePaola *et al.* (2001) observed an increase of cell layer resistance to 1.2 to 1.3 times baseline after fifteen minutes of flow, followed by a decrease to 1.1 times baseline after thirty minutes. A similar trend was observed in the reported data. Of the cells that were on REs at a radius of 10.0 mm or more, of which there were four, an overshoot of TER occurred above baseline that ranged anywhere from slightly less than 1.2 times to 2 times baseline. Of these four REs experiencing an initial flow-induced TER spike, two remained above baseline, one fell below it, and one returned to it after thirty minutes of fluid flow. Seebach *et al.* (2000) observed a similar type of effect, showing a shear stress-dependent, graded correlation to the relative increase in TER after fifteen minutes of flow.

DePaola *et al.* (2001) suggested that a possible cause for these observations could be a decrease in the height of the space separating the substrate and the cells following the onset of flow. They mentioned that when initially exposed to flow, the cells may deform under the sudden increase in shear and pressure forces, pushing the ECs closer to the substrate while at the same time cell radius might increase, which could serve to increase TER. Seebach *et al.* (2000) made microscopic visual observations of PSECs under shear stress, and showed that the initial increase in TER was associated with an inhibition of the zigzag cellular movements that occur normally under static conditions. Therefore, they suggested, the decrease in cell fluctuations following the onset of shear stress may represent a stabilization of the cell-to-cell junctions, which may result in an increase in TER. The group mentioned that after twenty minutes of shear stress

application, the magnitude of impedance detected increased between 1 kHz and 300 kHz, and this compares well to the spectrum of frequencies over which shear stress-induced changes in the impedance magnitude of the electrochemical system are pictured in Figure 26.

The impedances of the electrodes of Rows A and B that were both located at radial positions of 15.0 mm were recorded and compared. The plots of the data are shown in Figure 14 and Figure 15. The initial spike in TER was greater (two times baseline) for the RE from Row B than it was for the RE from Row A (slightly less than 1.2 times baseline). This result demonstrates that there can be variability in the time-dependent impedance characteristics of the cells when exposed to the same shear stress waveform. Although the cells on both REs were exposed to the same peak wall shear stress level (2.07 dynes/cm^2 based on the supplied simulation), there was a difference in the relative increase in TER after fifteen minutes of fluid flow. This observation points to the need to measure multiple electrodes from the same radial position in order to possibly demonstrate statistically significant cellular changes specific to RE radial position. It can be stated that all electrodes sampled that were at least 10.0 mm or more from the center of circulation showed a peak in TER above its baseline value after fifteen minutes of shear stress exposure (Figures 14 – 17). On the other hand, all electrodes sampled at a radial distance of 7.5 mm or less showed no increase in TER after fifteen minutes, and instead the value remained steady before falling (Figure 18 and Figure 19). The range of maximum wall shear stress levels from the CFD simulation that corresponded to electrodes showing initial increases in TER was from 1.78 dynes/cm^2 to 2.29 dynes/cm^2 . Applying the computational results, the range of maximum wall shear stress levels

experienced by the ECs at the radial locations where no increase in TER was observed (5.0 mm and 7.5 mm), was from 1.44 dynes/cm² to 1.61 dynes/cm².

Although Seebach *et al.* (2000) found that the TERs of confluent monolayers of PSECs increased and peaked after twenty minutes of exposure to shear stress at 10 dynes/cm², their results showed that after peaking, TER declined for approximately the next six hours, reaching a low of less than 85% of their baseline value. Likewise, DePaola *et al.* (2001) found that after the first fifteen minutes of fluid shear stress, BAEC monolayer resistance started to decrease, falling to 85% of its baseline value after five hours. The same decrease in TER, which brought it below its baseline value after two hours of sustained fluid flow exposure, was observed in the study described herein that was performed with HUVECs. During the two-hour period of shear stress, of the electrodes sampled that showed an initial spike in TER, the maximum relative decreases in TER below baseline ranged from about 30% to 90% (Figures 14 – 17). Meanwhile, the range of relative decreases in TER below baseline for electrodes that did not show any initial rise in TER was from about 30% to 40% (Figure 18 and Figure 19), which was a range encompassing much smaller relative decreases when compared to that of the aforementioned electrodes that did show an initial increase in TER. Seebach *et al.* (2000) found that following the initial peak of TER, the decrease of the value below baseline was accompanied by a shear stress-induced change in cell shape. The authors suggested that the motility of the individual ECs within confluent cultures reported in another study (Dieterich *et al.*, 2000) might suggest that cell-to-cell adhesion must be weakened first, so that cells can move relative to each other (Seebach *et al.*, 2000). Seebach *et al.* (2000) suggested that this mechanism could be the cause of the decrease in the TER of PSECs

below baseline seen after about thirty minutes of shear stress exposure.

2. Cell Layer Capacitance and Microscopic Images

After fifteen minutes of fluid flow, cell layer capacitance dropped to as low as about 25% of baseline for the RE of Row B at a 15.0 mm radius (Figure 20), but only dropped about 1% for the RE of Row A at a 5.0 mm radius (Figure 25). The RE of Row A was the only RE that did not show a drop of at least 20% from its original cell layer capacitance value. Every RE that was sampled showed an increase in cell layer capacitance above baseline by the end of the two-hour period of shear stress. The RE that showed the largest initial drop in capacitance (Figure 20) subsequently demonstrated a recovery of the value to about 20% above baseline. The largest relative increase in capacitance at the end of the experiment, which was almost 2.8 times baseline, was seen for the RE of Row A at a 10.0 mm radius (Figure 23). The only electrode that showed virtually no change in cell layer capacitance after fifteen minutes demonstrated a subsequent rise in the capacitive value to almost 2.2 times baseline (Figure 25). Finally, aside from the RE of Row A at 5.0 mm with only a 1% decrease in cell layer capacitance, the RE of Row A at a radius of 7.5 mm had both the smallest percentage drop (approximately 20%) in cell layer capacitance after fifteen minutes of flow, as well as the lowest percentage increase above baseline at the end of the experiment (slightly greater than 30%).

These results are somewhat consistent with those reported by DePaola *et al.* (2001). Their results showed that cell layer capacitance decreased after the initiation of flow and then after fifteen minutes, it started to increase. However, cell layer capacitance never increased more than 5% above baseline in their experiments with BAECs. It was

discussed in the results section that for the attachment and spreading experiment of the presented work, the impedance at earlier time-points with low cell coverage often did not fit the cell layer circuit model with low error percentages (Tables 1 – 5). Seebach *et al.* (2000) found cell layer capacitance to be basically constant for PSECs exposed to 10 dynes/cm² in a cone-and-plate viscometer. They stated that subconfluent cell cultures with large intercellular gaps still influenced the impedance spectra, but that if parts of the electrode were uncovered, the parallel resistor and capacitor model no longer sufficiently described the electrical properties of the monolayer. They went on to say that under these conditions the capacitance values became artificially higher than their expected value. Their cellular populations did not show intercellular gap formation after shear stress experiments, and they concluded that the constant cell layer capacitance serves as an internal control that indicates the absence of large gap formation in between cells.

Previous groups have studied static culture conditions and found that they cause tight junctions to be either poorly developed or completely absent from macrovascular ECs *in vitro* (Craig *et al.*, 1998). It should be noted that both DePaola *et al.* (2001) and Seebach *et al.* (2000) used arterial ECs in their shear stress response impedance sensing studies. Venous ECs are polygonal instead of elongated in shape, and they do not display preferred orientation to fluid flow (Rahman *et al.*, 2009; Seebach *et al.*, 2000), so different responses to shear stress should be expected from this type of cell. Furthermore, Levesque and Nerem (1985) showed that the orientation of BAECs in the direction of flow requires twenty-four hours to complete. However, in response to flow, ECs have been reported to rearrange their intercellular junctions and to begin to move horizontally to align in the direction of flow within five hours (DePaola *et al.*, 2001). The gap

formation that was observed in the orbital shear study microscopically after two hours of shear stress exposure as displayed in Figure 27 and Figure 28, may be indicative of this adaptive cellular response to the onset of shear stress. The intercellular gap formation that occurred may represent the causative factor for the large increases in cell layer capacitance, seen towards the end of the two-hour shear stress exposure period, as suggested by the findings of Seebach *et al.* (2000). One of the two REs that experienced the smallest relative decrease in TER after two hours (the RE of Row A at a radius of 7.5 mm) also experienced the lowest range of normalized changes in measured cell layer capacitance (Figure 18 and Figure 24). Therefore, it is possible that gap formation in the cell layer, which was observed microscopically at the end of two hours of shear stress exposure, may be reflected by large increases in measured cell layer capacitance.

VII. CONCLUSION

The determination of the TER of macrovascular ECs using DC techniques is often difficult due to the resistance of this type of cell being characteristically low (less than 5 $\Omega\text{-cm}^2$) (DePaola *et al.*, 2001). The presented method of impedance sensing of ECs showed accuracy in modeling empirical data with circuit fits that allowed for the determination of these types of low TER values. Changes in the area of the device surface that was covered with cells during the attachment and spreading experiment were directly reflected in increases in cell layer resistance as shown in Tables 1 – 5. The increase in errors in the values of the circuit fit components at subconfluent levels of device surface coverage with cells, when compared with conditions of high cellular surface coverage, demonstrates that the circuit model used fits data with confluent monolayers more closely than it fits data from subconfluent cell cultures. Results from confluent monolayers were characterized by low percentage error deviations in cell layer resistance from values that produce an equally good fit to the empirical data.

Endothelial responses to hydrodynamic shear stress produced visually discernable alterations of impedance between 3 kHz and 200 kHz using a log-log plot (Figure 26). These responses to shear stress entailed an initial, transient increase in TER for four electrodes at radii of 10.0 mm or greater during the first fifteen minutes of flow (Figures 14 – 17), in contrast to the observation of no such rise of TER above baseline for two electrodes at radii of 7.5 mm or less (Figure 18 and Figure 19). Additionally, those

cellular subpopulations showing an initial TER increase typically displayed a greater subsequent relative decrease in TER below baseline after two hours of fluid shear (ranging from about 30% to 90%), as compared to the cells on the two electrodes that showed no increase above baseline (ranging from about 30% to 40%).

These results could be indicative of a differential response of the ECs to varying shear stress waveforms. For example, Chakraborty *et al.* (2012) stated that using CFD and assuming an orbital speed of 100 rpm, wall shear stress remains more uniform near the center of the dish than near the sidewalls, where wall shear stress was found to fluctuate to a greater degree. This difference in the shear stress waveforms of being more pulsatile at large radii and more oscillatory near the center of the dish, could be the causative factor driving these differential trends that appear as unique, position-dependent responses of cell layer resistance observed in this study. The supplied wall shear stress numerical results show larger ranges of values during one orbit at radii of 10.0 mm and above when compared to the ranges of shear stress produced at radii of 7.5 mm and below. For example, according to the CFD results, wall shear stress values at a 12.5 mm radius change by 1.64 dynes/cm² throughout one orbit; meanwhile, wall shear stress values at a radius of 5.0 mm vary by only 0.46 dyne/cm² during the orbital period. Initial TER increases above baseline values occurred for electrodes at radial distances corresponding to peak wall shear stress levels of 1.78 dynes/cm² to 2.29 dynes/cm² according to the supplied CFD results, versus a range of 1.44 dynes/cm² to 1.61 dynes/cm² for cellular populations that showed no increase. Tables of these values are shown in the Appendix.

The increase in TER after flow onset exhibited by the cells on top of four REs

appears to replicate the findings of other researchers (DePaola *et al.*, 2001; Seebach *et al.*, 2000) who have studied EC impedance responses to shear stress and found an initial, transient increase in TER. Different theories have been put forth to attempt to explain this phenomenon. It has been suggested that decreases in the distance separating the cell layer basal side and the substrate immediately following flow onset may be responsible for the increase in TER (DePaola *et al.*, 2001). Meanwhile, other researchers have posited that the increase in TER could be reflective of a stabilization of intercellular junctions that occurs after shear stress begins (Seebach *et al.*, 2000).

Two REs at the same radial distance (15.0 mm) but from different rows (A and B) showed distinct relative initial increases in TER above baseline. They also demonstrated differences in the relative decrease of TER below baseline after two hours of shear stress. Variability in the cellular impedance responses at the same radial position in the presence of orbital fluid flow indicates the need to sample from multiple electrodes at the same distance from the center of fluid circulation. This approach is necessary in future work to produce statistically significant findings of differences between the average circuit values normalized to baseline found at specific radii.

When large increases in the cell layer capacitance in response to shear stress exposure for two hours are observed at the same time as large decreases in TER, it is reasonable to infer that intercellular gap formation has likely occurred over the RE surface. This conclusion can be drawn based on the observations of Seebach *et al.* (2000). The group observed drops in TER below baseline for PSECs subjected to 10 dynes/cm². Additionally, the group noted that the observed cell layer capacitance remained almost constant over the same time period, and that no gap formation in the cell

layer occurred. The authors of the publication asserted that when cell layer capacitance values become artificially high, the disparity can be taken as a formal indicator for gaps between cells.

Confirmation was made microscopically that intercellular gap formation occurred in the HUVEC monolayer after two hours of orbital shear. Therefore, it is likely that the increased capacitance above baseline at the end of the shear stress response study was a direct reflection of gap formation in the cell layer as supported by microscopy of the device surface at the end of the two hour period of fluid flow. Furthermore, Seebach *et al.* (2000) stated that constant cell layer capacitance serves as an internal control, indicating the absence of intercellular gap formation. In the orbital shear stress experiment, the RE that exhibited the smallest range of relative cell layer capacitance changes (Figure 24) was also one of the two electrodes with the smallest relative drop in TER after two hours (Figure 18).

Because TER provides an assessment of cell layer permeability, it is reasonable to conclude that variations in the percentage drop in TER below baseline after two hours likely indicate differences in the electrode surface area that was left uncovered due to gap formation in the cells on each electrode. In other words, because intercellular gap formation was confirmed microscopically at the end of two hours, it is reasonable to conclude that electrodes showing a large drop in TER below baseline had more area exposed due to gaps in the cell layer as compared to electrodes with a smaller drop in TER. Hence, it is likely that the increases in cell layer permeability that were manifested to various degrees in cellular subpopulations as indicated by differing percentage drops in TER after two hours, were due to intercellular gap formation. This conclusion can be

drawn because of the degree of TER decreases below baseline, which far exceeded those observed in studies with no cell layer gap formation (Seebach *et al.*, 2000). It must be noted that according to Seebach *et al.* (2000), intercellular gap formation may cause the accuracy of the circuit model that was employed in the orbital shear study at fitting the empirical data to decrease.

In closing, it can be concluded that the ability of the employed model for impedance sensing of ECs produced accurate measurements of cell layer resistance, as validated with the attachment and spreading experiment. Observations of differing trends of cellular impedance responses to shear stress conditions were found to correlate with position in a way that differentiated the responses of cells based on whether or not they were 10.0 mm or greater from the center of circulation as opposed to within 7.5 mm of it. The trends in the responses of TER to shear stress for radial positions of 10.0 mm or more followed those observed in previously published reports (DePaola *et al.*, 2001; Seebach *et al.*, 2000). Trends in capacitance followed the same path as those in the study performed by DePaola *et al.* (2001), but the degree of relative changes in capacitance normalized to baseline far exceeded those observed the study. The large increase in cell layer capacitance that occurred for every electrode observed in the orbital shear stress study provides direct evidence of intercellular gap formation according to Seebach *et al.* (2000), and this interpretation of the impedance data was confirmed by microscopy of the HUVECs at the end of the experiment.

Overall, the platform and experimental setup used to conduct endothelial shear stress response studies with real-time impedance sensing offers a non-invasive, sensitive means of measuring EC functional properties such as permeability. The design of the

system allows for the use largely of conventional cell culture techniques, while allowing assessments of cellular adaptations to fluid flow environments. Because cellular responses such as the orientation of ECs in the direction of flow have been shown to require twenty-four hours to complete (Levesque and Nerem, 1985), it is necessary to conduct shear stress response studies with impedance sensing that last longer than two hours in duration. This plan for future experiments is necessary to continue monitoring changes in ECs beyond the initial rearrangement of intercellular junctions, which is reported to occur within five hours of shear stress onset (DePaola *et al.*, 2001). Through future endeavors, researchers will be able to improve on the interpretation of the impedance of ECs when subjected to shear stress. Hopefully, longer studies will enable the correlation of cell layer electrical impedance changes with a wider range of dynamic morphological responses of cells.

REFERENCES

- Aird, W.C. (2007). Phenotypic heterogeneity of the endothelium: I. Structure, function, and mechanisms. *Circulation Research*, 100(2):158-173.
- Alberts, B., Johnson, A., Lewis, J., Raff, M., Roberts, K. and Walter, P. (2002). *Molecular Biology of the Cell*. New York: Garland Science.
- Albuquerque, M.L., Flozak, A.S. (2001). Patterns of living beta-actin movement in wounded human coronary artery endothelial cells exposed to shear stress. *Experimental Cell Research*, 270(2):223-234.
- Bergan, J.J., Pascarella, L., Schmid-Schönbein, G.W. (2008). Pathogenesis of primary chronic venous disease: insights from animal models of venous hypertension. *Journal of Vascular Surgery*, 47(1):183-192.
- Bergan, J.J., Schmid-Schönbein, G.W., Smith, P.D., Nicolaidis, A.N., Boisseau, M.R., Eklof, B. (2006). Chronic venous disease. *The New England Journal of Medicine*, 355(5):488-498.
- Blackman, B.R., García-Cardena, G., Gimbrone, M.A. Jr. (2002). A new in vitro model to evaluate differential responses of endothelial cells to simulated arterial shear stress waveforms. *Journal of Biomechanical Engineering*, 124(4):397-407.
- Brown, T.D. (2000). Techniques for mechanical stimulation of cells in vitro: a review. *Journal of Biomechanics*, 33(1):3-14.
- Chakraborty, A., Chakraborty, S., Jala, V.R., Haribabu, B., Sharp, M.K., Berson, R.E. (2012). Effects of biaxial oscillatory shear stress on endothelial cell proliferation and morphology. *Biotechnology and Bioengineering*, 109(3):695-707.
- Chen, H.C. (2005). Boyden chamber assay. *Methods in Molecular Biology*, 294:15-22.
- Chiu, J.J., Chien, S. (2011). Effects of Disturbed Flow on Vascular Endothelium: Pathophysiological Basis and Clinical Perspectives. *Physiological Reviews*, 91(1):327-387.
- Chiu, J.J., Wang, D.L., Chien, S., Skalak, R., Usami, S. (1998). Effects of disturbed flow on endothelial cells. *Journal of Biomechanical Engineering*, 120(1):2-8.

- Craig, L.E., Spelman, J.P., Strandberg, J.D., Zink, M.C. (1998). Endothelial cells from diverse tissues exhibit differences in growth and morphology. *Microvascular Research*, 55(1):65-76.
- Cooke, J.P. (2003). Flow, NO, and atherogenesis. *Proceedings of the National Academy of Sciences of the United States of America*, 100(3):768-770.
- Dardik, A., Chen, L., Frattini, J., Asada, H., Aziz, F., Kudo, F.A., Sumpio, B.E. (2005). Differential effects of orbital and laminar shear stress on endothelial cells. *Journal of Vascular Surgery*, 41(5):869-880.
- Davies, P.F. (1995). Flow-mediated endothelial mechanotransduction. *Physiological Reviews*, 75(3):519-560.
- Davies, P.F., Barbee, K.A., Volin, M.V., Robotewskyj, A., Chen, J., Joseph, L., Griem, M.L., Wernick, M.N., Jacobs, E., Polacek, D.C., DePaola, N., Barakat, A.I. (1997). Spatial relationships in early signaling events of flow-mediated endothelial mechanotransduction. *Annual Review of Physiology*, 59:527-549.
- Davies, P.F., Remuzzi, A., Gordon, E.J., Dewey, C.F. Jr, Gimbrone, M.A. Jr. (1986). Turbulent fluid shear stress induces vascular endothelial cell turnover in vitro. *Proceedings of the National Academy of Sciences of the United States of America*, 83(7):2114-2117.
- Davies, P.F., Spaan, J.A., Krams, R. (2005). Shear stress biology of the endothelium. *Annals of Biomedical Engineering*, 33(12):1714-1718.
- Dejana, E. (1997). Endothelial adherens junctions: implications in the control of vascular permeability and angiogenesis. *The Journal of Clinical Investigation*, 100(11 Suppl):S7-10.
- DePaola, N., Gimbrone, M.A. Jr, Davies, P.F., Dewey, C.F. Jr. (1992). Vascular endothelium responds to fluid shear stress gradients. *Arteriosclerosis and Thrombosis: A Journal of Vascular Biology*, 12(11):1254-1257.
- DePaola, N., Phelps, J.E., Florez, L., Keese, C.R., Minnear, F.L., Giaever, I., Vincent, P. (2001). Electrical impedance of cultured endothelium under fluid flow. *Annals of Biomedical Engineering*, 29(8):648-656.
- Dieterich, P., Odenthal-Schnittler, M., Mrowietz, C., Krämer, M., Sasse, L., Oberleithner, H., Schnittler, H.J. (2000). *Biophysical Journal*, 79(3):1285-1297.
- Doran, A.C., Meller, N., McNamara, C.A. (2008). Role of smooth muscle cells in the initiation and early progression of atherosclerosis. *Arteriosclerosis, Thrombosis, and Vascular Biology*, 28(5):812-819.

- Flaherty, J.T., Pierce, J.E., Ferrans, V.J., Patel, D.J., Tucker, W.K., Fry, D.L. (1972). Endothelial nuclear patterns in the canine arterial tree with particular reference to hemodynamic events. *Circulation Research*, 30(1):23-33.
- Franke, W. W., Cowin, P., Grund, C., Kuhn, C. and Kepprell, H. P. (1988). The endothelial junction: the plaque and its components. *Endothelial Cell Biology in Health and Disease*. New York: Plenum Press, 147-166.
- Gamry Instruments. (2008). Basics of Electrochemical Impedance Spectroscopy. *Application Note*, 1-17.
- Giaever, I., Keese, C.R. (1991). Micromotion of mammalian cells measured electrically. *Proceedings of the National Academy of Sciences of the United States of America*, 88(17):7896-7900.
- Giaever, I., Keese, C.R. (1993). A morphological biosensor for mammalian cells. *Nature*, 366(6455):591-592.
- Girard, P.R., Nerem, R.M. (1995). Shear stress modulates endothelial cell morphology and F-actin organization through the regulation of focal adhesion-associated proteins. *Journal of cellular physiology*, 163(1):179-193.
- Gitter, A.H., Bertog, M., Schulzke, J., Fromm, M. (1997). Measurement of paracellular epithelial conductivity by conductance scanning. *European Journal of Physiology*, 434(6):830-840.
- Goldstein A.S., DiMilla, P.A. (2002). Effect of adsorbed fibronectin concentration on cell adhesion and deformation under shear on hydrophobic surfaces. *Journal of Biomedical Materials Research*, 59(4):665-675.
- Goda, N., Kataoka, N., Shimizu, J., Mohri, S., Yamamoto, Y., Okuda, H., Kajiya, F. (2005). Evaluation of micromotion of vascular endothelial cells in electrical cell-substrate impedance sensing (ECIS) method using a mathematical model. *Journal of Mechanics in Medicine and Biology*, 5(2):357-368.
- Grasso, S., Hernández, J.A., Chifflet, S. (2007). Roles of wound geometry, wound size, and extracellular matrix in the healing response of bovine corneal endothelial cells in culture. *American Journal of Physiology: Cell Physiology*, 293(4):C1327-1337.
- Gray, B.L., Lieu, D.K., Collins, S.D., Smith, R.L., Barakat, A.I. (2002). Microchannel Platform for the Study of Endothelial Cell Shape and Function. *Biomedical Microdevices*, 4(1):9-16.
- Guan, J.G., Miao, Y.Q., Zhang, Q.J. (2004). Impedimetric biosensors. *Journal of Bioscience and Bioengineering*, 97(4):219-226.

- Gutierrez, E., Groisman, A. (2007). Quantitative measurements of the strength of adhesion of human neutrophils to a substratum in a microfluidic device. *Analytical Chemistry*, 79(6):2249-2258.
- Halliday, D., Resnick, R., Walker, J. (2001). *Fundamentals of Physics*. New York: John Wiley and Sons, Inc.
- Helmlinger, G., Berk, B.C., Nerem, R.M. (1996). Pulsatile and steady flow-induced calcium oscillations in single cultured endothelial cells. *Journal of Vascular Research*, 33(5):360-369.
- Helmlinger, G., Geiger, R.V., Schreck, S., Nerem, R.M. (1991). Effects of pulsatile flow on cultured vascular endothelial cell morphology. *Journal of Biomechanical Engineering*, 113(2):123-131.
- Horbett, T.A., Waldburger, J.J., Ratner, B.D., Hoffman, A.S. (1988). Cell adhesion to a series of hydrophilic-hydrophobic copolymers studied with a spinning disc apparatus. *Journal of Biomedical Materials Research*, 22(5):383-404.
- Hsu, P.P., Li, S., Li, Y.S., Usami, S., Ratcliffe, A., Wang, X., Chien, S. (2001). Effects of flow patterns on endothelial cell migration into a zone of mechanical denudation. *Biochemical and Biophysical Research Communications*, 285(3):751-759.
- Hynes, R.O. (1992). Integrins: versatility, modulation, and signaling in cell adhesion. *Cell*, 69(1):11-25.
- Jo, H., Dull, R.O., Hollis, T.M., Tarbell, J.M. (1991). Endothelial albumin permeability is shear dependent, time dependent, and reversible. *The American Journal of Physiology*, 260(6 Pt 2):H1992-H1996.
- Kantak, A.S., Gale, B.K., Lvov, Y., Jones, S.A. (2003). Platelet function analyzer: Shear activation of platelets in microchannels. *Biomedical Microdevices*, 5(3):207-215.
- Kim, D.W., Langille, B.L., Wong, M.K., Gotlieb, A.I. (1989). Patterns of endothelial microfilament distribution in the rabbit aorta in situ. *Circulation Research*, 64(1):21-31.
- Kochanek, K.D., Xu, J.Q., Murphy, S.L., Miniño, A.M., Kung, H.C. (2011). Deaths: final data for 2009. *National Vital Statistics Reports*, 60(3).
- Kraiss, L.W., Weyrich, A.S., Alto, N.M., Dixon, D.A., Ennis, T.M., Modur, V., McIntyre, T.M., Prescott, S.M., Zimmerman, G.A. (2000). Fluid flow activates a regulator of translation, p70/p85 S6 kinase, in human endothelial cells. *American Journal of Physiology: Heart and Circulatory Physiology*, 278(5):H1537-H1544.

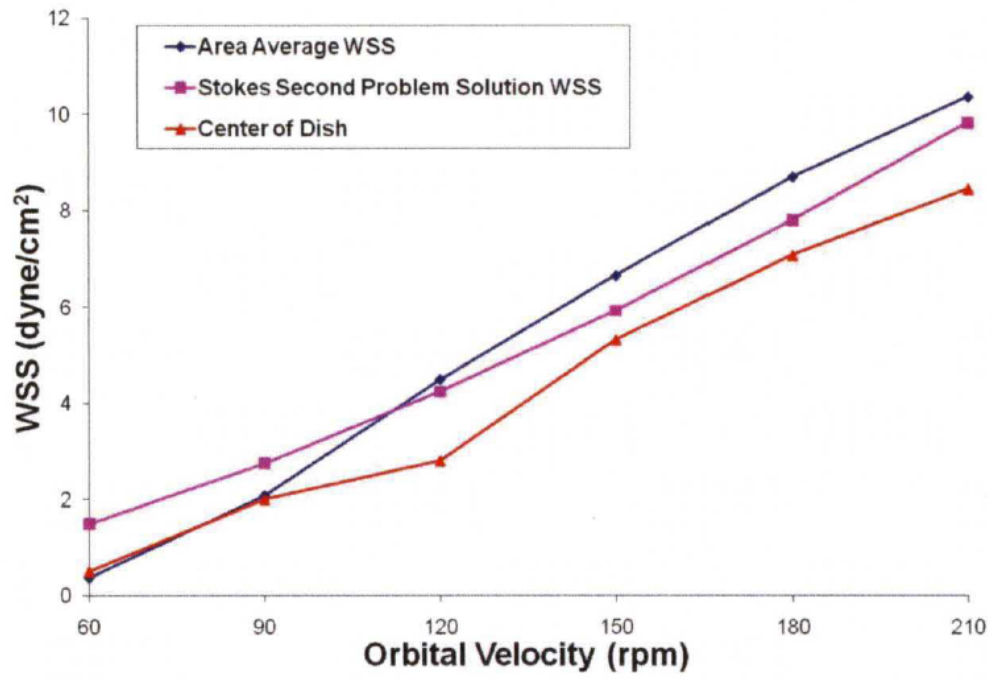
- Ku, D.N., Giddens, D.P., Zarins, C.K., Glagov, S. (1985). Pulsatile flow and atherosclerosis in the human carotid bifurcation. Positive correlation between plaque location and low oscillating shear stress. *Arteriosclerosis*, 5(3):293-302.
- Kwei, S., Stavrakis, G., Takahas, M., Taylor, G., Folkman, M.J., Gimbrone, M.A. Jr., García-Cardena, G. (2004). Early adaptive responses of the vascular wall during venous arterialization in mice. *The American Journal of Pathology*, 164(1):81-89.
- Lamallice, L., Le Boeuf, F., Huot, J. (2007). Endothelial cell migration during angiogenesis. *Circulation Research*, 100(6):782-794.
- Langille, B.L. (1996). Arterial remodeling: relation to hemodynamics. *Canadian Journal of Physiology and Pharmacology*, 74(7):834-841.
- Langille, B.L., O'Donnell, F. (1986). Reductions in arterial diameter produced by chronic decreases in blood flow are endothelium-dependent. *Science*, 231(4736):405-407.
- Levesque, M.J., Nerem, R.M. (1985). The elongation and orientation of cultured endothelial cells in response to shear stress. *Journal of Biomechanical Engineering*, 107(4):341-347.
- Levesque, M.J., Nerem, R.M., Sprague, E.A. (1990). Vascular endothelial cell proliferation in culture and the influence of flow. *Biomaterials*, 11(9):702-707.
- Ley, K., Lundgren, E., Berger, E., Arfors, K.E. (1989). Shear-dependent inhibition of granulocyte adhesion to cultured endothelium by dextran sulfate. *Blood*, 73(5):1324-1330.
- Li, N., Tourovskaia, A., Folch, A. (2003). Biology on a chip: microfabrication for studying the behavior of cultured cells. *Critical Reviews in Biomedical Engineering*, 31(5-6):423-488.
- Lo, C.M., Ferrier, J. (1998). Impedance analysis of fibroblastic cell layers measured by electric cell-substrate impedance sensing. *Physical Review E*, 57(6):6982-6987.
- Lo, C.M., Keese, C.R., Giaever, I. (1995). Impedance analysis of MDCK cells measured by electric cell-substrate impedance sensing. *Biophysical Journal*, 69(6):2800-2807.
- McLenachan, J.M., Vita, J., Fish, D.R., Treasure, C.B., Cox, D.A., Ganz, P., Selwyn, A.P. (1990). Early evidence of endothelial vasodilator dysfunction at coronary branch points. *Circulation*, 82(4):1169-1173.
- Mehta, D., Malik, A.B. (2006). Signaling mechanisms regulating endothelial permeability. *Physiological Reviews*, 86(1):279-367.

- Melkumyants, A.M., Balashov, S.A., Khayutin, V.M. (1989). Endothelium dependent control of arterial diameter by blood viscosity. *Cardiovascular Research*, 23(9):741-747.
- Miao, H., Hu, Y.L., Shiu, Y.T., Yuan, S., Zhao, Y., Kaunas, R., Wang, Y., Jin, G., Usami, S., Chien, S. (2005). Effects of flow patterns on the localization and expression of VE-cadherin at vascular endothelial cell junctions: in vivo and in vitro investigations. *Journal of Vascular Research*, 42(1):77-89.
- Noria, S., Cowan, D.B., Gotlieb, A.I., Langille, B.L. (1999). Transient and steady-state effects of shear stress on endothelial cell adherens junctions. *Circulation Research*, 85(6):504-514.
- Noria, S., Xu, F., McCue, S., Jones, M., Gotlieb, A.I., Langille, B.L. (2004). Assembly and reorientation of stress fibers drives morphological changes to endothelial cells exposed to shear stress. *The American Journal of Pathology*, 164(4):1211-1223.
- Olivier, L.A., Truskey, G.A. (1993). A numerical analysis of forces exerted by laminar flow on spreading cells in a parallel plate flow chamber assay. *Biotechnology and Bioengineering*, 42(8):963-973.
- Pascarella, L., Schmid Schönbein, G.W. (2005). Causes of telangiectasias, reticular veins, and varicose veins. *Seminars in Vascular Surgery*, 18(1):2-4.
- Phelps, J.E., DePaola, N. (2000). Spatial variations in endothelial barrier function in disturbed flows in vitro. *American Journal of Physiology: Heart and Circulatory Physiology*, 278(2):H469-H476.
- Powell, D.W. (1981). Barrier function of epithelia. *The American Journal of Physiology*, 241(4):G275-G288.
- Pratt, B.M., Harris, A.S., Morrow, J.S., Madri, J.A. (1984). Mechanisms of cytoskeletal regulation. Modulation of aortic endothelial cell spectrin by the extracellular matrix. *The American Journal of Pathology*, 117(3):349-54.
- Rahman, A.R., Lo, C.M., Bhansali, S. (2009). A detailed model for high-frequency impedance characterization of ovarian cancer epithelial cell layer using ECIS electrodes. *IEEE Transactions on Bio-Medical Engineering*, 56(2):485-492.
- Regehr, K.J., Domenech, M., Koepsel, J.T., Carver, K.C., Ellison-Zelski, S.J., Murphy, W.L., Schuler, L.A., Alarid, E.T., Beebe, D.J. (2009). Biological implications of polydimethylsiloxane-based microfluidic cell culture. *Lab on a Chip*, 9(15):2132-2139.

- Schnittler, H.J., Feldmann, H. (1999). Molecular pathogenesis of filovirus infections: role of macrophages and endothelial cells. *Current Topics in Microbiology and Immunology*, 235:175-204.
- Seebach, J., Dieterich, P., Luo, F., Schillers, H., Vestweber, D., Oberleithner, H., Galla, H.J., Schnittler, H.J. (2000). Endothelial barrier function under laminar fluid shear stress. *Laboratory Investigation*, 80(12):1819-1831.
- Shyy, J.Y., Chien, S. (2002). Role of integrins in endothelial mechanosensing of shear stress. *Circulation Research*, 91(9):769-775.
- Tardy, Y., Resnick, N., Nagel, T., Gimbrone, M.A. Jr, Dewey, C.F. Jr. (1997). Shear stress gradients remodel endothelial monolayers in vitro via a cell proliferation-migration-loss cycle. *Arteriosclerosis, Thrombosis, and Vascular Biology*, 17(11):3102-3106.
- Thomas, J.M., Chakraborty, A., Sharp, M.K., Berson, R.E. (2011). Spatial and temporal resolution of shear in an orbiting petri dish. *Biotechnology Progress*, 27(2):460-5.
- Thurston, G., Baluk, P., McDonald, D.M. (2000). Determinants of endothelial cell phenotype in venules. *Microcirculation*, 7(1):67-80.
- Tiruppathi, C., Malik, A.B., Del Vecchio, P.J., Keese, C.R., Giaever, I. (1992). Electrical method for detection of endothelial cell shape change in real time: assessment of endothelial barrier function. *Proceedings of the National Academy of Sciences of the United States of America*, 89(17):7919-7923.
- Toepke, M.W., Beebe, D.J. (2006). PDMS absorption of small molecules and consequences in microfluidic applications. *Lab on a Chip*, 6(12):1484-1486.
- Traub, O., Berk, B.C. (1998). Laminar shear stress: mechanisms by which endothelial cells transduce an atheroprotective force. *Arteriosclerosis, Thrombosis, and Vascular Biology*, 18(5):677-685.
- Tzima, E. (2006). Role of small GTPases in endothelial cytoskeletal dynamics and the shear stress response. *Circulation Research*, 98(2):176-185.
- Usami, S., Chen, H.H., Zhao, Y., Chien, S., Skalak, R. (1993). Design and construction of a linear shear stress flow chamber. *Annals of Biomedical Engineering*, 21(1):77-83.
- Weber, K.S., Nelson, P.J., Gröne, H.J., Weber, C. (1999). Expression of CCR2 by endothelial cells: implications for MCP-1 mediated wound injury repair and In vivo inflammatory activation of endothelium. *Arteriosclerosis, thrombosis, and vascular biology*, 19(9):2085-2093.

- Wegener, J., Zink, S., Rösen, P., Galla, H. (1999). Use of electrochemical impedance measurements to monitor beta-adrenergic stimulation of bovine aortic endothelial cells. *European Journal of Physiology*, 437(6):925-934.
- Xiao, Y., Truskey, G.A. (1996). Effect of receptor-ligand affinity on the strength of endothelial cell adhesion. *Biophysical Journal*, 71(5):2869-2884.
- Yeo, L.Y., Chang, H.C., Chan, P.P., Friend, J.R. (2011). Microfluidic devices for bioapplications. *Small*, 7(1):12-48.
- Yoshida, Y., Okano, M., Wang, S., Kobayashi, M., Kawasumi, M., Hagiwara, H., Mitsumata, M. (1995). Hemodynamic-force-induced difference of interendothelial junctional complexes. *Annals of the New York Academy of Sciences*, 748:104-120.
- Youdim, K.A., Avdeef, A., Abbott, N.J. (2003). In vitro trans-monolayer permeability calculations: often forgotten assumptions. *Drug Discovery Today*, 8(21):997-1003.
- Young, E.W., Simmons, C.A. (2010). Macro- and microscale fluid flow systems for endothelial cell biology. *Lab on a Chip*, 10(2):143-160.
- Ziegler C. (2000). Cell-based biosensors. *Fresenius' Journal of Analytical Chemistry*, 366(6-7):552-559.
- Zoltowski, P. (1998). On the electrical capacitance of interfaces exhibiting constant phase element behaviour. *Journal of Electroanalytical Chemistry*, 443(1):149-154

APPENDIX



The shear stress plot of Thomas *et al.*, 2011

A Table of the supplied CFD results

	average	1.1906	1.1750	1.1445	1.1001	1.0620	1.0995
	maximum	1.3247	1.4399	1.6109	1.7779	2.2938	2.0746
	Angle	2.5	5.0	7.5	10.0	12.5	15.0
1	0.000	1.2805	1.3007	1.2887	1.2208	0.9816	0.8403
2	3.636	1.2874	1.3271	1.3316	1.2615	1.0066	0.9148
3	7.273	1.2939	1.3537	1.3626	1.2706	1.0479	0.9974
4	10.909	1.3004	1.3777	1.3819	1.2706	1.1136	1.0583
5	14.545	1.3063	1.3941	1.3980	1.2847	1.1998	1.1207
6	18.182	1.3111	1.4022	1.4037	1.3212	1.2854	1.1793
7	21.818	1.3156	1.4103	1.4063	1.3731	1.3556	1.2421
8	25.455	1.3195	1.4085	1.4154	1.4302	1.4042	1.3139
9	29.091	1.3224	1.4087	1.4352	1.4900	1.4339	1.3923
10	32.727	1.3237	1.4095	1.4700	1.5459	1.4585	1.4850
11	36.364	1.3244	1.4153	1.5175	1.5903	1.4849	1.5811
12	40.000	1.3247	1.4209	1.5579	1.6240	1.5156	1.6619
13	43.636	1.3240	1.4264	1.5947	1.6330	1.5594	1.7267
14	47.273	1.3225	1.4339	1.6109	1.6269	1.5992	1.7761
15	50.909	1.3204	1.4351	1.6050	1.5964	1.6270	1.8112
16	54.545	1.3179	1.4371	1.5812	1.5498	1.6260	1.8169
17	58.182	1.3152	1.4399	1.5459	1.4887	1.5606	1.7398
18	61.818	1.3121	1.4373	1.5089	1.4233	1.4070	1.4064
19	65.455	1.3085	1.4330	1.4917	1.3957	1.2901	0.7904
20	69.091	1.3045	1.4165	1.4896	1.4874	1.5780	1.3873
21	72.727	1.3000	1.4017	1.4872	1.6615	2.1427	2.0561
22	76.364	1.2944	1.3849	1.4804	1.7768	2.2938	2.0746
23	80.000	1.2885	1.3690	1.4715	1.7779	2.1372	2.0007
24	83.636	1.2822	1.3536	1.4594	1.6987	1.9141	1.9020
25	87.273	1.2754	1.3372	1.4337	1.6008	1.7565	1.8039
26	90.909	1.2689	1.3231	1.4018	1.5095	1.6659	1.7286
27	94.545	1.2630	1.3077	1.3681	1.4539	1.6114	1.6556
28	98.182	1.2569	1.2951	1.3424	1.4283	1.5573	1.5858
29	101.818	1.2503	1.2836	1.3155	1.4028	1.4996	1.5346
30	105.455	1.2431	1.2706	1.2934	1.3606	1.4395	1.4923
31	109.091	1.2357	1.2545	1.2712	1.3186	1.3917	1.4551
32	112.727	1.2282	1.2394	1.2475	1.2808	1.3484	1.4287
33	116.364	1.2215	1.2221	1.2265	1.2482	1.3079	1.3964
34	120.000	1.2156	1.2084	1.2083	1.2185	1.2722	1.3601
35	123.636	1.2098	1.1959	1.1898	1.1907	1.2400	1.3311
36	127.273	1.2027	1.1856	1.1685	1.1644	1.2102	1.3045
37	130.909	1.1949	1.1752	1.1486	1.1432	1.1934	1.2827
38	134.545	1.1874	1.1641	1.1334	1.1265	1.1593	1.2655
39	138.182	1.1800	1.1525	1.1180	1.1092	1.1346	1.2554

40	141.818	1.1726	1.1416	1.1038	1.0896	1.1119	1.2519
41	145.455	1.1652	1.1295	1.0911	1.0718	1.0890	1.2484
42	149.091	1.1578	1.1182	1.0787	1.0542	1.0668	1.2368
43	152.727	1.1508	1.1085	1.0657	1.0370	1.0472	1.2317
44	156.364	1.1440	1.0988	1.0529	1.0232	1.0297	1.2242
45	160.000	1.1374	1.0878	1.0409	1.0084	1.0134	1.2220
46	163.636	1.1313	1.0777	1.0290	0.9942	0.9963	1.2109
47	167.273	1.1264	1.0684	1.0169	0.9803	0.9805	1.2020
48	170.909	1.1221	1.0590	1.0055	0.9678	0.9644	1.1884
49	174.545	1.1180	1.0503	0.9951	0.9537	0.9496	1.1773
50	178.182	1.1143	1.0425	0.9849	0.9387	0.9343	1.1711
51	181.818	1.1109	1.0343	0.9741	0.9256	0.9196	1.1623
52	185.455	1.1077	1.0271	0.9621	0.9148	0.9045	1.1547
53	189.091	1.1045	1.0172	0.9516	0.9034	0.8882	1.1497
54	192.727	1.1010	1.0092	0.9449	0.8957	0.8714	1.1421
55	196.364	1.0969	1.0019	0.9393	0.8883	0.8597	1.1344
56	200.000	1.0927	0.9981	0.9325	0.8775	0.8519	1.1280
57	203.636	1.0896	0.9950	0.9261	0.8676	0.8410	1.1228
58	207.273	1.0886	0.9927	0.9195	0.8563	0.8293	1.1088
59	210.909	1.0880	0.9916	0.9136	0.8471	0.8175	1.0926
60	214.545	1.0876	0.9904	0.9086	0.8425	0.8063	1.0750
61	218.182	1.0881	0.9901	0.9037	0.8355	0.7955	1.0557
62	221.818	1.0888	0.9886	0.8989	0.8273	0.7865	1.0383
63	225.455	1.0894	0.9875	0.8952	0.8198	0.7778	1.0268
64	229.091	1.0903	0.9862	0.8920	0.8128	0.7705	1.0095
65	232.727	1.0916	0.9844	0.8892	0.8061	0.7644	0.9911
66	236.364	1.0920	0.9843	0.8861	0.7998	0.7586	0.9687
67	240.000	1.0913	0.9841	0.8851	0.7949	0.7514	0.9440
68	243.636	1.0910	0.9860	0.8834	0.7905	0.7443	0.9155
69	247.273	1.0924	0.9894	0.8807	0.7866	0.7372	0.8846
70	250.909	1.0928	0.9929	0.8795	0.7826	0.7301	0.8642
71	254.545	1.0934	0.9962	0.8803	0.7789	0.7249	0.8449
72	258.182	1.0946	0.9986	0.8840	0.7758	0.7199	0.8254
73	261.818	1.0967	1.0001	0.8875	0.7740	0.7136	0.8024
74	265.455	1.1027	1.0020	0.8907	0.7743	0.7081	0.7741
75	269.091	1.1092	1.0063	0.8932	0.7759	0.7041	0.7513
76	272.727	1.1162	1.0107	0.8957	0.7771	0.7000	0.7287
77	276.364	1.1232	1.0159	0.8982	0.7779	0.6939	0.7009
78	280.000	1.1301	1.0222	0.9038	0.7801	0.6889	0.6707
79	283.636	1.1381	1.0312	0.9116	0.7857	0.6819	0.6449
80	287.273	1.1463	1.0407	0.9219	0.7940	0.6762	0.6169
81	290.909	1.1532	1.0496	0.9305	0.8018	0.6706	0.5825
82	294.545	1.1586	1.0568	0.9386	0.8069	0.6652	0.5579
83	298.182	1.1641	1.0652	0.9466	0.8092	0.6598	0.5332

84	301.818	1.1674	1.0741	0.9575	0.8157	0.6554	0.5133
85	305.455	1.1608	1.0837	0.9729	0.8298	0.6526	0.4885
86	309.091	1.1534	1.0939	0.9905	0.8480	0.6573	0.4699
87	312.727	1.1192	1.1056	1.0094	0.8658	0.6680	0.4600
88	316.364	1.0947	1.1203	1.0241	0.8713	0.6786	0.4589
89	320.000	1.1101	1.1373	1.0361	0.8766	0.6817	0.4550
90	323.636	1.1283	1.1541	1.0512	0.8878	0.6807	0.4513
91	327.273	1.1445	1.1698	1.0725	0.9157	0.6894	0.4534
92	330.909	1.1699	1.1839	1.0974	0.9582	0.7171	0.4729
93	334.545	1.1898	1.1982	1.1262	0.9996	0.7510	0.4891
94	338.182	1.2097	1.2103	1.1532	1.0245	0.7739	0.5149
95	341.818	1.2276	1.2229	1.1708	1.0228	0.8023	0.5611
96	345.455	1.2400	1.2343	1.1785	1.0251	0.8343	0.6201
97	349.091	1.2519	1.2476	1.1893	1.0420	0.8810	0.6769
98	352.727	1.2634	1.2615	1.2105	1.0907	0.9282	0.7284
99	356.364	1.2727	1.2795	1.2459	1.1550	0.9600	0.7778
100	360.000	1.2805	1.3007	1.2887	1.2208	0.9816	0.8403

CURRICULUM VITAE

Mark Jacob Gruenthal

B.S. in Biomedical Engineering & Second Major in Systems Science

HOME ADDRESS

5421 Harbortown Circle

Prospect, KY 40059

BUSINESS ADDRESS

University of Louisville

200 Sackett Hall

Louisville, KY 40292

EDUCATION

Washington University in St. Louis St Louis, MO

Bachelor of Science in Biomedical Engineering May 2007

BME Track: Bioelectrical Systems

Second Major: Systems Science

PUBLICATIONS

Fassbender JM, Saraswat-Ohri S, Myers SA, Gruenthal MJ, Benton RL, Whittemore SR.

(2012) "Deletion of Endoplasmic Reticulum Stress-Induced CHOP Protects

Microvasculature Post-Spinal Cord Injury." *Current Neurovascular Research*. 9(4):274-281

Myers SA, DeVries WH, Gruenthal MJ, Andres KR, Hagg T, Whittemore SR. (2012)

"Sildenafil improves epicenter vascular perfusion but not hindlimb functional recovery after contusive spinal cord injury in mice." *Journal of Neurotrauma*. 29(3):528-538.

Myers SA, DeVries WH, Andres KR, Gruenthal MJ, Benton RL, Hoying JB, Hagg T, Whittemore SR. (2011) "CD47 knockout mice exhibit improved recovery from spinal cord injury." *Neurobiology of Disease*. 42(1):21-34.

Benton RL, Maddie MA, Gruenthal MJ, Hagg T, Whittemore SR. (2009) "Neutralizing endogenous VEGF following traumatic spinal cord injury modulates microvascular plasticity but not tissue sparing or functional recovery." *Current Neurovascular Research*. 6(2):124-131.

ABSTRACTS

Gruenthal MJ, Velasco V, Berson RE, Keynton RS, Williams SJ. (2012) "Impedance Analysis of Endothelial Cells in Development of an Orbital Shear Platform." *American Institute of Chemical Engineers (AIChE) Annual Meeting*. Pittsburgh, PA.